OFFICIAL FILE - TECHNICAL REPORT

FLUID VELOCITY PROFILE DEVELOPMENT FOR TURBULENT FLOW IN SMOOTH ANNULI

By

THEODORE H. OKIISHI

IOWA ENGINEERING EXPERIMENT STATION
IOWA STATE UNIVERSITY OF SCIENCE AND TECHNOLOGY
AMES, IOWA

JULY, 1965

FLUID VELOCITY PROFILE DEVELOPMENT FOR TURBULENT FLOW IN SMOOTH ANNULI

by

Theodore H. Okiishi

This is a reprint of a dissertation submitted to the Graduate Faculty of the Iowa State University in partial fulfillment of the requirements for the degree of Doctor of Philosophy. The experimental data, tabulated in Appendix C and Appendix D of the dissertation have been omitted in this reprint. The research problem discussed was a part of the program supported by the National Aeronautics and Space Administration under Research Grant NsG-62-60.

Project 407-S

Iowa Engineering Experiment Station
Iowa State University of Science and Technology
Ames, Iowa

July, 1965

TABLE OF CONTENTS

INTRODUCTION

This dissertation is concerned with the flow of a Newtonian fluid through a smooth, concentric, constant-area annulus with negligible heat transfer. The fully developed laminar-, transition-, and turbulent-flow cases have been investigated extensively for various annulus configurations.[1] However, there exists a definite scarcity of research on constant-area annulus-inlet flow. The author could find no evidence of previous research, either experimental or theoretical, on the turbulent-flow velocity field existing in a constant-area annulus-inlet section. Inasmuch as turbulent flow through relatively short annular sections occurs frequently in practice, e.g., flow through heat exchangers and axial-flow turbomachinery, there is a need for information on the subject.

Obviously, the flow field existing in the inlet section

---

[1]The term "fully developed flow" has been variously defined as the region in the flow where negligible changes in static-pressure gradients with x occur, where the mean axial-velocity profile changes with x are negligible, where the changes in turbulent-velocity fluctuating terms with x are negligible, where the outer- and inner-wall shear-stress variations with x are negligible, or downstream from the point where the developing boundary layers meet. The various regions described do not necessarily begin at the same axial distance from the annulus entrance.

of an annular passage will depend to some extent on the shape of the entrance. Reason leads to the conclusion that the flow field existing in an annular inlet section with a square-edged entrance as shown in Figure 1 will not be the same as the one existing in an annular inlet section with a rounded entrance, also shown in Figure 1. For the square-edged entrance case, flow separation is expected at the outer wall very near the inlet because of the abrupt change in cross section. Therefore, no conventional boundary-layer development is involved. For the rounded-entrance case, a uniform mean-velocity variation with radius is expected at the entrance to the passage. The flow existing beyond the entrance might be expected to behave like the flow between two flat plates that are parallel to each other. Thus, for each wall, boundary-layer growth and progression from laminar to turbulent flow are expected.

In single-boundary internal flow, for example, flow through passages having circular, rectangular, and triangular cross sections, the boundary layer develops on one surface only; therefore, only one wall-shear-stress variation is involved. Further, single-boundary flow usually occurs in a configuration that allows for easy determination of the

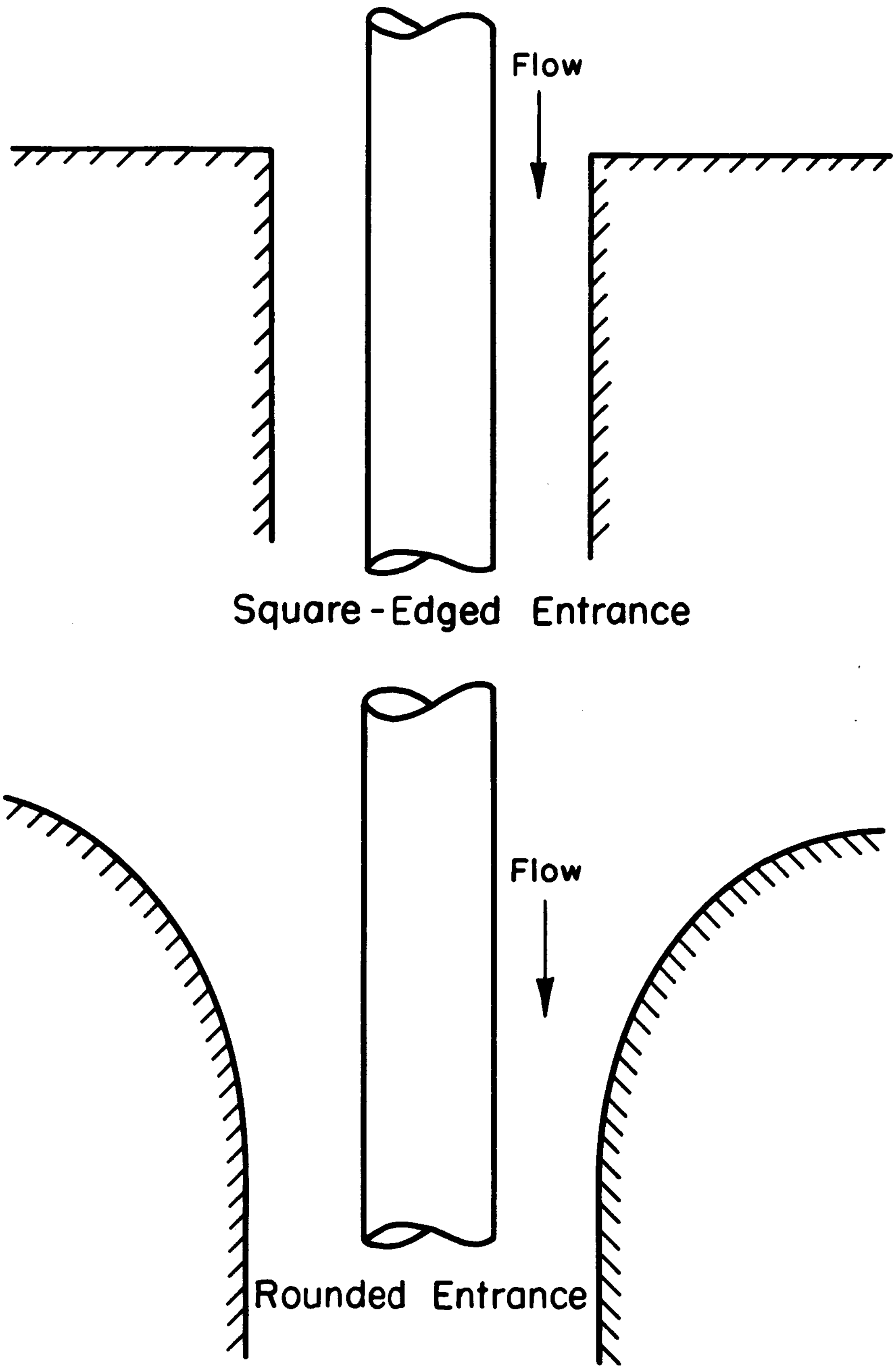

Figure 1. Square-edged and rounded entrances.

maximum velocity (zero shear) location. Two wall-shear-stress distributions and boundary-layer developments exist for flow through annuli. Also, as pointed out by Brighton and Jones (5) and Okiishi and Serovy (30), the location of the radius of maximum velocity for annular flow is not straightforward except for the laminar-flow case.

At the present time, because of the limited number of equations and the overwhelming number of unknowns, turbulent flow is not especially amenable to strict theoretical analysis. Approximate methods based on the momentum-integral equation and energy equation have been used for predicting average turbulent-flow properties. The successful application of these approximate methods depended, however, on the use of experimentally determined results.

Thus, an initial study of the turbulent-flow development in an annular space is likely to be experimental. Because turbulent flow is random and chaotic and boundary-layer transition is intermittent, a true picture of the developing flow field is obtainable only by instantaneously collecting field data at numerous axial and radial locations. This is not feasible at the present time because the present state of instrumentation technology will not allow it; a more practical alternative is to measure average flow properties over longer periods of time.

The current investigation was carried out as a step toward understanding the nature of turbulent flow in the inlet section of a constant-area annulus. Experimental results based on measurements of mean axial velocities and outer-wall static pressures are presented for air flow through two annuli over a Re_D range of approximately 70,000 to 160,000. The radius ratios of the annuli were 0.344 and 0.531, and each annulus was tested with both square-edged and rounded entrances. The feasibility of using the approximate solution approach based on the momentum-integral equation to predict inlet flow characteristics was investigated.

REVIEW OF RELATED RESEARCH

Fully Developed Flow In Annuli

Laminar flow

The equations for velocity profile, radius of maximum velocity, and static-pressure gradient for steady, fully developed, incompressible and laminar fluid flow in an annulus can be derived analytically as shown, for example, in the text by Lamb (24), by solving the Navier-Stokes equations and the continuity equation.[1] The derived equations have been verified experimentally (33, 37, 47) and are

$$u = \frac{2U_a[r_2^2 - r^2 - 2r_m^2 \ln(r_2/r)]}{r_2^2 + r_1^2 - 2r_m^2} \qquad (1)$$

$$r_m = \sqrt{\frac{r_2^2 - r_1^2}{2\ln(r_2/r_1)}} \qquad (2)$$

$$\frac{dp}{dx} = -\frac{8\mu U_a}{g_c(r_2^2 + r_1^2 - 2r_m^2)} \qquad (3)$$

---

[1]The term "fully developed" is used here to describe the region in the flow where the axial-point-velocity profiles are not changing with axial distance.

Transition flow

Transition flow is difficult to study, analytically or experimentally, because of its unstable nature. However, a few annular transition-flow studies have been made (9, 10, 33, 38, 47, 48). Prengle and Rothfus (33) concluded from the behavior of their dye-study observations that the laminar- to turbulent-flow transition range for flow through annuli extended from Reynolds numbers based on $2(r_2^2 - r_m^2)/r_2$ of 700 ± 50 to 2,200 or 2,300. The direct skin-friction measurements of Rothfus *et al.* (38) showed that the radius of maximum velocity shifts appreciably for transition flow. From velocity-profile measurements, Walker (47) and Croop (9) obtained radius of maximum velocity variation trends that were similar to the one followed by the skin-friction-data r_m values for transition flow. The shift appeared to be dependent upon radius ratio as well as Reynolds number, and Croop concluded that no simple correlation that would describe the shift of r_m existed. The general trend was a shift of r_m toward the core at the lower end of the transition range, a subsequent shift away from the core beyond the laminar-flow value for larger Reynolds numbers, and finally, a shift inward with larger Reynolds numbers till the laminar-flow value of r_m was again attained.

Turbulent flow

Theory and experiment have been combined to arrive at conclusions about fully developed turbulent flow in annuli.[1] In the bibliographies of several recent publications (5, 30, 34), most of the studies done in the past are listed. Brighton and Jones' work (5) is especially enlightening because of the turbulence measurements presented and the conclusions drawn with respect to the location of the radius of maximum velocity.

Inlet-Region Flow Through Internal Passages

Laminar flow

The axial development of velocity profiles and static-pressure drop for the laminar flow of a fluid in the entrance region of tubes and ducts has been studied analytically and experimentally. Lundgren *et al.* (27) grouped the methods of solution of the problem into four general categories. These categories are used in Table 1 as a means of classifying previous research.

---

[1]The term "fully developed" is used here to describe the region in the flow where the mean-axial-point velocity profile changes with length along the axis are negligible.

Table 1. Summary of past analytical research on the problem of the development of the laminar flow of a fluid in the entrance region of ducts

Researcher(s)	Reference	Conduit shape	Approach to solution
Sparrow *et al*.	44	Tubes and rectangular ducts	Linearization of the inertia terms of the Navier-Stokes differential equation of motion for the axial direction
Lundgren *et al*.	27	Arbitrary	Linearization...
Langhaar	25	Tube	Linearization...
Hanks	18	Tube	Linearization...
Targ	Cited in Lungren *et al*. (27)	Tube	Linearization...
Han	17	Rectangular duct	Linearization...
Sparrow *et al*.	Cited in Lungren *et al*. (27)	Parallel-plate channel	Linearization...
Sugino	45	Annulus	Linearization...
Sparrow and Lin	43	Annulus	Linearization...
Chang and Atabek	7	Annulus	Linearization...

Table 1 (Continued)

Researcher(s)	Reference	Conduit shape	Approach to solution
Heaton *et al.*	19	Annulus	Linearization...
Schlichting	Cited in Lundgren *et al.* (27)	Parallel-plate channel	Patching together boundary-layer solutions which apply near the entrance and pertubations of the fully developed solutions which apply far downstream
Atkinson and Goldstein	16	Tube	Patching...
Roidt and Cess	35	Rectangular duct	Patching...
Collins and Schowalter	8	Rectangular duct	Patching...
Schiller	Cited in Lundgren *et al.* (27)	Tube and parallel-plate channel	Application of a model consisting of a developing boundary layer and an inviscid-core flow in conjunction with an integral representation of the momentum-conservation principle

Table 1 (Continued)

Researcher(s)	Reference	Conduit shape	Approach to solution
Siegel	Cited in Campbell and Slattery (6)	Tube	Application...
Campbell and Slattery	6	Tube	Application...
Bodoia and Osterle	4	Parallel-plate channel	Reduction of the mass- and momentum-conservation equations to finite difference form with subsequent numerical solution on an electronic digital computer

The experimental velocity-profile development and static-pressure-drop results for laminar flow in the inlet of a tube by Nikuradse, Pfenninger, and Reshotko as cited by Campbell and Slattery (6), and analytical work by Atkinson and Goldstein, Langharr, Schiller, Siegel, and Campbell and Slattery as cited in Table 1 compared favorably as shown by Campbell and Slattery. Thus there is evidence that the first three approaches result in equations that approximate the actual inlet-flow field well. Bodoia and Osterle (4) did not attempt to compare their results with experimental data.

The results of the analytical studies of laminar flow in the inlet region of an annulus were, in general, in the form of very complicated functions. No suitable experimental velocity data were presented for comparison. The analytical heat-transfer results of Heaton *et al*. (19) compared favorably with a limited amount of experimental heat-transfer data.

Turbulent flow

Analytical studies of pipe-inlet flow Analytical studies (13, 14, 20, 26, 32, 36) of the turbulent flow of a fluid in the inlet region of pipes have been, by sheer necessity, semi-empirical in nature. Further, the results of such analyses were predictions of bulk flow quantities, such as core or maximum velocity, static-pressure-head loss, and boundary-layer-thickness parameters which compared reasonably well with the limited amount of experimental values available. Some of the basic assumptions made as initial steps in arriving at solutions in the above-mentioned studies were:

1. The existence of a uniform velocity distribution at the start of the inlet section.
2. The existence of a turbulent boundary layer from the beginning of the constant-area section.
3. The existence of a core of fluid outside the boundary layer where the flow was irrotational.
4. Negligible pressure variation in the radial direction.
5. Negligible effects due to fluctuating components.

All of the analyses began with a statement of the momentum-integral equation. They differed only in the assumptions made about the behavior of the various fluid-flow properties involved.

The author could find no previous analytical studies of the developing turbulent flow in annuli.

<u>Experimental study of pipe-inlet flow</u> Barbin and Jones (3) published the results of what appears to be the

most extensive experimental study of the turbulent flow of a fluid in the inlet region of a pipe. Measurements of mean velocities in the axial direction, turbulence intensities, and Reynolds stresses at several axial locations were presented for a pipe Reynolds number of 388,000. Boundary-layer transition was artificially produced and controlled with sand grains cemented to the outer wall near the entrance. Some of their conclusions were:

1. The momentum flux based on experimental data remained constant in the inlet region for $\frac{x}{D} > 1.5$.
2. Mean axial velocities, turbulence intensities, and Reynolds stresses were still changing with axial distance at a distance of 40.5 diameters from the entrance.
3. Velocity profiles in the inlet regions were not similar.

Experimental studies of annular-inlet flow   The only experimental studies of the turbulent flow of a fluid in the inlet region of an annulus found in the literature were reported by Olson and Sparrow (31) and Rothfus *et al*. (38). The Re_D range for the Rothfus study was approximately 900 to 45,000. The entrances to the annuli were square-edged as shown in Figure 1. Average inner-wall shear stresses were calculated for a 4-foot section, an 8-foot section, and a 12-foot section of annulus and assumed to be the local value for the mid-length axial location of the section. Thus, at best, the results are approximate. The trends demonstrated by the data were a decrease of shear stress with distance from the entrance and a decrease of effect of inlet length on shear stress with an increase in Reynolds number. The results of Olson and Sparrow (31) were based on numerous static-pressure measurements made along the axes of annuli. The Re_D range covered was 16,000 to 70,000. The annulus size and entrance-region information is summarized in Table 2. The entrance configurations are shown in Figure 2.

Table 2. Annuli dimensions for Olson and Sparrow study

Annulus	Inner-tube outside diameter in.	Outer-tube inside diameter in.	r_1/r_2	Entrance
1	.3125	1.00	.312	Square-edged Rounded
2	.500	1.00	.500	Square-edged Rounded

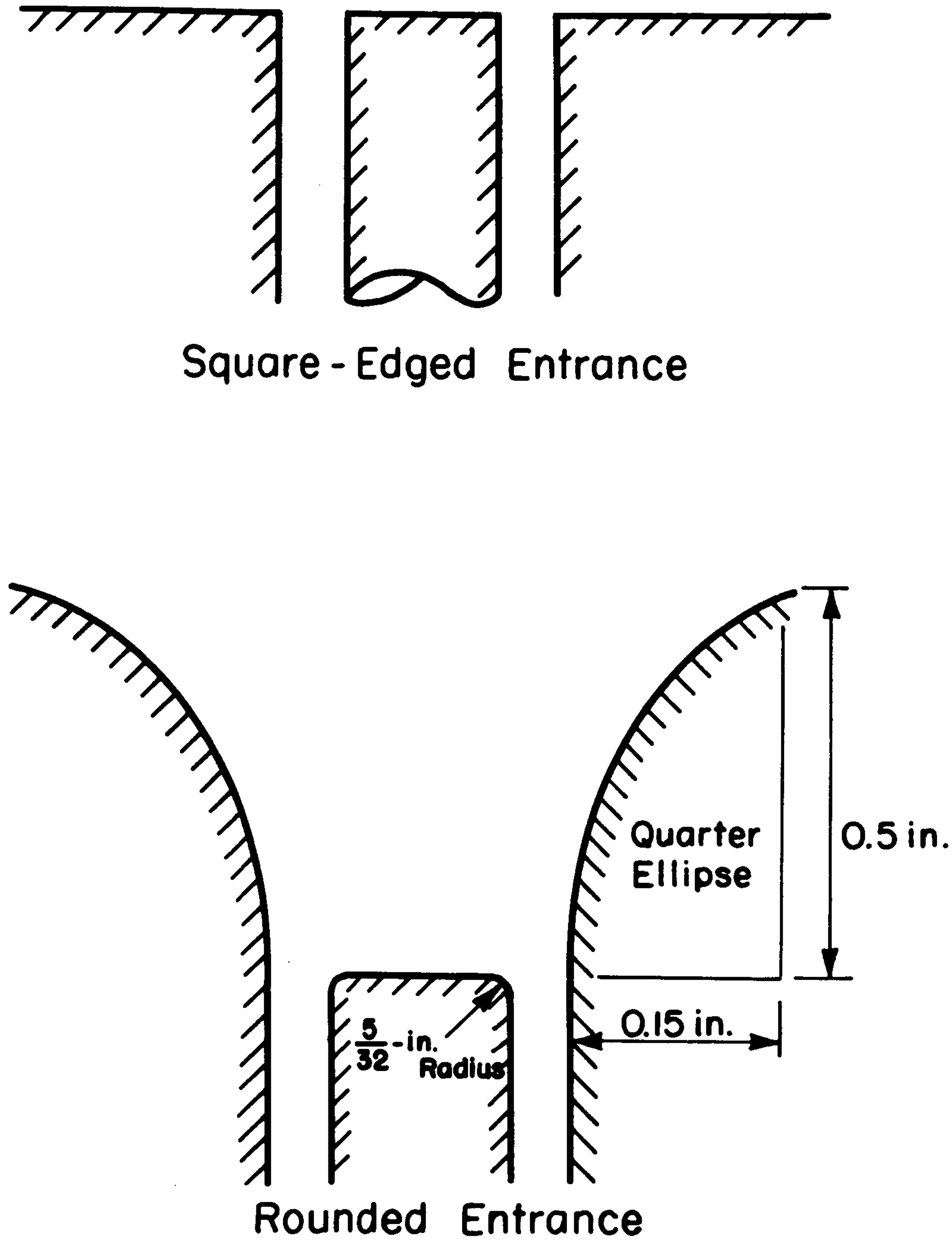

Figure 2. Square-edged and rounded entrances of the Olson and Sparrow (31) test apparatus.

Their conclusions were:

1. For the square-edged-entrance annuli, the length over which separation occurred was shortest for annulus 2 and slightly longer for annulus 1.
2. The entrance length, defined in terms of the length of duct required for the local pressure gradient to approach to within 5% of the fully developed value, for the square-edged- and rounded-entrance tests ranged from 20 to 25 hydraulic diameters. In the case where a turbulent boundary layer was induced at both surfaces by tripping, the entrance length was reduced to 15 hydraulic diameters.

In a review of the literature, no experimental studies of the developing turbulent-velocity profile in an annular passage could be identified.

ANALYSIS

The Reynolds equations of motion for turbulent flow of fluids, expressed in cylindrical coordinates, are (39)

$$\frac{\partial v}{\partial t} + \frac{v\partial v}{\partial r} + \frac{w}{r}\frac{\partial v}{\partial \emptyset} + \frac{u\partial v}{\partial x} - \frac{w^2}{r} = -\frac{\partial}{\partial r}\left[\frac{g_c p}{\rho} + g_c\Omega\right]$$

$$+ \frac{\partial}{\partial r}\left[\nu\left(\frac{\partial v}{\partial r} + \frac{v}{r}\right) - \overline{v'v'}\right] + \frac{1}{r}\frac{\partial}{\partial \emptyset}\left[\frac{\nu}{r}\left(\frac{\partial v}{\partial \emptyset} - 2w\right) - \overline{v'w'}\right]$$

$$+ \frac{\partial}{\partial x}\left(\nu\frac{\partial v}{\partial x} - v'u'\right) - \frac{\overline{v'v'}}{r} + \frac{\overline{w'w'}}{r} \qquad (4)$$

$$\frac{\partial w}{\partial t} + \frac{v\partial w}{\partial r} + \frac{w}{r}\frac{\partial w}{\partial \emptyset} + \frac{u\partial w}{\partial x} + \frac{vw}{r} = -\frac{1}{r}\frac{\partial}{\partial \emptyset}\left[\frac{g_c p}{\rho} + g_c\Omega\right]$$

$$+ \frac{\partial}{\partial r}\left[\nu\left(\frac{\partial w}{\partial r} + \frac{w}{r}\right) - \overline{v'w'}\right] + \frac{1}{r}\frac{\partial}{\partial \emptyset}\left[\frac{\nu}{r}\left(\frac{\partial w}{\partial \emptyset} + 2v\right) - \overline{w'w'}\right]$$

$$+ \frac{\partial}{\partial x}\left(\nu\frac{\partial w}{\partial x} - \overline{w'u'}\right) - 2\,\frac{\overline{v'w'}}{r} \qquad (5)$$

$$\frac{\partial u}{\partial t} + \frac{v\partial u}{\partial r} + \frac{w}{r}\frac{\partial u}{\partial \emptyset} + \frac{u\partial u}{\partial x} = -\frac{\partial}{\partial x}\left[\frac{g_c p}{\rho} + g_c\Omega\right]$$

$$+ \frac{\partial}{\partial r}\left[\nu\left(\frac{\partial u}{\partial r} + \frac{u}{r}\right) - \overline{v'u'}\right] + \frac{1}{r}\frac{\partial}{\partial \emptyset}\left(\frac{\nu}{r}\frac{\partial u}{\partial \emptyset} - \overline{u'w'}\right)$$

$$+ \frac{\partial}{\partial x}\left(\nu\frac{\partial u}{\partial x} - \overline{u'u'}\right) - \frac{\overline{v'u'}}{r} + \frac{u\nu}{r^2} \qquad (6)$$

For the condition of steady, incompressible, and axisymmetric swirl-free flow of a gas the equations of motion become

$$v\frac{\partial v}{\partial r} + u\frac{\partial v}{\partial x} = -\frac{g_c}{\rho}\frac{\partial p}{\partial r} + \nu\left[\frac{\partial^2 v}{\partial r^2} + \frac{\partial}{\partial r}\left(\frac{v}{r}\right) + \frac{\partial^2 v}{\partial x^2}\right]$$

$$-\frac{\partial}{\partial x}(\overline{v'u'}) - \frac{\partial}{\partial r}(\overline{v'v'}) - \frac{\overline{v'v'}}{r} + \frac{\overline{w'w'}}{r} \qquad (7)$$

$$0 = -\frac{\partial}{\partial r}(\overline{v'w'}) - \frac{\partial}{\partial x}(\overline{w'u'}) - 2\,\frac{\overline{v'w'}}{r} \qquad (8)$$

$$v\frac{\partial u}{\partial r} + u\frac{\partial u}{\partial x} = -\frac{g_c}{\rho}\frac{\partial p}{\partial x} + \nu\left[\frac{\partial^2 u}{\partial r^2} + \frac{1}{r}\frac{\partial u}{\partial r} + \frac{\partial^2 u}{\partial x^2}\right]$$

$$-\frac{\partial}{\partial x}(\overline{u'u'}) - \frac{\partial}{\partial r}(\overline{v'u'}) - \frac{\overline{v'u'}}{r} \qquad (9)$$

Solutions for laminar flow in an inlet section based on the Navier-Stokes equations of motion have been obtained. However, parallel solutions for turbulent flow in an inlet section based on the Reynolds equation of motion do not appear to be feasible because of the large number of unknown quantities involved. There is a definite paucity of knowledge about the fluctuating component variables involved. As mentioned previously, the author located only one investigation, see Barbin and Jones (3), of the structure of turbulence in the inlet of an internal duct. Measurements of the fluctuating components u', and w', and the Reynolds stresses $\overline{u'v'}$ were made for flow in a pipe inlet with a pipe-diameter Reynolds number of 388,000. An approach based on the approximate momentum-integral equation appears to be more practical.

The flow of a fluid in the inlet section of an annulus with a square-edged entrance does not involve a conventional boundary-layer growth because of the fluid separation that occurs near the entrance. Therefore, no attempt is made to arrive at analytical results for this case. On the other hand, annular flow through a rounded entrance involves boundary-layer growth on the inner and outer walls in the presence of a negative pressure gradient. One approach to the solution of the annular-inlet turbulent-flow problem would be to consider the inner and outer boundary layers separately. This possibility is investigated further in the following paragraphs.

If the pressure variation in the radial direction and the fluctuating velocity-component terms involved are considered negligible as suggested by Thwaites (46), the momentum-integral equation for the inner-wall boundary layer is

$$-\frac{d}{dx}\left(\int_{r_1}^{r_{\delta 1}}\frac{\rho u^2 r dr}{g_c}\right) + U\frac{d}{dx}\left(\int_{r_1}^{r_{\delta 1}}\frac{\rho u r dr}{g_c}\right) = \tau_{01} r_1 + \frac{dp}{dx}\frac{(r_{\delta 1}^2 - r_1^2)}{2} \tag{10}$$

Further, if the flow of the fluid existing outside the developing boundary layer is assumed to be irrotational, the following relationship is true

$$\frac{dp}{dx} = -\frac{\rho}{2g_c}\frac{dU^2}{dx} = -\frac{\rho U}{g_c}\frac{dU}{dx} \tag{11}$$

Also,

$$\frac{d}{dx}\left(U\int_{r_1}^{r_{\delta 1}} urdr\right) = U\frac{d}{dx}\left(\int_{r_1}^{r_{\delta 1}} urdr\right) + \frac{dU}{dx}\left(\int_{r_1}^{r_{\delta 1}} urdr\right) \tag{12}$$

If Equation 11 and Equation 12 are substituted into Equation 10, the result is

$$\frac{\rho}{g_c}\frac{d}{dx}\left[\int_{r_1}^{r_{\delta 1}}(U-u)urdr\right] + \frac{\rho}{g_c}\frac{dU}{dx}\int_{r_1}^{r_{\delta 1}}(U-u)rdr = \tau_{01} r_1 \tag{13}$$

But,

$$\frac{d}{dx}\left[\frac{1}{U^2}\int_{r_1}^{r_{\delta 1}}(U-u)urdr\right] = \frac{1}{U^2}\frac{d}{dx}\left[\int_{r_1}^{r_{\delta 1}}(U-u)urdr\right] +$$

$$\frac{d(U^{-2})}{dx}\int_{r_1}^{r_{\delta 1}}(U-u)urdr \tag{14}$$

Therefore,

$$\frac{d}{dx}\left[\int_{r_1}^{r_{\delta 1}} (1 - \frac{u}{U})(\frac{u}{U}) r dr\right] + \frac{1}{U}\frac{dU}{dx}\left[\int_{r_1}^{r_{\delta 1}} 2(1 - \frac{u}{U})\frac{u}{U} r dr\right.$$

$$\left. + \int_{r_1}^{r_{\delta 1}} (1 - \frac{u}{U}) r dr\right] = \frac{\tau_{01} r_1 g_c}{\rho U^2} \quad (15)$$

Derived in a similar fashion, the differential equation for the outer-wall boundary layer is

$$\frac{d}{dx}\left[\int_{r_{\delta 2}}^{r_2} (1 - \frac{u}{U})(\frac{u}{U}) r dr\right] + \frac{1}{U}\frac{dU}{dx}\left[\int_{r_{\delta 2}}^{r_2} 2(1 - \frac{u}{U})(\frac{u}{U}) r dr\right.$$

$$\left. + \int_{r_{\delta 2}}^{r_2} (1 - \frac{u}{U}) r dr\right] = \frac{\tau_{02} r_2 g_c}{\rho U^2} \quad (16)$$

Approximate boundary-layer thickness-parameter equations that do not take into account surface curvature in the transverse direction are

$$\delta_1^* = \frac{1}{r_1} \int_{r_1}^{r_{\delta 1}} r(1 - \frac{u}{U}) dr \quad (17)$$

$$\delta_1^{**} = \frac{1}{r_1} \int_{r_1}^{r_{\delta 1}} r \frac{u}{U}(1 - \frac{u}{U}) dr \quad (18)$$

$$\delta_2^* = \frac{1}{r_2} \int_{r_{\delta 2}}^{r_2} r(1 - \frac{u}{U}) dr \quad (19)$$

$$\delta_2^{**} = \frac{1}{r_2} \int_{r_{\delta 2}}^{r_2} r \frac{u}{U}(1 - \frac{u}{U}) dr \quad (20)$$

The exact boundary-layer thickness-parameter equations are

$$\theta_1^* = \sqrt{\int_{r_1}^{r_{\delta 1}} 2\left(1 - \frac{u}{U}\right) r\,dr + r_1^2} - r_1 \tag{21}$$

$$\theta_1^{**} = \sqrt{\int_{r_1}^{r_{\delta 1}} 2r\frac{u}{U}\left(1 - \frac{u}{U}\right) dr + r_1^2} - r_1 \tag{22}$$

$$\theta_2^* = r_2 - \sqrt{r_2^2 - \int_{r_{\delta 2}}^{r_2} 2\left(1 - \frac{u}{U}\right) r\,dr} \tag{23}$$

$$\theta_2^{**} = r_2 - \sqrt{r_2^2 - \int_{r_{\delta 2}}^{r_2} 2r\frac{u}{U}\left(1 - \frac{u}{U}\right) dr} \tag{24}$$

The inner- and outer-wall boundary-layer differential equations expressed in terms of the approximate thickness parameters are

$$\frac{d\delta_1^{**}}{dx} + \frac{1}{U}\frac{dU}{dx}\left(2\delta_1^{**} + \delta_1^*\right) = \frac{\tau_{01} g_c}{\rho U^2} \tag{25}$$

$$\frac{d\delta_2^{**}}{dx} + \frac{1}{U}\frac{dU}{dx}\left(2\delta_2^{**} + \delta_2^*\right) = \frac{\tau_{02} g_c}{\rho U^2} \tag{26}$$

The shape parameter, H, for boundary layers is defined as the ratio of the displacement and momentum thicknesses. Therefore,

$$H_1 = \frac{\delta_1^*}{\delta_1^{**}} \tag{27}$$

and
$$H_2 = \frac{\delta_2^*}{\delta_2^{**}} \tag{28}$$

The inner- and outer-wall boundary-layer equations, in terms of H_1 and H_2, are

$$\frac{d\delta_1^{**}}{dx} + \frac{\delta_1^{**}}{U}\frac{dU}{dx}(2 + H_1) = \frac{\tau_{01} g_c}{\rho U^2} \tag{29}$$

$$\frac{d\delta_2^{**}}{dx} + \frac{\delta_2^{**}}{U}\frac{dU}{dx}(2 + H_2) = \frac{\tau_{02} g_c}{\rho U^2} \tag{30}$$

In comparison, the corresponding differential equation for the boundary-layer flow over a flat plate in the presence of a pressure gradient is

$$\frac{d\beta^{**}}{dx} + \frac{\beta^{**}}{U}\frac{dU}{dx}(2 + H) = \frac{\tau_o g_c}{\rho U^2} \tag{31}$$

where

$$\beta^{**} = \int_o^\beta \frac{u}{U}(1 - \frac{u}{U})dy \tag{32}$$

$$\beta^* = \int_o^\beta (1 - \frac{u}{U})dy \tag{33}$$

and

$$H = \frac{\beta^*}{\beta^{**}} \tag{34}$$

As shown in summary form by Schlichting (40) and Thwaites (46), several solutions to the flat-plate boundary-layer differential equation exist. The laminar-flow boundary-layer solutions were based on two general techniques that can be attributed to Pohlhausen and Thwaites as cited in Schlichting (40). Thwaites (46) pointed out that the chief differences between the turbulent-flow boundary-layer solutions were in the assumptions made about the behavior of H and $\frac{\tau_o g_c}{\rho U^2}$. In all cases, a copious amount of experimental data was required as a basis for the evaluation of these quantities. All of the solutions were in terms of a known potential-flow field, i.e., the variation with x of pressure or U was assumed known.

It appears then, that equations 29 and 30 that describe the flow in the inner- and outer-wall boundary layers of an annulus could be solved in terms of a given variable such as U. Before this is achieved, however, detailed experimental data for both the laminar and turbulent boundary layers existing in an annulus inlet need to be obtained so that reasonable hypotheses about variations of H_1, H_2, $\frac{\tau_{01} g_c}{\rho U^2}$ and

$\frac{\tau_{02} g_c}{\rho U^2}$ can be made.

If the continuity equation

$$\frac{d}{dx}[U(r_2^2-r_1^2) - 2r_1\delta_1^* U - 2r_2\delta_2^* U] = 0 \tag{35}$$

or

$$\frac{1}{U}\frac{dU}{dx} = \frac{2r_1 \frac{d\delta_1^*}{dx} + 2r_2 \frac{d\delta_2^*}{dx}}{r_2^2-r_1^2-2r_1\delta_1^* - 2r_2\delta_2^*} \tag{36}$$

is combined with Equations 29 and 30, the resultant equations are

$$\frac{d\delta_1^{**}}{dx}[r_2^2-r_1^2+2r_1H_1\delta_1^{**}(1+H_1)-2r_2H_2\delta_2^{**}] + \frac{d\delta_2^{**}}{dx}[2r_2H_2\delta_1^{**}(2+H_1)]$$

$$+ \frac{dH_1}{dx}[2r_1(\delta_1^{**})^2(2+H_1)] + \frac{dH_2}{dx}[2r_2\delta_1^{**}\delta_2^{**}(2+H_1)]$$

$$= \frac{\tau_{01} g_c}{\rho U^2}[r_2^2-r_1^2-2(r_1H_1\delta_1^{**}+r_2H_2\delta_2^{**})] \tag{37}$$

$$\frac{d\delta_1^{**}}{dx}[2r_1H_1\delta_2^{**}(2+H_2)] + \frac{d\delta_2^{**}}{dx}[r_2^2-r_1^2+2r_2H_2\delta_2^{**}(1+H_2)-2r_1H_1\delta_1^{**}]$$

$$+ \frac{dH_1}{dx}[2r_1\delta_1^{**}\delta_2^{**}(2+H_2)] + \frac{dH_2}{dx}[2r_2(\delta_2^{**})^2(2+H_2)]$$

$$= \frac{\tau_0 2 g_c}{\rho U^2}(r_2^2 - r_1^2 - 2r_1 H_1 \delta_1^{**} - 2r_2 H_2 \delta_2^{**}) \qquad (38)$$

Experimental data are still necessary for a solution.

The unstable nature of transition is no small problem. Schubauer and Klebanoff (41) have demonstrated that for flow over a flat plate the process of transition is intermittent and consists of laminar and turbulent regions. They concluded that transition starts from perturbations in the laminar flow in the form of spots that grow, move downstream, and merge to form the completely turbulent region. Thus, the concept of transition occurring along a continuous line transverse to the flow is false. Schlichting (40) reviewed the research done on the transition problem for flat-plate boundary layers and concluded that transition could occur at distances from the leading edge that correspond to Re_x values ranging from 3.5×10^5 to 4.0×10^6 depending upon surface conditions and the turbulence intensity of the free stream. Thus, there is evidence that the region or area over which transition occurs shifts when surface and flow conditions change.

Clearly, an experimental investigation of the turbulent-flow field in an annulus is in order.

EXPERIMENTAL APPARATUS

The experimental results obtained during the present investigation were measured in vertical annuli formed by positioning smooth TYPE K copper tubes concentrically within a smooth red-brass pipe. The pertinent dimensions of the different annuli are listed in Table 3.

Table 3. Pertinent dimensions of annuli for present investigation

Annulus designation	Inner-tube outside diameter in.	Outer-tube inside diameter in.	$\frac{r_1}{r_2}$	Inlet
1 SQ	1.375	4.000	0.344	Square-edged
1 RD	1.375	4.000	0.344	Rounded
2 SQ	2.125	4.000	0.531	Square-edged
2 RD	2.125	4.000	0.531	Rounded

A schematic drawing of the test apparatus is shown in Figure 3. Air flow through the annuli was initiated and maintained by a constant-speed centrifugal blower.

Six-inch long plastic tubes, all having a diameter of

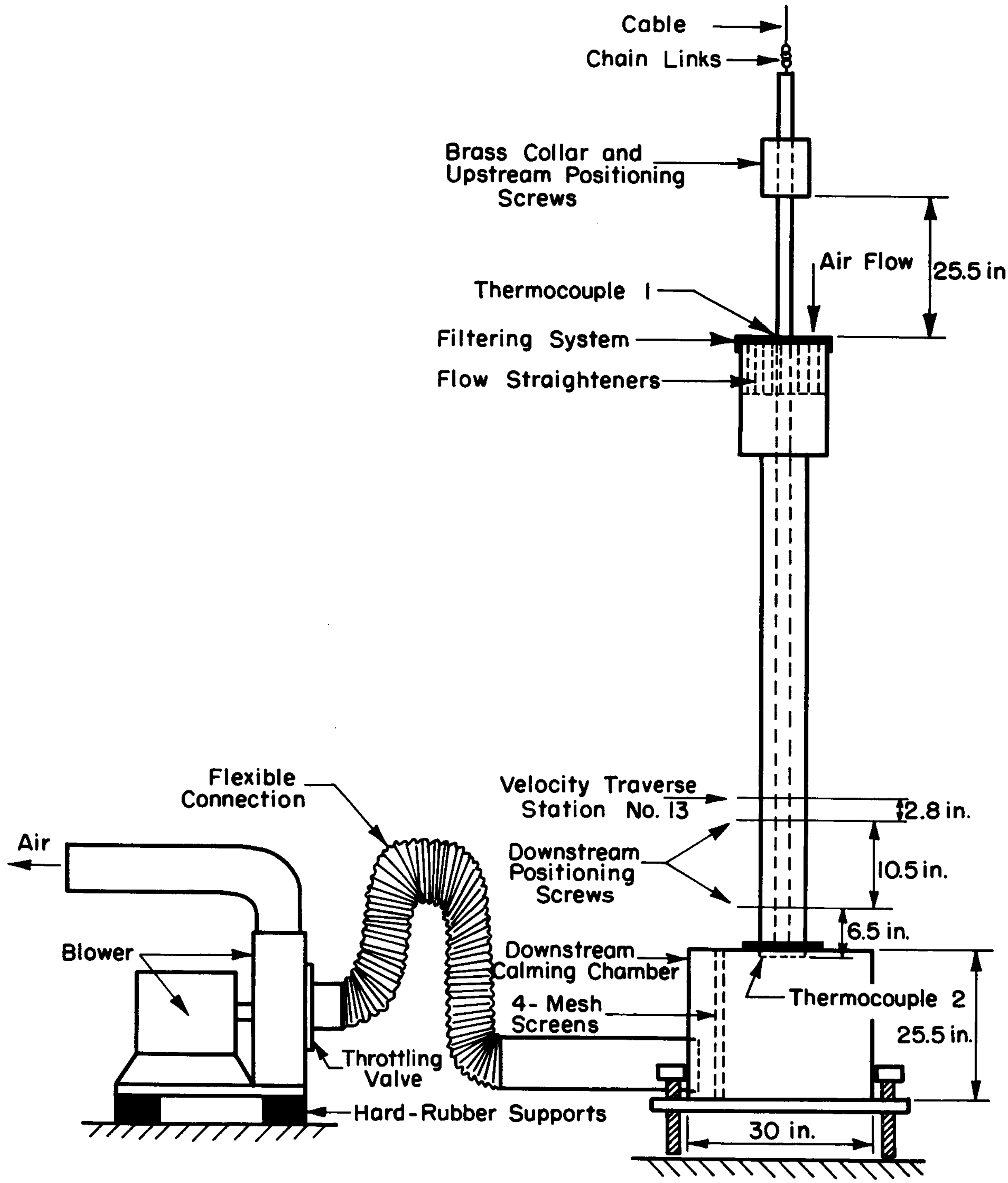

Figure 3. Schematic diagram of the test apparatus.

1.25 inches, were placed at the upstream end of the cylindrical inlet to the test section as shown in Figures 3 and 4. They were arranged in a honeycomb pattern around the inner tube to help impart axial motion to the fluid. The inlet to the annuli was a galvanized-sheet-metal cylinder that was surrounded and supported circumferentially by a box made from 3/4-inch thick plywood. The pertinent dimensions and details of construction for the square-edged and rounded inlets are shown in Figure 4. All joints in the flow boundaries were made smooth by hand finishing the adjacent surfaces. The shape and dimensions of the rounded inlet were those suggested by the American Society of Mechanical Engineers (1) for a long-radius flow nozzle. The filtering system consisted of 4 layers of No. 1370 CV Ny-Sul-Loft air-filter material from the Lamports Company and a sheet of 1-inch thick Owens-Corning commercial fiberglass material. It was held in place upstream from the plastic tubes with a 2-mesh screen. The filters were replaced after every Re_D-annulus combination run had been completed.

The 30 by 30 by 25.5-inch downstream calming chamber was constructed from 3/4-inch thick plywood. The side view dimensions of the chamber are given in Figure 3, and the details of the exit-section construction are shown in Figure

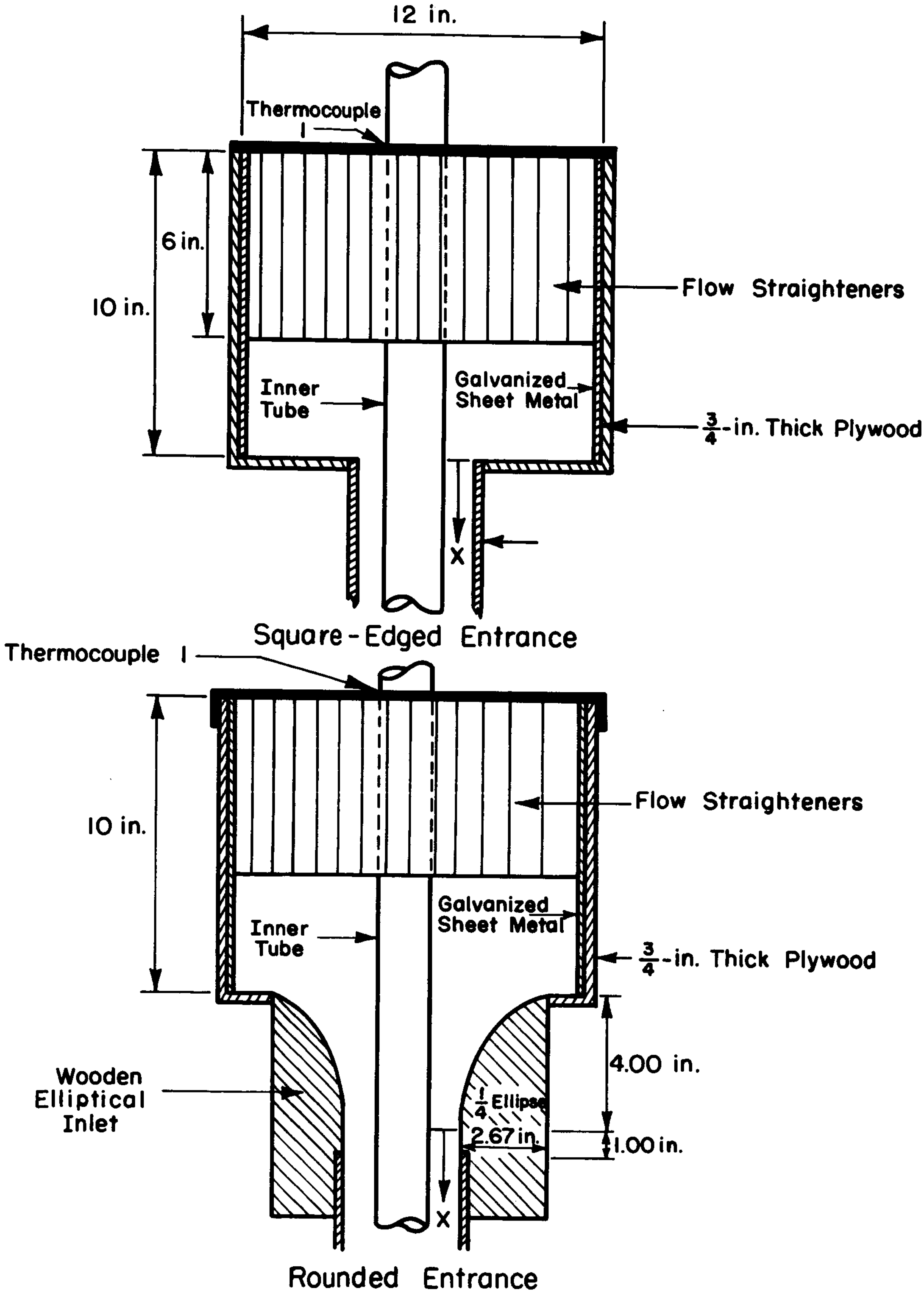

Figure 4. Entrance-construction details.

5. As shown in Figure 5, the inner tube available for forming annulus 2 was not long enough to extend beyond the downstream end of the outer tube as did the inner tube of annulus 1. The author assumed that this difference would not affect the flow development upstream. No apparent effects on the data were noticed.

The inner tubes were supported with a cable and positioned concentrically with four sets of 10-32 machine screws. As shown in Figure 3, the two upstream sets of positioning screws were located in a 5-inch long section of 4.5-inch outer diameter red-brass pipe that was positioned approximately 25.5 inches above the entrance to the cylindrical inlet section. The two upstream sets included six and five 10-32 screws spaced circumferentially. The two downstream sets of positioning screws were located 6.5 and 17 inches from the downstream end of the outer brass tube. The set that was 6.5 inches from the exit included five 10-32 screws spaced circumferentially while the set located 17 inches from the exit included three 10-32 screws spaced circumferentially. The final velocity-traverse station was located 19.75 inches from the exit. Since the sets of positioning screws were located above the inlet and downstream from the final velocity-traverse station, no physical

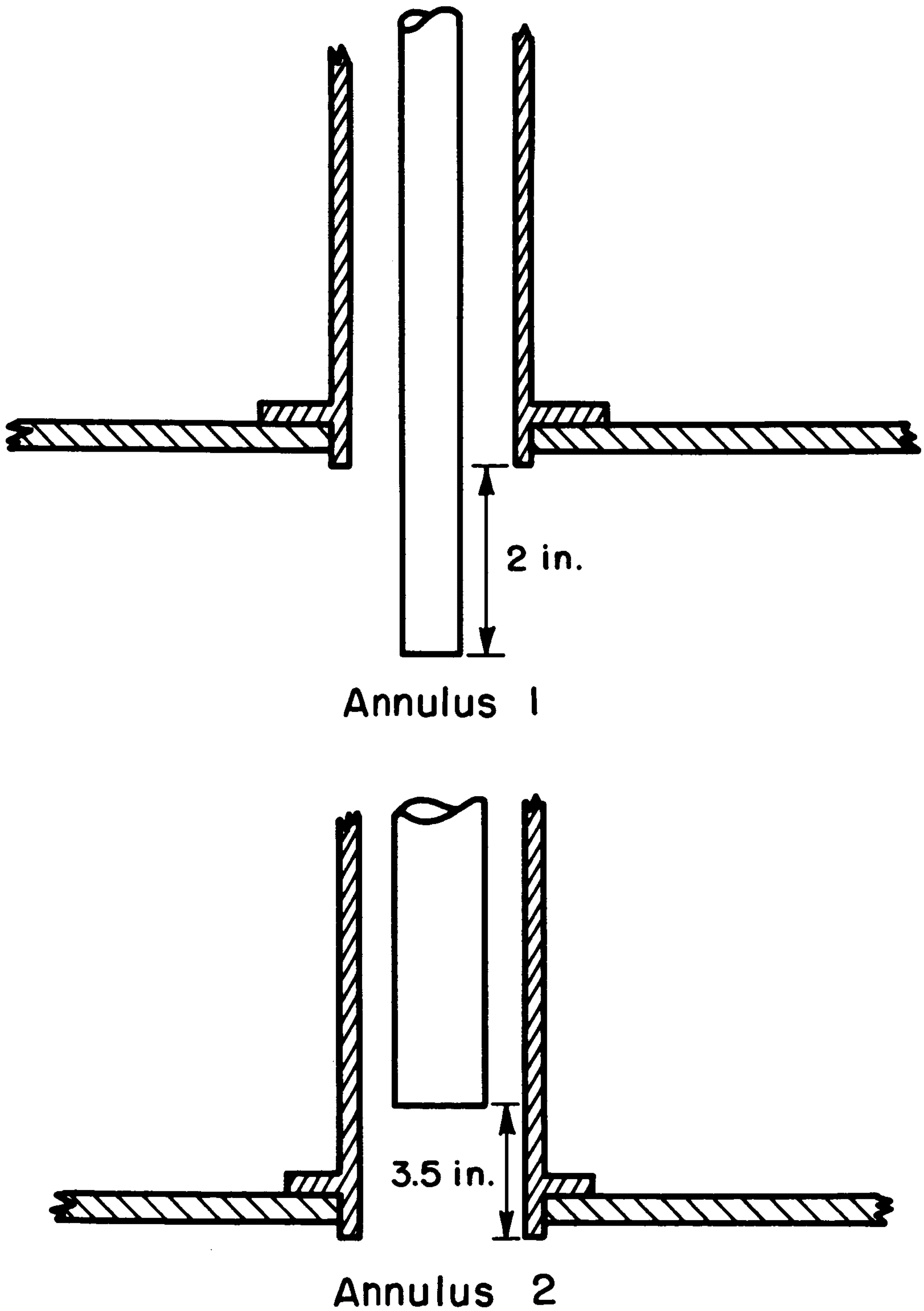

Figure 5. Exit-construction details.

obstructions to the flow were present in the entire length of the test section. With this arrangement, the maximum eccentricity was approximately 4 per cent of the passage width, a value comparable to that reported by Reynolds et al. (34).

Total-pressure-probe radial-traverse stations were located along the outer surface of the outer pipe at the axial positions listed in Table 4. Except for stations 1, 3, 4, 6, and 9, all of the radial-traverse stations were composed of 1/8-inch diameter total-head-probe access holes that were spaced circumferentially at 120° intervals and three 0.039-inch diameter static-pressure-tap holes spaced between, and 0.25 inch upstream from the access holes. Only one total-pressure-probe access hole was available at station 3. As a result of drill-tip breakage during the fabrication of the 0.039-inch static-pressure taps, only two instead of the usual three static-pressure taps were available at stations 1, 4, 6, and 9. The fact that only one total-pressure-probe hole was available at station 3 was of no consequence since an outer-pipe support located in the vicinity prevented any velocity measurements from being made there. The two static-pressure taps at stations 1, 4, 6, and 9 were sufficient for measuring average values of the static pressures at those locations. No deviations that could be

Table 4. Traverse-station location

Axial-location number	Distance from the beginning of the constant-area section, x		$\frac{x}{D_2-D_1}$			
	Rounded entrance in.	Square-edged entrance in.	Annulus 1RD	Annulus 1SQ	Annulus 2RD	Annulus 2SQ
1	6.00	5.00	2.29	1.90	3.20	2.67
2	10.0	9.00	3.81	3.43	5.33	4.80
3	14.0	13.0	5.33	4.95	7.47	6.93
4	16.5	15.5	6.29	5.90	8.80	8.27
5	20.5	19.5	7.81	7.43	10.93	10.40
6	24.5	23.5	9.33	8.95	13.07	12.53
7	28.5	27.5	10.86	10.48	15.20	14.67
8	31.5	30.5	12.00	11.62	16.80	16.27
9	37.0	36.0	14.10	13.71	19.73	19.20
10	45.0	44.0	17.14	16.76	24.00	23.47
11	53.0	52.0	20.19	19.81	28.27	27.73
12	61.0	60.0	23.24	22.86	32.53	32.00
13	65.5	64.5	24.95	24.57	34.93	34.40

attributed to this difference in number of static-pressure taps were noticed during preliminary checks made of the static-pressure taps.

The total-pressure-probe radial-traverse mechanism was constructed from brass and steel stock and is shown in Figure 6. A 2-inch travel Lufkin micrometer head with a least count of 0.0001 inch was used for positioning the total-pressure probe.

The total-pressure probe used for all of the velocity measurements was made from stainless-steel hypodermic-needle tubing. The pertinent dimensions of the probe are given in Figure 7.

All fluid-pressure measurements were made with an inclined Meriam manometer having a range of 12 inches of water and a least count of 0.01 inch of water and a Meriam micromanometer having a range of 20 inches of water and a least count of 0.001 inch of water. The 20-inch-range micromanometer was used to calibrate the 12-inch-range inclined manometer and to measure static pressures that were larger than the range of the inclined manometer. The inclined manometer was used for all static-pressure measurements within its range and all velocity-head measurements. The atmospheric-pressure measurements were made with a

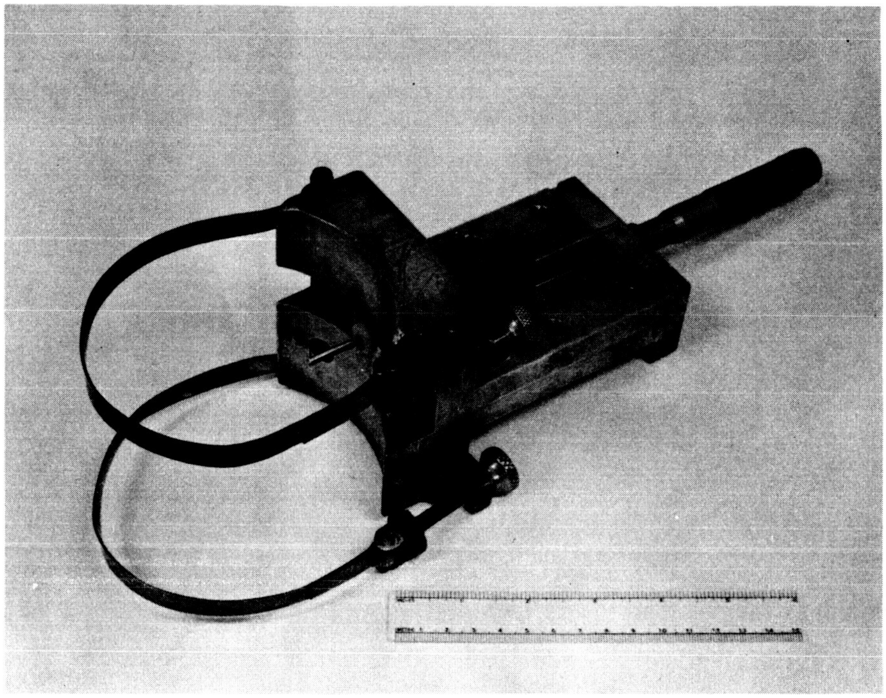

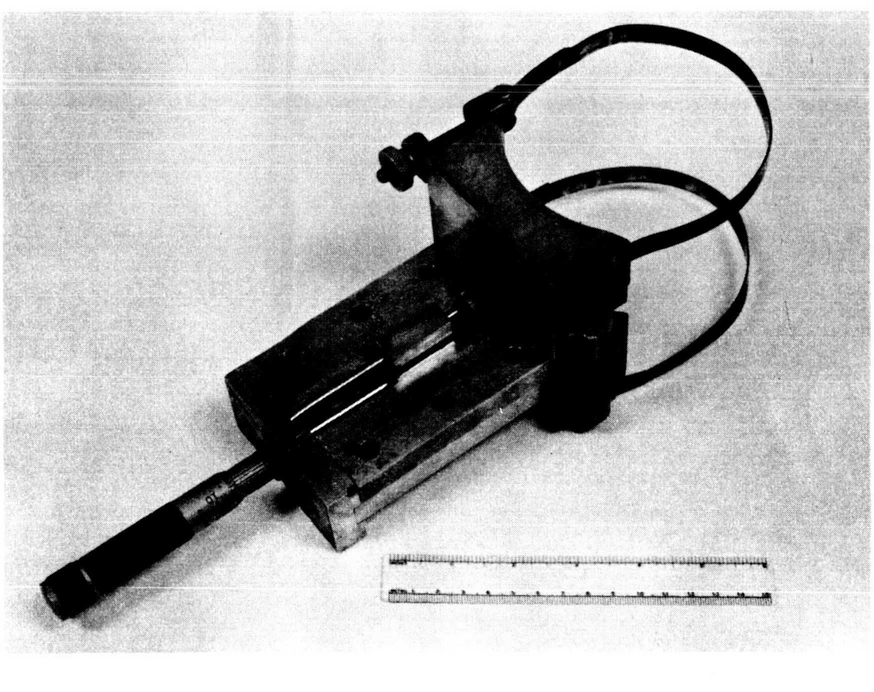

Figure 6. Total-pressure-probe radial-traverse mechanism.

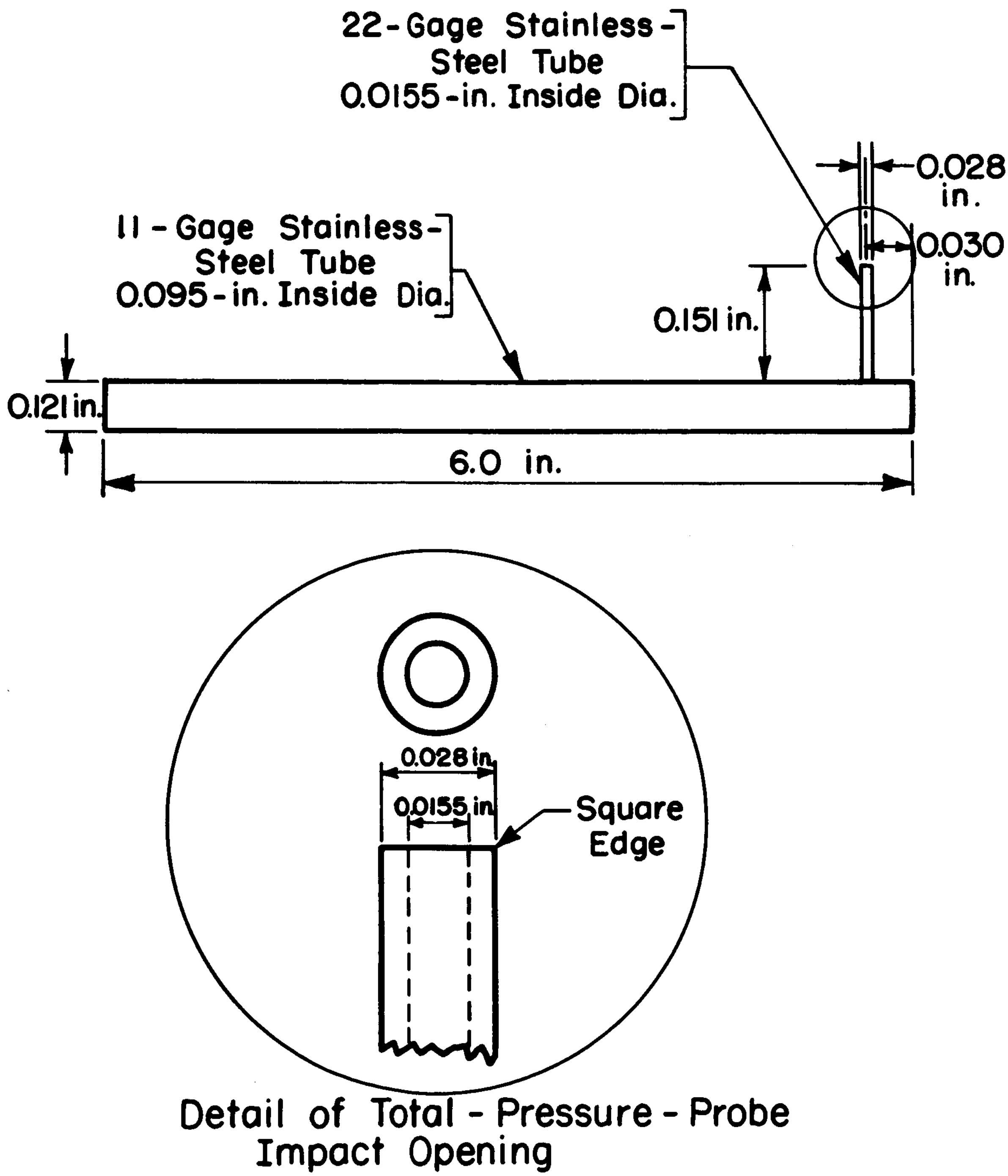

Figure 7. Total-pressure probe.

barometer having a least count of 0.001 in. Hg. Fluid-temperature measurements were made at the inlet and exit of the annuli as shown in Figure 3 with copper-constantan thermocouples and a Leeds and Northrup potentiometer that had a least count of 0.02 mv. The room temperature was measured with a mercury-in-glass thermometer having a least count of 0.5°F.

EXPERIMENTAL PROCEDURE

Data Collection

The mass flow rate of air through the annuli was regulated by throttling at the blower inlet. After a desired flow rate was attained, the apparatus was allowed to function for approximately one hour prior to making any measurements to establish approximate steady-flow conditions. The data collection was organized as indicated in Tables 5, 6, 7, and 8. The axial-location numbers correspond to those listed in Table 4. The circumferential-location letters correspond to three radial planes spaced 120^{o} apart. The 6-digit numbers without parentheses represent the velocity-traverse-run numbers with the first four digits corresponding to the month and day of the run and the last two digits signifying the sequential location of the run. All of the data were taken during the interval October 29, 1964, to February 9, 1965. The 4-digit numbers within parentheses are indicated mass-flow-rate values expressed in units of lb_m/hr. The percentages represent the percent differences between the maximum and minimum flow-rate values obtained for circumferential-and axial-sequence surveys. The Re_D values listed here and throughout the dissertation are thus nominal and

Table 5. Summary of velocity traverses in annulus 1 SQ

Axial location	High Flow Rate $Re_D \sim 161,000$			A%[a]	Medium Flow Rate $Re_D \sim 122,000$		
	Circumferential location				Circumferential location		
	N	S	W		N	S	W
1	(2454) 122309	(2460) 122311	(2378) 122310 (2435) 121901	3.46	(1943) 122907 (1963) 010401	(1849) 122909 (1847) 123001	(1875) 122908 (1907) 010501
2	(2426) 122308	(2594) 121808	(2462) 121902		(1915) 010402	(1825) 123002	(1907) 010502
3							
4							
5	(2385) 122307 (2435) 122801	(2557) 121807 (2480) 122803	(2519) 121903 (2481) 122802	1.90	(1893) 122906 (1875) 010403	(1869) 122904 (1881) 123003	(1926) 122905 (1889) 010503
6							
7	(2374) 122306	(2556) 121806	(2523) 121904		(1872) 010404	(1848) 123004	(1911) 010504
8							
9	(2410) 122305	(2567) 121805	(2520) 121905		(1874) 010405	(1890) 123005	(1898) 010505
10	(2414) 122304	(2563) 121804	(2510) 121906		(1876) 010406	(1911) 123006	(1881) 010506
11	(2400) 122303	(2557) 121803	(2511) 121907		(1870) 010407	(1899) 123007	(1883) 010507

[a]Maximum circumferential-sequence percentage difference.

2

A%[a]	Low Flow Rate $Re_D \sim 80,100$			A%[a]
	Circumferential location			
	N	S	W	
5.10	(1220) 121609			
	(1221) 121608			
3.05	(1234) 121407 (1212) 121607	(1259) 121408 (1240) 121501	(1272) 121406	3.08
	(1216) 121606	(1232) 121502	(1273) 121405	
	(1220) 121605	(1227) 121503	(1273) 121404	
	(1221) 121604			
	(1216) 121603	(1240) 121504	(1268) 121403	

Table 5 (Continued)

Axial location	High Flow Rate $Re_D \sim 161{,}000$			A%[a]	Medium Flow Rate $Re_D \sim 122{,}000$		
	Circumferential location				Circumferential location		
	N	S	W		N	S	W
12	(2403) 122302	(2584) 121802	(2534) 121908		(1877) 010408	(1921) 123008	(1880) 010508
13	(2479) 121911 (2411) 122301	(2524) 121910 (2599) 121801	(2516) 121909	1.82	(1908) 122901 (1891) 010409	(1930) 122903 (1928) 123009	(1931) 122902 (1873) 010509
B%[b]	3.38	1.69	4.05		5.00	5.65	2.02

[b]Maximum axial-sequence percentage difference.

2

$A\%^a$	Low Flow Rate $Re_D \sim 80,100$			$A\%^a$
	Circumferential location			
	N	S	W	
	(1217)	(1236)	(1268)	
	121602	121505	121402	
	(1212)	(1238)	(1240)	
1.20	121508	121506	121507	2.30
	(1224)		(1270)	
	121601		121401	
	0.99	1.88	0.40	

Table 6. Summary of velocity traverses in annulus 2 SQ

Axial location	High Flow Rate $Re_D \sim 145,000$			A%[a]	Medium Flow Rate $Re_D \sim 118,000$		
	Circumferential location				Circumferential location		
	N	S	W		N	S	W
1							
2							(2041) 103006
3							
4							
5	(2484) 111201 (2502) 111307	(2582) 111306	(2633) 111601 (2532) 111308	3.20	(1990) 103007 (2038) 110506	(2084) 103008 (2125) 110401	(2061) 103005
6							
7	(2484) 111202	(2593) 111305	(2619) 111602		(2057) 110505	(2155) 110402	(2087) 103004
8							
9	(2530) 111203	(2605) 111304	(2619) 111603		(2091) 110504	(2170) 110403	(2093) 103003
10							
11	(2512) 111204	(2630) 111303	(2613) 111604		(2080) 110503	(2192) 110404	(2126) 102903 (2093) 103001
12	(2508) 111205	(2606) 111302	(2643) 111605		(2081) 110502	(2168) 110405	(2130) 102902

[a]Maximum circumferential-sequence percentage difference.

2

A%[a]	Low Flow Rate $Re_D \sim 68,400$ Circumferential location N	S	W	A%[a]
	(1208) 112107			
4.70	(1190) 111807	(1216) 111808	(1204) 111806	2.18
	(1211) 112106	(1206) 111901		
	(1210) 112105	(1210) 111902	(1199) 111805	
	(1228) 112104	(1210) 111903	(1200) 111804	
	(1214) 112103	(1219) 111904	(1204) 111803	
	(1215) 112102	(1203) 111905	(1215) 111802	

Table 6 (Continued)

Axial location	High Flow Rate $Re_D \sim 145,000$			$A\%^a$	Medium Flow Rate $Re_D \sim 118,000$		
	Circumferential location				Circumferential location		
	N	S	W		N	S	W
13	(2527) 111206	(2565) 111208 (2602) 111301	(2553) 111207 (2645) 111606	1.50	(2094) 110408 (2091) 110501	(2164) 110406	(2126) 110407 (2134) 102901 (2097) 102904 (2082) 103002
$B\%^b$	1.85	1.85	1.22		2.60	3.15	2.54

[b]Maximum axial-sequence percentage difference.

2

A%[a]	Low Flow Rate $Re_D \sim 68,400$			A%[a]
	Circumferential location			
	N	S	W	
3.35	(1189) 111908 (1219) 112101	(1204) 111906	(1199) 111907 (1216) 111801	1.25
	1.66	1.33	1.42	

Table 7. Summary of velocity traverses in annulus 1 RD

Axial location	High Flow Rate $Re_D \sim 151,000$			A%[a]	Medium Flow Rate $Re_D \sim 121,000$		
	Circumferential location				Circumferential location		
	N	S	W		N	S	W
1							
2	(2375) 011801	(2424) 011803	(2397) 011802	2.06	(1866) 011101	(1874) 011103	(1764) 011102
	(2270) 011901		(2309) 012104		(1844) 011208		(1894) 011301
3							
4							
5	(2291) 011902	(2421) 011804	(2317) 012105		(1859) 011207	(1864) 011104	(1909) 011302
6							
7	(2312) 011903	(2417) 011805			(1877) 011206	(1826) 011210	(1899) 011209
	(2318) 012102	(2312) 012101	(2333) 012103	0.91		(1859) 011105	(1924) 011303
8							
9	(2329) 011904	(2412) 011806	(2353) 012106		(1891) 011205	(1849) 011106	(1930) 011304
10	(2332) 011905	(2411) 011807	(2349) 012107		(1900) 011204	(1851) 011107	(1917) 011305
11	(2323) 011906	(2412) 011808	(2356) 012108		(1888) 011203	(1860) 011108	(1918) 011306

[a]Maximum circumferential-sequence percentage difference.

2

A%[a]	Low Flow Rate $Re_D \sim 78,800$ Circumferential location N	 S	 W	A%[a]
6.20	(1211) 011402 (1214) 011601	(1223) 011403	(1226) 011401 (1223) 011501	1.23
	(1209) 011602	(1215) 011404	(1234) 011502	
4.00	(1215) 011603	(1223) 011610 (1209) 011405	(1244) 011609 (1233) 011503	2.38
	(1222) 011604	(1204) 011406	(1234) 011504	
	(1216) 011605	(1209) 011407	(1227) 011505	
	(1202) 011606	(1215) 011408	(1227) 011506	

Table 7 (Continued)

Axial location	High Flow Rate $Re_D \sim 151,000$			A%[a]	Medium Flow Rate $Re_D \sim 121,000$		
	Circumferential location				Circumferential location		
	N	S	W		N	S	W
12	(2320) 011907	(2378) 011809	(2363) 012109		(1893) 011202	(1862) 011109	(1922) 011307
13	(2317) 011908	(2328) 011910 (2382) 011810	(2348) 011909 (2352) 012110	1.34	(1883) 011112 (1896) 011201	(1861) 011110	(1901) 011111 (1909) 011308
B%[b]	2.73	1.94	2.34		3.02	1.35	1.90

[b]Maximum axial-sequence percentage difference.

2

A%[a]	Low Flow Rate $Re_D \sim 78,800$			A%[a]
	Circumferential location			
	N	S	W	
	(1198) 011607	(1210) 011409	(1227) 011507	
2.11	(1180) 011412 (1200) 011608	(1212) 011410	(1232) 011411 (1233) 011508	4.40
	2.00	1.58	0.90	

Table 8. Summary of velocity traverses in annulus 2 RD

Axial location	High Flow Rate $Re_D \sim 142,000$			$A\%$[a]	Medium Flow Rate $Re_D \sim 117,000$		
	Circumferential location				Circumferential location		
	N	S	W		N	S	W
1							
2	(2511) 020501 (2570) 020401	(2469) 020503	(2454) 020502 (2540) 020801	2.32	(2061) 012901 (2067) 020101	(2000) 012903	(1987) 012902 (2040) 020201
3							
4							
5	(2603) 020402	(2456) 020504	(2581) 020802		(2074) 020102	(1982) 012904	(2099) 020202
6							
7	(2604) 020403	(2454) 020505	(2584) 020803		(2087) 020103	(1978) 012905	(2100) 020203
8							
9	(2470) 020901 (2603) 020404	(2516) 020903 (2437) 020506	(2459) 020902 (2584) 020804	2.32	(2100) 020208 (2096) 020104	(2032) 020209 (1972) 012906	(2095) 020204
10	(2566) 020405		(2562) 020805		(2085) 020105	(2009) 012907	
11	(2528) 020406	(2454) 020507	(2542) 020806		(2080) 020106	(2028) 012908	(2093) 020205

[a]Maximum circumferential-sequence percentage difference.

2

A%[a]	Low Flow Rate $Re_D \sim 67,700$ Circumferential location N	S	W	A%[a]
3.72	(1191) 012601 (1221) 012801	(1174) 012603	(1192) 012602 (1193) 012701	1.53
	(1217) 012802	(1169) 012604	(1204) 012702	
	(1223) 012803	(1167) 012605	(1204) 012703	
3.35	(1194) 012709 (1233) 012804	(1158) 012710 (1163) 012606	(1202) 012704	3.80
	(1222) 012805	(1177) 012607	(1193) 012705	
	(1208) 012806	(1188) 012608	(1196) 012706	

Table 8 (Continued)

Axial location	High Flow Rate $Re_D \sim 142{,}000$			A%[a]	Medium Flow Rate $Re_D \sim 117{,}000$		
	Circumferential location				Circumferential location		
	N	S	W		N	S	W
12	(2508) 020407	(2453) 020508	(2574) 020807		(2062) 020107	(2021) 012909	(2101) 020206
13	(2490) 020809 (2486) 020408	(2494) 020810 (2456) 020509	(2556) 020808	2.65	(2061) 020108	(2029) 020110 (2027) 012910	(2095) 020109 (2096) 020207
B%[b]	4.75	1.30	1.73		1.70	2.84	3.00

[b]Maximum axial-sequence percentage difference.

2

A%[a]	Low Flow Rate $Re_D \sim 67,700$ Circumferential location N	S	W	A%[a]
	(1201) 012807	(1186) 012609	(1200) 012707	
3.25	(1182) 012612 (1200) 012808	(1185) 012610	(1205) 012611 (1194) 012708	1.95
	2.75	2.24	0.92	

represent rounded-off approximations of the true Re_D values.

Each velocity-traverse run consisted of velocity-pressure-head measurements along a radius, an average static-pressure measurement, fluid-temperature measurements, a room-temperature measurement, and an atmospheric-pressure measurement. The zero position for the total-pressure-probe impact-pressure opening was determined for each run by allowing the probe to butt up against the inner wall of the annulus. The zero location could be duplicated repeatedly to within 0.002 inch. The probe was aligned axially by eye. At the end of each run, key velocity-pressure and static-pressure measurements were checked. The checks showed that the flow rate and profile shape were not changing appreciably over the time required to obtain a single velocity traverse.

One complete set of outer-wall-tap pressure measurements along the axis was made for each distinct Re_D, annulus, and entrance combination.

Data Reduction

The data were reduced by using the equations and techniques mentioned in Appendix A. Since mean point velocities were involved in most of the results, the assumptions associated with the calculation of the axial point velocities are discussed further. The point velocities were obtained from direct velocity-pressure-head measurements. The total-pressure-probe velocity coefficient was assumed equal to 1.0 since no general calibration information that included the effects of the many variables involved was available. This assumption probably had a negligible effect on the results since the velocity ratios, $\frac{u}{U_a}$ and $\frac{u}{U}$, were frequently involved. The flow was assumed incompressible as justified by Dean (12) for Mach numbers less that 0.2. The maximum velocity measured during the present investigation was approximately 180 ft/sec, which corresponds to a Mach number of 0.164. The minimum distance from the inner wall to the geometric center of the total-pressure-probe impact hole was 0.03 inch. For velocity measurements made at this distance from the wall, MacMillan's (28) data suggest applying a displacement correction of approximately 0.0035 inch, while Davies' (11) data suggest making no displacement correction. Since the probe could be positioned to within .002 inch only, no displacement correction was applied to the data. Finally, the velocity-pressure-head measurements were made with the assumption that the radial variations of static pressure were negligible. Although radial static-pressure variations probably did exist, especially near the annuli inlets, the present state of flow instrumentation does not allow precise static-pressure measurements to be made in relatively narrow internal passages. Judging from the mass flow rate values as shown in Tables 5, 6, 7, and 8, the assumption did not lead to serious discrepancies.

DISCUSSION OF EXPERIMENTAL RESULTS

Propagation of Uncertainty

When a large number of observations of a particular variable is available, an estimate of the true value of the variable and the reliability of this estimate can be calculated statistically. The same technique cannot, however, be applied to the observations of a single-sample investigation. Kline and McClintock (23) recommend that for single-sample observations, the experimenter should state what he thinks the reliability of his single observation of a particular variable is and report that observation with an uncertainty interval based on chosen odds. For example, following their suggestion, a single observation of a variable would be reported as

$$\text{variable} = \text{observed value} \pm \epsilon \ (\eta \text{ to } 1) \tag{39}$$

to imply that the observed value is believed to be the best estimate of the true value of the variable and that the odds are η to 1 that the true value of the variable lies within $\pm\ \epsilon$ of the observed value.

If F is a linear function of independent variables a, b, c, ..., and i, each of which is normally distributed, then

Kline and McClintock (23) suggest using the relationship

$$\epsilon_F^2 = (\frac{\partial F}{\partial a} \epsilon_a)^2 + (\frac{\partial F}{\partial b} \epsilon_b)^2 + \ldots + (\frac{\partial F}{\partial i} \epsilon_i)^2 \qquad (40)$$

for determining the propagation of observation uncertainty intervals into the result. They further state that if the same odds were used for all of the observation uncertainty intervals, then it could also be used for describing the reliability of the uncertainty interval associated with the calculated result. If the uncertainty intervals are small, the linear function restriction can be relaxed.

The following estimates were made about one set of typical measurements:

$$p_{ATM} = 13.95 \pm 0.01 \text{ psia (20 to 1)}$$

$$t_{ROOM} = 70.2 \pm 0.5^{o}F \text{ (20 to 1)}$$

$$T_{AIR} = 530.0 \pm 0.5^{o}R \text{ (20 to 1)}$$

$$p_{GAGE} = 0.4200 \pm 0.0004 \text{ psia (20 to 1)}$$

The corresponding air density was calculated, as shown in Appendix A, to be

$$\rho = 0.0710 \pm 0.000085 \frac{lb_m}{ft^3} \text{ (20 to 1)}$$

Thus, at 20 to 1 odds, the uncertainty interval associated with the calculated ρ_{AIR} is essentially negligible. For $\Delta h_v = 1.00 \pm 0.01$ inch H_2O (20 to 1) and the values above, the mean axial velocity was found to be 68.5 ± 0.4 ft/sec (20 to 1). The uncertainty interval is approximately $\pm$ 0.6% of the velocity. For $\Delta h_v = 7.00 \pm 0.03$ inch H_2O (20 to 1) and the values above, the velocity was calculated to be 180 ± 0.4 ft/sec (20 to 1). The uncertainty interval is $\pm$ 0.23% of the result. Strictly speaking, these results are valid for the particular measurements considered. However, it was assumed that they could be used for the other similar measurements and mean velocities of the present investigation as estimates.

Estimates of the uncertainty intervals associated with some of the calculated results are given throughout the discussion. No estimates of uncertainty intervals were calculated for the results involving numerical integrations. The quantities used in the numerical integrations were mean velocities, radii, and air densities. As mentioned previously the uncertainty intervals based on 20 to 1 odds associated with the mean velocities and air densities were small. The maximum uncertainty interval based on 20 to 1 odds associated with the radius measurements was estimated to be in the order of 0.15% of the radius measurement. Further, for any particular quantity, the uncertainty distribution was assumed to be symmetric with respect to the estimated true value. Therefore, it seems reasonable to assume that the results of the numerical integrations were reliable values.

Velocity-Profile Data

General remarks

The conclusions about the behavior of the velocity profiles obtained during the present investigation were drawn on the basis of plots of the reduced data on $\frac{u}{U_a}$ and $\frac{r-r_1}{r_2-r_1}$ coordinates. Thus, a criterion that established significant and insignificant differences of compared results was necessary. The maximum uncertainty interval for 20 to 1 odds associated with u was estimated to be in the order of $\pm$ 0.6% of u. It therefore seemed reasonable to estimate that the uncertainty interval for 20 to 1 odds associated with $\frac{u}{U_a}$ would not exceed $\pm$ 1.0% of $\frac{u}{U_a}$. Thus, differences in profiles that exceeded 2% on the $\frac{u}{U_a}$ coordinate were considered significant. The $\frac{u}{U_a}$ scale used in Figures 8 through 14, and 19 through 32, allowed for differences of

0.01 to be detected. The maximum uncertainty interval for 20 to 1 odds associated with any one value of $\frac{r-r_1}{r_2-r_1}$ was estimated to be $\pm$ 0.01. The $\frac{r-r_1}{r_2-r_1}$ scale used in Figures 8 through 14 and 19 through 32 had a least count of 0.02 and was therefore consistent with the estimated uncertainty interval of the parameter. The $\frac{u}{U_a}$ and $\frac{r-r_1}{r_2-r_1}$ scales for Figures 15, 17, and 33 through 42 were expanded so that the trends exhibited by the various profiles could be seen more clearly.

Square-edged-entrance annuli

Velocity profiles measured on different days at the same location and flow rate (within 5%) were compared to check the repeatability of flow development in annuli 1SQ and 2SQ. The conclusion drawn from the comparison of profiles was that the flow development in annuli 1SQ and 2 SQ could be readily repeated. Sample comparisons are shown in Figure 8 for annulus 1SQ and Figure 9 for annulus 2SQ.

The results of the circumferential-sequence velocity-profile measurements made in annulus 1SQ are shown in Figures 10, 11, and 12. At distances of 1.9 and 7.43 hydraulic diameters from the entrance, the flow development in annulus

1SQ was not exactly axisymmetric. However, at a distance of 24.57 hydraulic diameters from the entrance of annulus 1SQ, the velocity-profile shapes compared favorably. The results of the circumferential-sequence velocity-profile measurements made in annulus 2SQ are shown in Figures 13 and 14. At a distance of 10.4 hydraulic diameters from the entrance, the flow development in annulus 2SQ was not exactly axisymmetric. The profile shapes for the flow at a distance of 34.4 hydraulic diameters from the inlet of annulus 2SQ were quite similar. The non-regularity of the asymmetry of velocity profiles with changes in Re_D led the author to believe that "constant" system characteristics were not the cause of the differences in flow development along the three radial planes. Also, the Re_D effect on profile shape was not consistent. For example, as demonstrated in Figure 10, the shape of the velocity profile measured at survey location 1S was affected appreciably by the change in nominal Re_D from 160,000 to 120,000 while the shape of the velocity profile measured at survey location 1N was unaffected by the same change in nominal Re_D. At distances of 24.57 and 34.4 hydraulic diameters from the entrances of annuli 1SQ and 2SQ respectively, the circumferential-sequence surveys showed that changes in Re_D over the respective ranges did not affect the shape of the velocity profile.

Typical axial-sequence velocity-profile data obtained in annuli 1SQ and 2SQ are shown in Figures 15 through 18. The trends indicated by the sample data shown are indicative of the trends exhibited by all of the data. There appeared to be no regular Re_D effect on the development trends. It was discovered, however, that the shapes of the velocity profiles were not changing noticeably beyond 19.81 and 27.73 hydraulic diameters of development length in annuli 1SQ and 2SQ respectively. The results of the study of profile-shape changes after 19.81 and 27.73 hydraulic diameters of development length are shown in Figures 19 through 24. These axial comparisons combined with the circumferential comparisons of Figure 12 and Figure 14 lead to the conclusion that fully developed mean-velocity profiles were apparently obtained in annuli 1SQ and 2SQ after approximately 20 and 30 hydraulic diameters of development.

Rounded-entrance annuli

Velocity profiles measured on different days at the same location and flow rate (within 5%) were compared to check the repeatability of flow development in annuli 1RD and 2RD. Apparently, the flow development in annuli 1RD and 2RD could not be repeated consistently. In some instances, the comparisons indicated noticeable changes in profile shape; while in others, no noticeable changes were observed. No regular pattern could be detected. A few sample comparisons are shown in Figure 25 and Figure 26. As mentioned previously in the Experimental Procedure section, key measurements repeated during single-velocity-profile runs indicated that no measurable changes in velocity-profile shape occurred over the time interval required to obtain a single velocity profile.

The circumferential-sequence velocity profiles obtained for the flow through annuli 1RD and 2RD are shown in Figures 27, 28, 29, 30, 31, and 32. The flow development in both annuli 1RD and 2RD was not identical along the three radial planes. Slight differences in development occurred at all of the axial distances where measurements were taken. Apparently, 24.95 and 34.93 hydraulic diameters of development length were not sufficient amounts to obtain fully developed velocity profiles in annuli 1RD and 2RD respectively. The Re_D effect on profile shape was not regular. Turbulent-velocity-fluctuation measurements would have shed light on the seemingly irregular changes that did occur in the velocity profiles when the Re_D was changed.

Trends of flow development in annuli 1RD and 2RD were sought by comparing first the development patterns along the three radial planes for constant Re_D values and then the development patterns along a specific radial plane for various Re_D values. No regular trends could be detected. In general, the downstream development patterns depended on the stage of profile development achieved in the portion of the annulus close to the entrance. One possible explanation of the irregularity is the behavior of transition from laminar to turbulent flow. It is quite probable that transition occurred in the developing boundary layers near the entrance. The occurrence of boundary-layer transition also serves as an explanation of the non-repeatability of the flow development in the rounded-entrance annuli. In Figures 33 to 42, the results of some of the axial-sequence velocity-profile data are shown. The profile-development patterns along three radial planes at a constant Re_D and along a specific radial plane for various Re_D values are included for annuli 1RD and 2RD. It is interesting to note that the velocities near the radius of maximum velocity decreased with axial distance in portions of annulus 2RD. This same effect was demonstrated by the data of Barbin and Jones (3) and attributed to insufficient development of Reynolds stresses near the wall by Karl Brenkert, Jr. in a discussion of that paper.

The axial variation of boundary-layer displacement thickness was also quite dependent upon the location of transition as shown in Figures 43 to 46. The displacement-thickness data correspond to the axial-sequence velocity-profile data shown in Figures 33 to 42 and were calculated as shown in Appendix A.

Pressure-Drop Data

Obtaining reliable gradient information from experimental data is difficult because of the extreme precision required in measuring the small differences involved. For example, it is possible to calculate the pressure gradient in the portion of annulus 2SQ where the variation of static pressure with length was approximately linear, with the high-Re_D static-pressure measurements obtained at axial locations 12 and 13 as listed in Appendix D. The result is $-0.0220 \frac{\text{in. } H_2O}{\text{in.}}$. The uncertainty intervals for 20 to 1 odds associated with the static-pressure and length measurements were estimated to be $\pm$ 0.01 inch H_2O and $\pm$ 0.05 inch respectively. With these, the uncertainty interval for 20 to 1 odds associated with the gradient above was calculated to be $\pm 0.0035 \frac{\text{inch } H_2O}{\text{inch}}$ or nearly $\pm$ 16% of the gradient. If data obtained over a wider spacing, for example at axial stations 11 and 13, were used, the quantities in the numerator and denominator would be larger; and, thus, the uncertainty interval of the result would be smaller as long as the same precision were maintained in the measurements. The gradient and uncertainty interval for 20 to 1 odds obtained from the data obtained over a wider spacing was found to be -0.0240 $\pm$ 0.0011 $\frac{\text{inch } H_2O}{\text{inch}}$. The uncertainty interval is only $\pm$ 5% of the gradient. Finally, if the data obtained over the same spacing but for a lower Re_D were used, the error of the result would again be large because of the smaller Δh_s. From the low-Re_D data of annulus 2SQ, the pressure gradient and uncertainty interval for 20 to 1 odds were calculated to be -0.0064 $\pm$ 0.0011 $\frac{\text{inch } H_2O}{\text{inch}}$. The uncertainty interval is nearly $\pm$ 18% of the gradient.

In an effort to obtain pressure gradients that were reasonably precise, the cubic-spline curve-fitting computer program of Fowler and Wilson (15) was used instead of the difference technique illustrated above. Still, as expected, the gradients computed from the data involved a definite amount of scatter that was largest for the low-Re_D values. Nevertheless, the trends indicated by all of the gradient information were similar and are demonstrated in Figures 47 and 48. The trends are in agreement with those demonstrated by the data of Olson and Sparrow (31). The decrease in pressure gradient near the entrance for flow through the rounded entrances can be interpreted as an indication of boundary-layer transition. According to Olson and Sparrow, installation of boundary-layer tripping devices at the entrance of an annulus with a rounded inlet results in no decrease in pressure gradient as suggested by the dotted lines.

Irrotational-Flow Parameter

As mentioned in the Analysis section, a fundamental assumption made in solving boundary-layer problems is the existence of an irrotational-flow field external to the boundary layer. The gage-pressure Bernoulli constant was calculated from the experimental data and graphed as a function of axial location to determine whether or not irrotational flow existed in the upstream portion of the annuli with rounded inlets. The uncertainty interval for 20 to 1 odds associated with the ratio$\left(\frac{U^2}{2g_c} + \frac{P_{GAGE}}{\rho_{AIR}}\right)/$

$\left(\frac{U}{2g_c} + \frac{P_{GAGE}}{\rho_{AIR}}\right)_{ENTRANCE}$ was estimated to be in the order of $\pm$ 0.015. Thus, parameter changes greater than 0.03 were considered significant. All of the data exhibited the trends indicated by the curves of Figure 49. In annuli 2RD and 1RD irrotational-flow fields apparently existed in the initial 10 to 14 hydraulic diameters of development length over the Re_D range. Because of energy dissipation, the magnitude of the term $\frac{P_{ATM}}{\rho_{AIR}} + \frac{P_{GAGE}}{\rho_{AIR}} + \frac{U^2}{2g_c}$ should decrease with distance from the inlet in the portion of the annulus where the flow is no longer irrotational. The corresponding change of $\frac{P_{GAGE}}{\rho_{AIR}} + \frac{U^2}{2g_c}$ is an increase in magnitude since it is a negative quantity. Thus the increase in magnitude of the term $\left(\frac{P_{GAGE}}{\rho_{AIR}} + \frac{U^2}{2g_c}\right) / \left(\frac{P_{GAGE}}{\rho_{AIR}} + \frac{U^2}{2g_c}\right)_{ENTRANCE}$ with x, as exhibited by the curves of Figure 49, is consistent with energy considerations. The term $\frac{P_{ATM}}{\rho_{AIR}}$ was not included in the present results because of its size in comparison with the magnitudes of $\frac{P_{GAGE}}{\rho_{AIR}}$ and

$\frac{U^2}{2g_c}$. For example, with p_{ATM} = (14.37)(144)psfa and ρ_{AIR} = 0.071 lb_m/ft^3, $\frac{p_{ATM}}{\rho_{AIR}} = 29{,}300 \frac{lb_f}{lb_m ft}$. The maximum values of $\frac{p_{GAGE}}{\rho_{AIR}}$ and $\frac{U^2}{2g_c}$ encountered during the present investigation were -1200 and 500 $\frac{lb_f}{lb_m ft}$ respectively.

Approximate Boundary-Layer-Thickness Parameters

In the Analysis section, the approximate equations for the boundary-layer momentum-thickness parameters were used in obtaining the differential equation for the boundary layer. The result was a boundary-layer differential equation very similar in form to the one for boundary-layer flow over an infinite flat plate. In Table 9 some of the corresponding numerical values of the exact and approximate boundary-layer-thickness parameters are compared. The differences between the two increased with distance along the annulus, as expected. The maximum discrepancy was approximately 5%.

Shape-Factor Results

As mentioned in the text by Schlichting (40), the transition region for flat-plate boundary layers is characterized

Table 9. Comparison of exact and approximate boundary-layer-thic

$\frac{x}{D_H}$	Approximate displacement-thickness parameter		Exact displacement-thickness parameter		Approximate momentum-thickness parameter	
	Inner surface	Outer surface	Inner surface	Outer surface	Inner surface	Outer surface
3.81	0.0158	0.0295	0.0156	0.0298	0.00398	0.0177
7.81	0.0310	0.0441	0.0301	0.0448	0.0164	0.0311
10.86	0.0399	0.0519	0.0385	0.0528	0.0238	0.0354
14.10	0.0477	0.0556	0.0457	0.0567	0.0304	0.0401
17.14	0.0530	0.0624	0.0505	0.0638	0.0349	0.0419
3.81	0.0163	0.0269	0.0161	0.0272	0.00424	0.0154
7.81	0.031	0.0407	0.0302	0.0412	0.0167	0.0277
10.86	0.0424	0.0517	0.0408	0.0526	0.026	0.0351
14.10	0.0512	0.0625	0.0489	0.0638	0.0332	0.0428
17.14	0.0553	0.0720	0.0526	0.0737	0.0368	0.0484
5.33	0.0286	0.0348	0.0283	0.035	0.0109	0.0194
10.93	0.0525	0.0414	0.0514	0.0418	0.0302	0.0261
15.20	0.0637	0.0492	0.0620	0.0498	0.0394	0.0287
5.33	0.0283	0.0362	0.0279	0.0365	0.0101	0.0213
10.93	0.0529	0.0469	0.0517	0.0474	0.0307	0.0301
15.20	0.0656	0.0562	0.0638	0.057	0.0412	0.0352

2

kness parameters

Exact momentum-thickness parameter: Inner surface	Outer surface	
0.00397	0.0178	
0.0162	0.0314	Annulus 1RD
0.0233	0.0358	$Re_D \sim 150,000$
0.0295	0.0406	
0.0338	0.0425	
0.00422	0.0155	
0.0164	0.0280	Annulus 1RD
0.0254	0.0355	$Re_D \sim 80,000$
0.0322	0.0434	
0.0356	0.0492	
0.0108	0.0195	
0.0298	0.0262	Annulus 2RD
0.0388	0.0289	$Re_D \sim 145,000$
0.0100	0.0214	
0.0303	0.0304	Annulus 2RD
0.0404	0.0355	$Re_D \sim 70,000$

by large changes in the shape factor or ratio of displacement thickness to momentum thickness. For example, according to Schlichting, the transition region in a flat-plate boundary layer is characterized by a drop in value of the shape factor from 2.6 in the laminar boundary layer to 1.4 in the turbulent boundary layer. The results shown in Figures 50 and 51 indicate, then, that boundary-layer transition occurred in annuli 1RD and 2RD near the inlet. The effects of transition were measured at the initial velocity-traverse stations 3.81 and 5.33 hydraulic diameters downstream from the throats of the converging inlets of annuli 1RD and 2RD respectively. For both annuli with rounded entrances, transition apparently occurred closer to the entrance on the outer wall than on the inner wall. The increase in spread of values near the entrance can be interpreted as an indication of the intermittent nature of the transition process.

Friction-Factor Results

The local skin-friction factor can be defined as follows

$$f = \frac{2\tau_o g_c}{\rho U^2} \tag{41}$$

The momentum-integral equation for the inner-wall boundary layer is

$$-d\left(\int_{r_1}^{r_m} \frac{2\rho u^2 r dr}{g_c}\right) + U d\left(\int_{r_1}^{r_m} \frac{2\rho u r dr}{g_c}\right) = \tau_{01} 2r_1 dx + dp(r_m^2 - r_1^2) \quad (42)$$

For the outer wall, the equation is

$$-d\left(\int_{r_m}^{r_2} \frac{2\rho u^2 r dr}{g_c}\right) + U d\left(\int_{r_m}^{r_2} \frac{2\rho u r dr}{g_c}\right) = \tau_{02} 2r_2 dx + dp(r_2^2 - r_m^2) \quad (43)$$

Barbin's (2) data indicated that changes in momentum flux were negligible for flow development in a pipe for $\frac{x}{D} > 1.5$. Thus changes in the momentum flux for the developing boundary layers in an annulus with a rounded entrance should also be approximately constant for $\frac{x}{D_H}$ values sufficiently large when the annulus is divided into two portions of flow separated by the plane of maximum velocity. Also, since the plane of maximum velocity is always characterized by $\frac{du}{dr} = 0$, the changes in mass flow rate through the outer and inner portions of the annulus should also be negligible. The trends indicated by the curves of Figures 52, 53, 54, and 55 were followed by all of the data. Thus, for $\frac{x}{D_H} > 3.81$ for annulus 1RD and $\frac{x}{D_H} > 5.33$ for annulus 2RD, changes in momentum flux and partial flow rate were apparently negligible within the portions of the annulus passage divided by the plane of maximum velocity. Thus, for the inner and outer walls, the wall shear stresses could be evaluated with the equations

$$\tau_{01} = -\left(\frac{r_m^2 - r_1^2}{2r_1}\right)\frac{dp}{dx} \qquad (44)$$

and

$$\tau_{02} = -\left(\frac{r_2^2 - r_m^2}{2r_2}\right)\frac{dp}{dx} \qquad (45)$$

Or, in terms of local skin-friction coefficients

$$f_1 = -\left(\frac{r_m^2 - r_1^2}{2r_1}\right)\frac{2g_c}{\rho U^2}\frac{dp}{dx} \qquad (46)$$

and

$$f_2 = -\left(\frac{r_2^2 - r_m^2}{2r_2}\right)\frac{2g_c}{\rho U^2}\frac{dp}{dx} \qquad (47)$$

As mentioned previously, the $\frac{dp}{dx}$ results obtained from the static-pressure-drop data are approximate because of the difficulty involved in calculating gradients. Further, r_m is not easily determined from experimental velocity data. The r_m values used in obtaining the results shown in Figures 56 and 57 were 1.239 and 1.503 inches for annuli 1RD and 2RD respectively. These values seem to be best suited for the present data and are compared in Table 10 with the values suggested by Brighton and Jones (5) and laminar-flow theory.

Table 10. Comparison of radii of maximum velocity

r_1/r_2	Present values inches	Laminar-flow values inches	Brighton and Jones' values inches
0.344	1.239	1.2852	1.222
0.531	1.503	1.5065	1.484

Thus, the local-friction-factor data shown in Figures 56 and 57 should be used quantitatively with caution. The decrease in local friction factors for Re_x values less the 6×10^5 can be interpreted as an effect of the transition occurring in the boundary layer. The trend demonstrated by the local-friction-factor data is similar to the one displayed by the data of Shapiro and Smith (42). Typical calculated Re_x values and uncertainty intervals were calculated to be 327,000 ± 2300 and 5,700,000 ± 14,700 for 20 to 1 odds. At the low end the uncertainty interval is ± 0.70% of the result; while at the high end, it is only ± 0.25% of the result.

The average local friction factor can be defined as

$$f_{AVE} = -\left(\frac{D_2 - D_1}{2\rho U_a^2}\right) g_c \frac{dp}{dx} \tag{48}$$

The values of f_{AVE} for axial station 12 were calculated from the static-pressure-drop data and appear to be consistent with the fully developed annular-flow results of Brighton and Jones (5), as shown in Figure 58. The values for station 12 instead of station 13 were chosen because they were determined from data obtained both upstream and downstream from the measuring station.

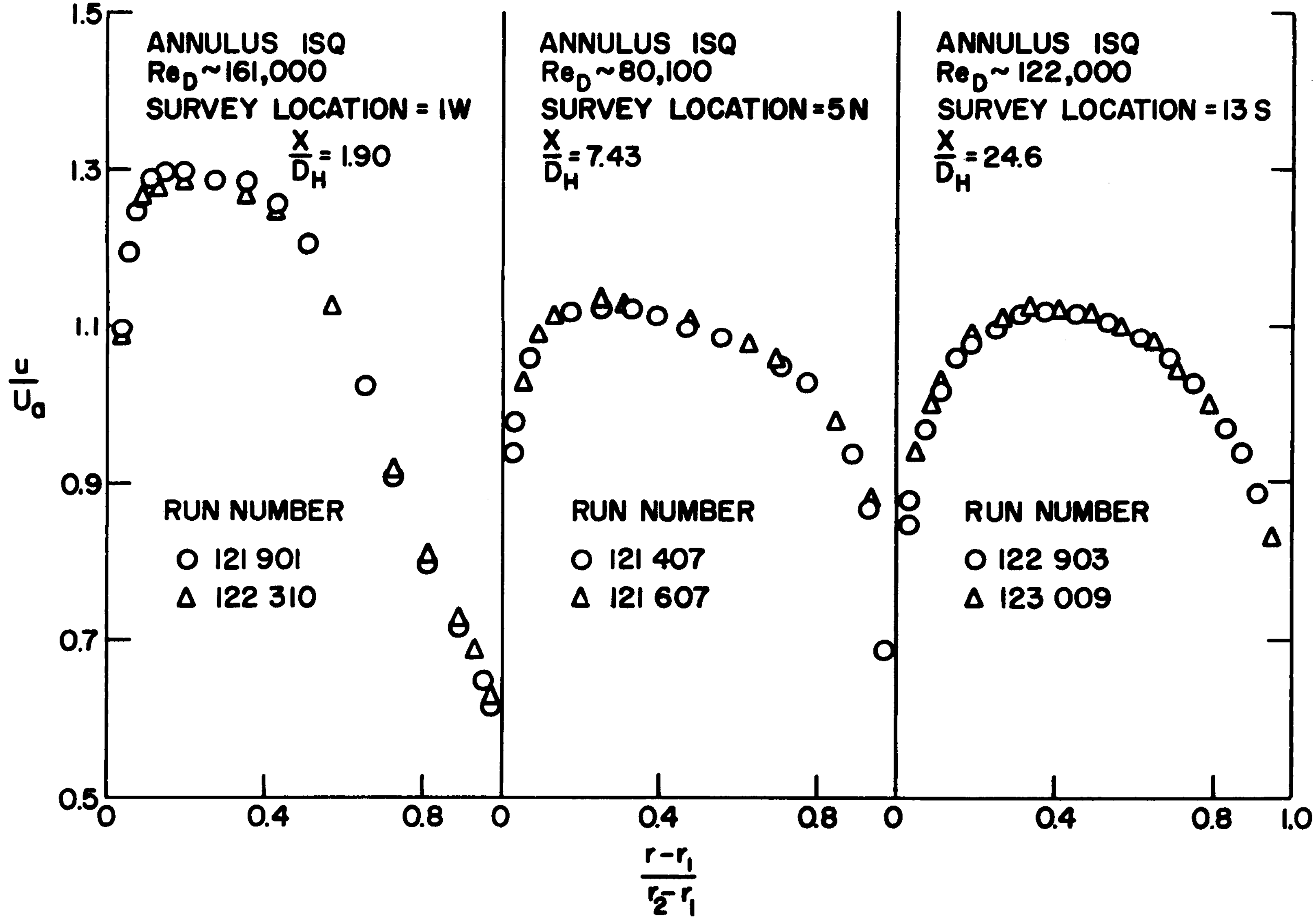

Figure 8. Typical time-sequence velocity profiles for annulus 1 SQ.

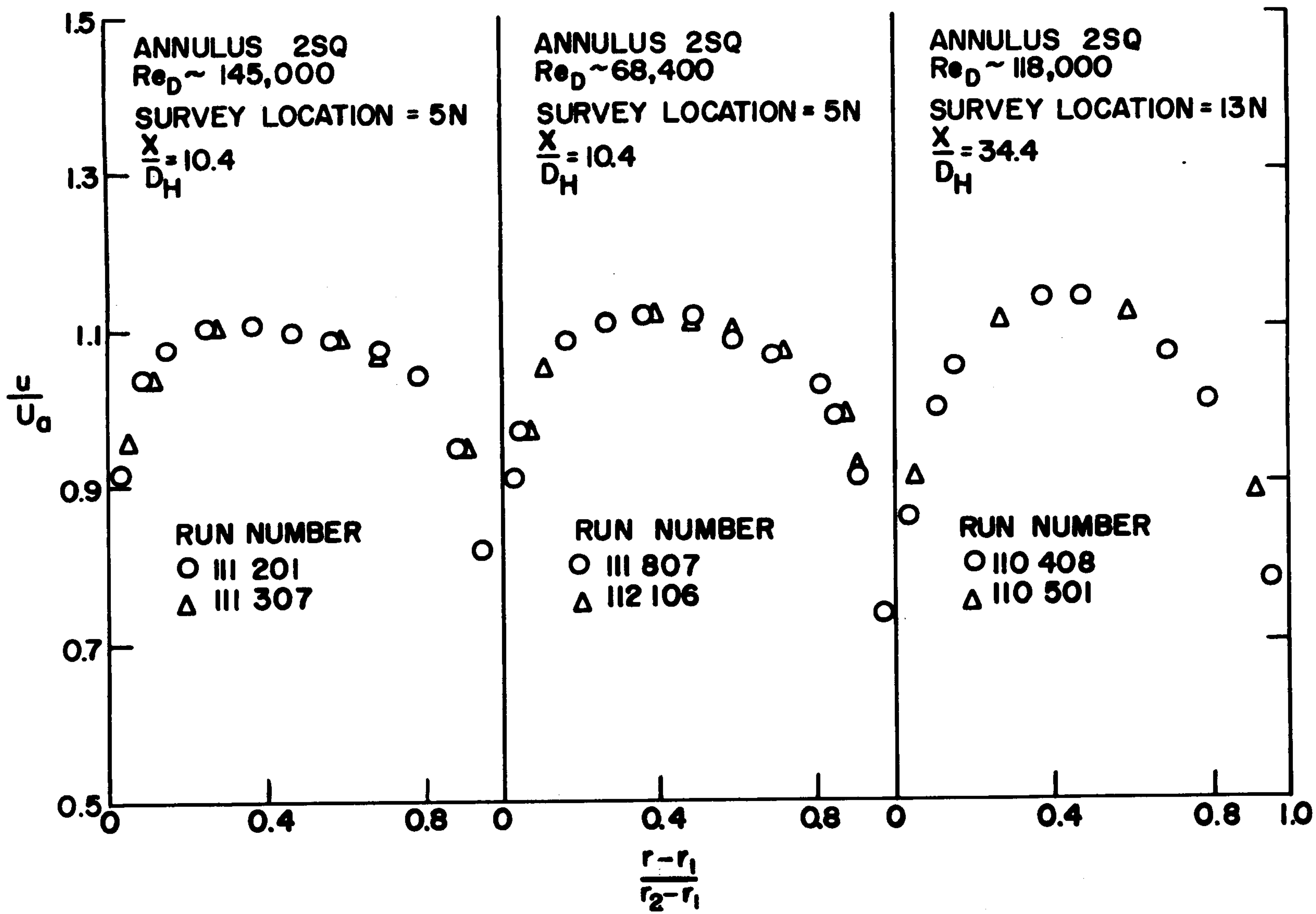

Figure 9. Typical time-sequence velocity profiles for annulus 2 SQ.

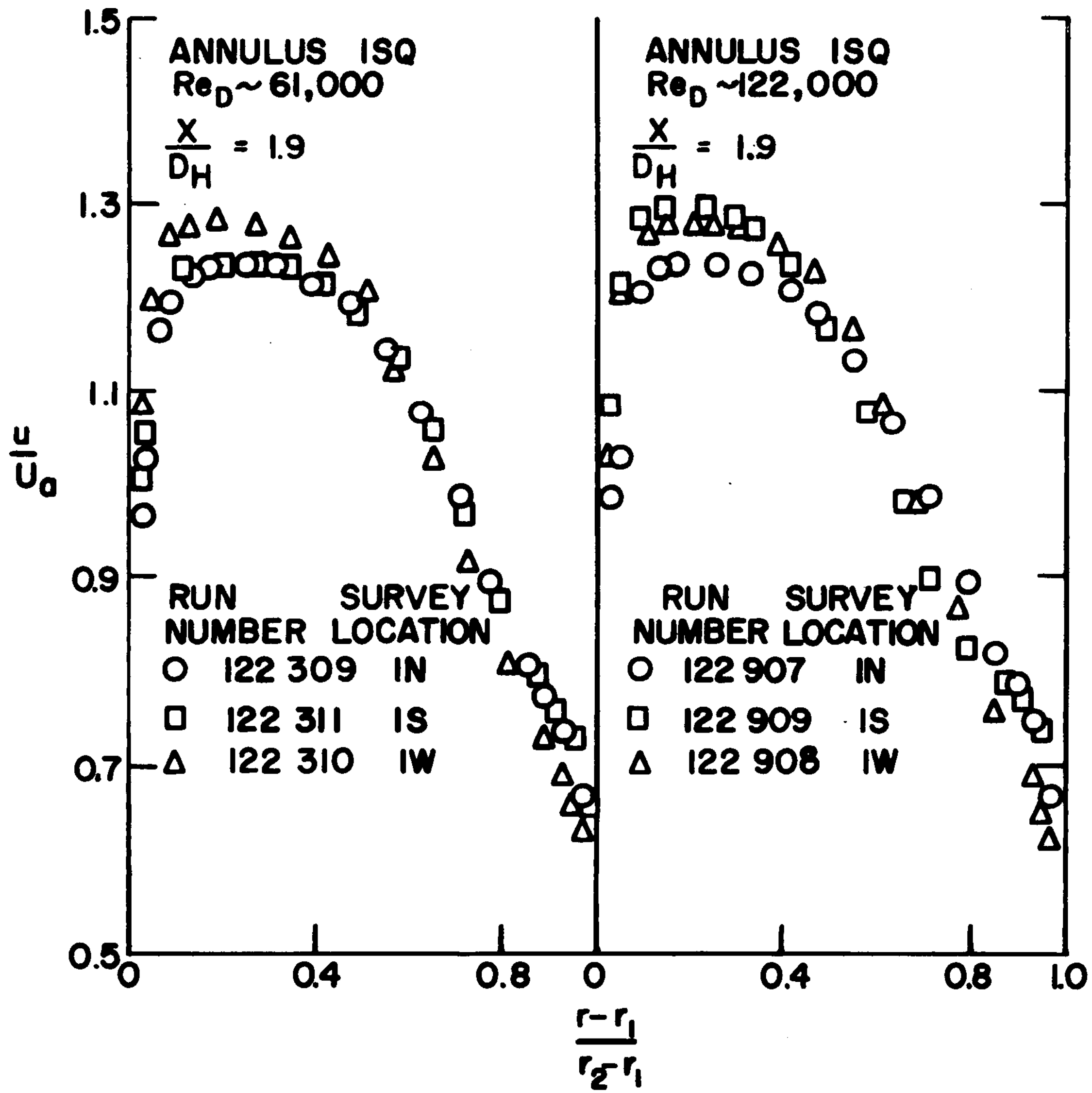

Figure 10. Circumferential-sequence velocity profiles for axial location 1 of annulus 1 SQ.

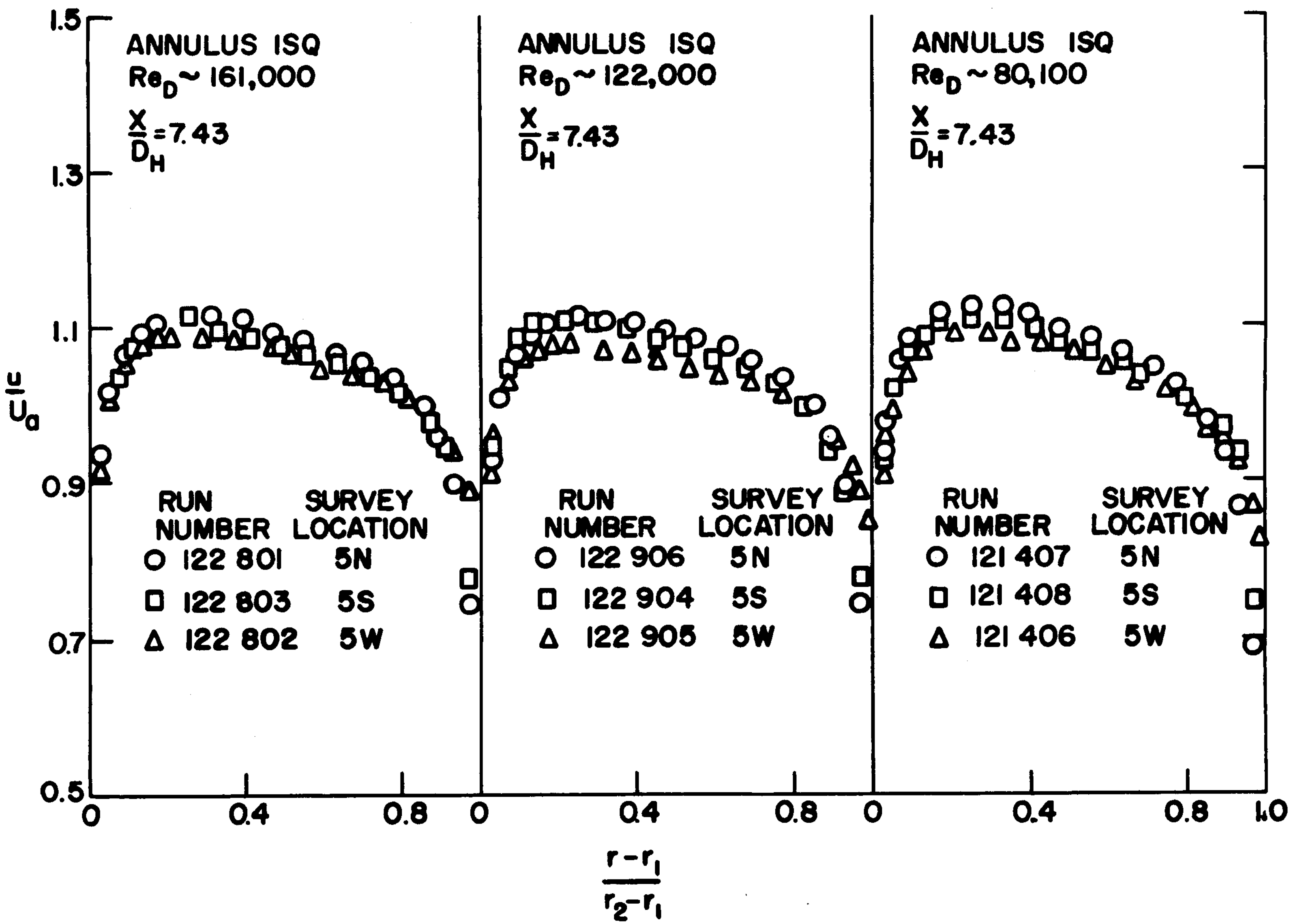

Figure 11. Circumferential-sequence velocity profiles for axial location 5 of annulus 1 SQ.

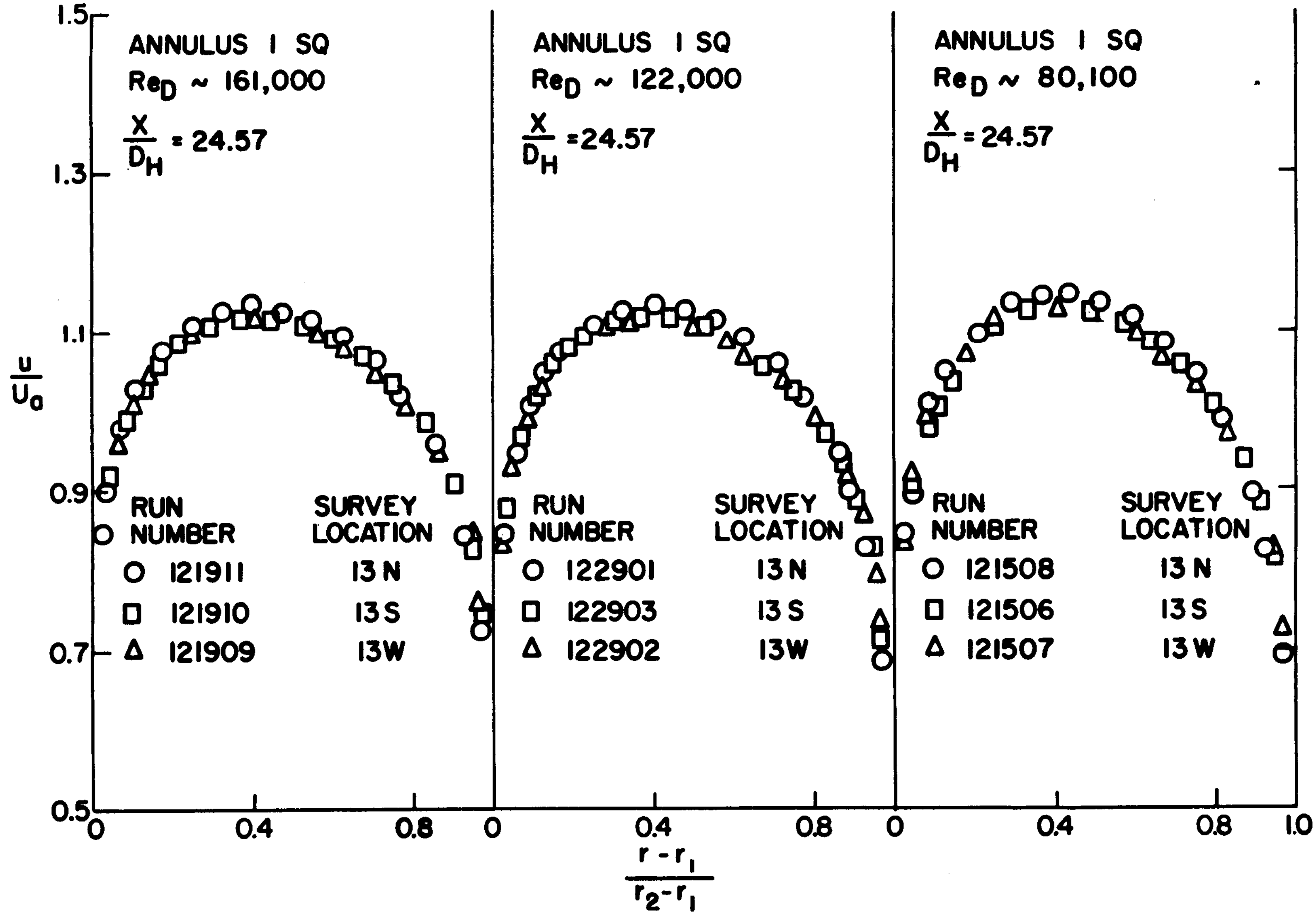

Figure 12. Circumferential-sequence velocity profiles for axial location 13 of annulus 1 SQ.

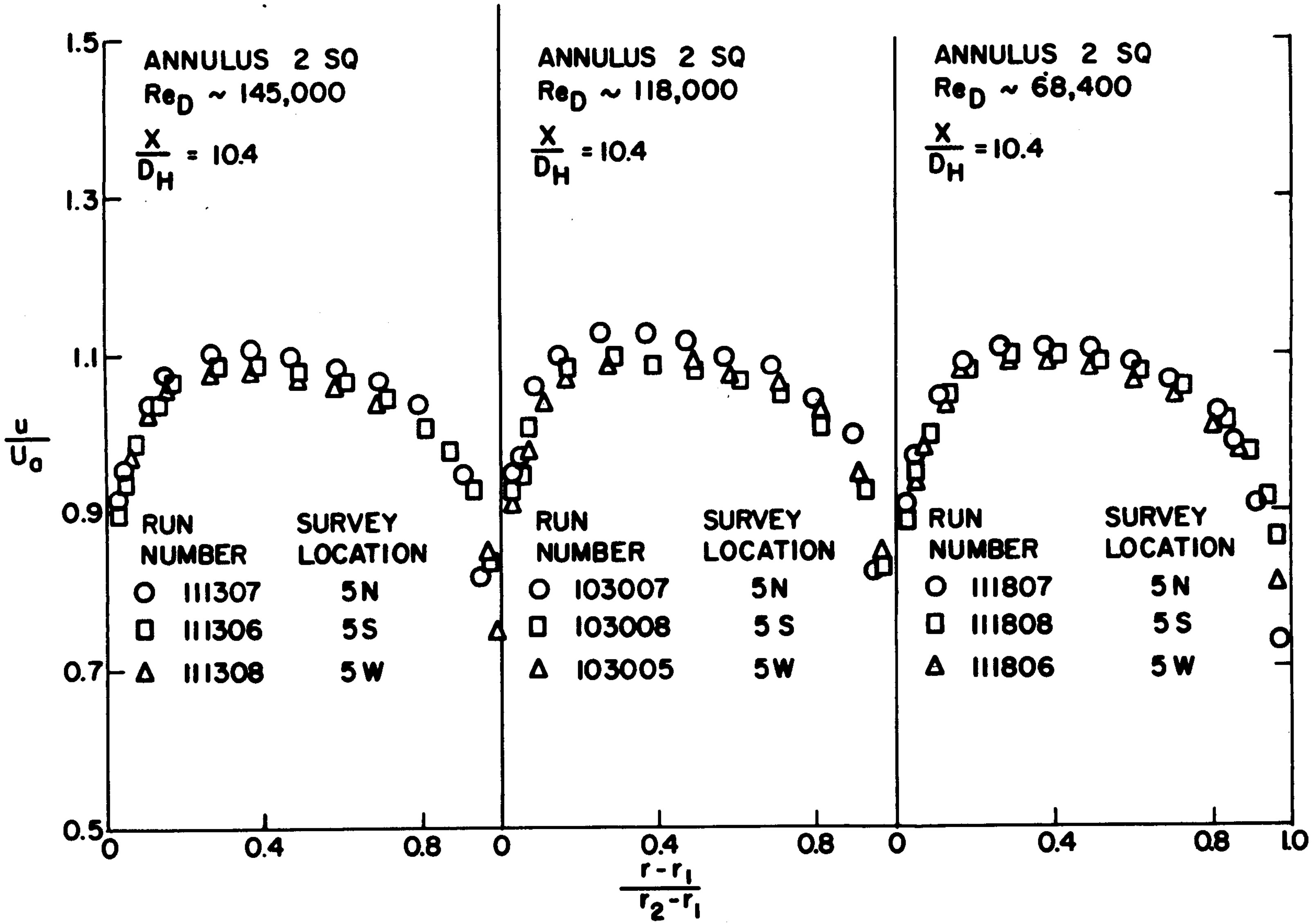

Figure 13. Circumferential-sequence velocity profiles for axial location 5 of annulus 2 SQ.

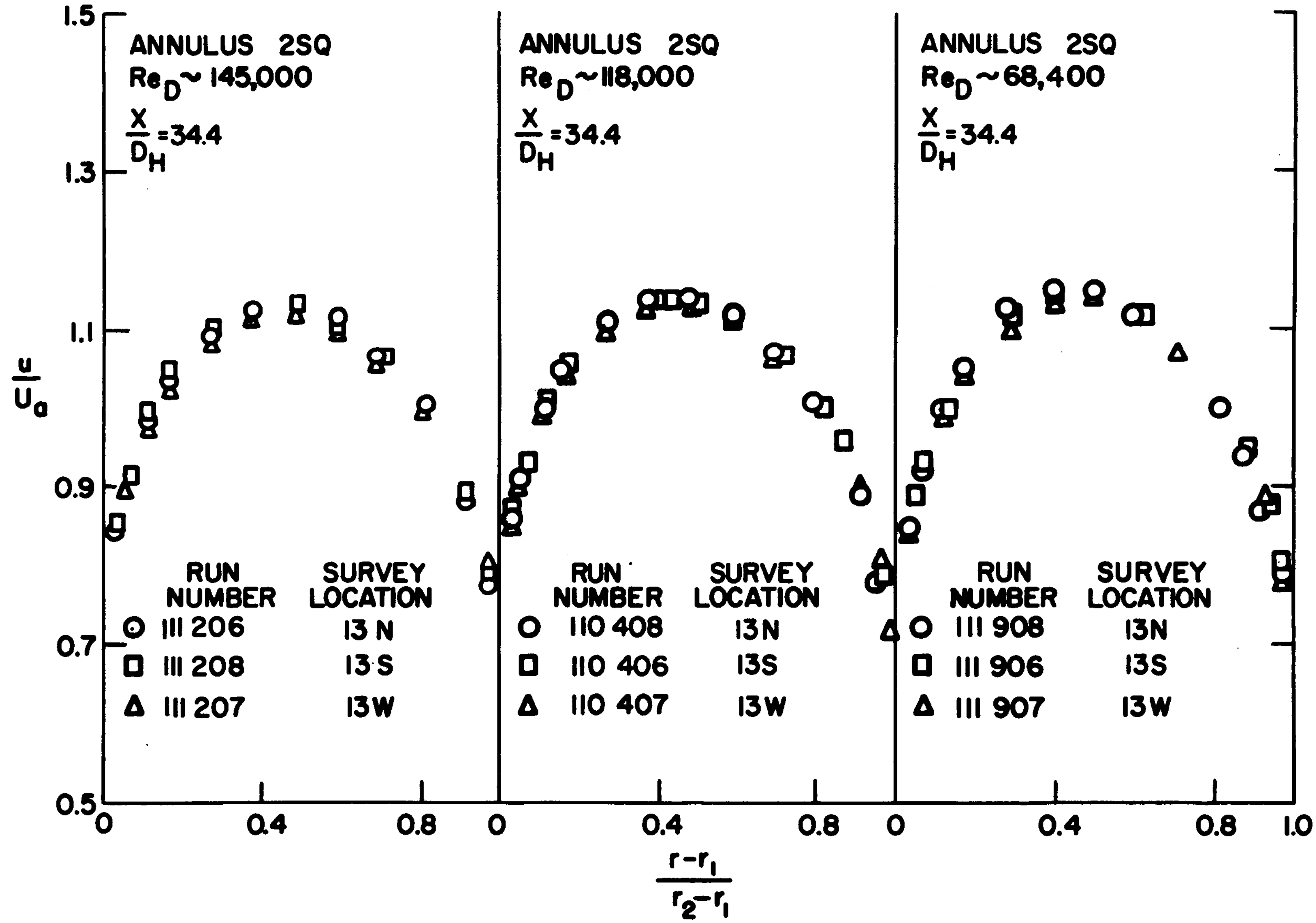

Figure 14. Circumferential-sequence velocity profiles for axial location 13 of annulus 2 SQ.

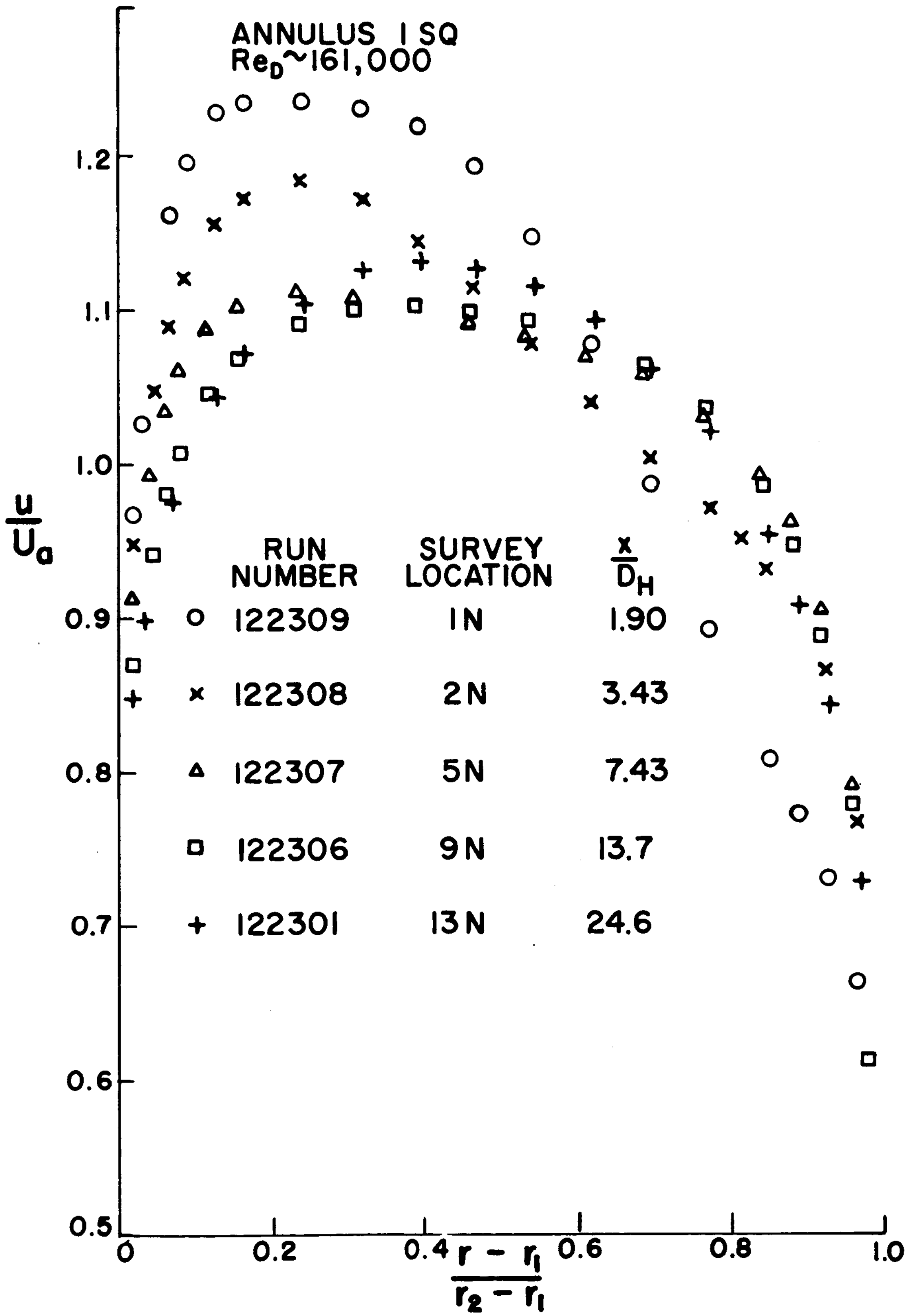

Figure 15. Axial-sequence velocity profiles for high flow rate and radial plane N of annulus 1 SQ.

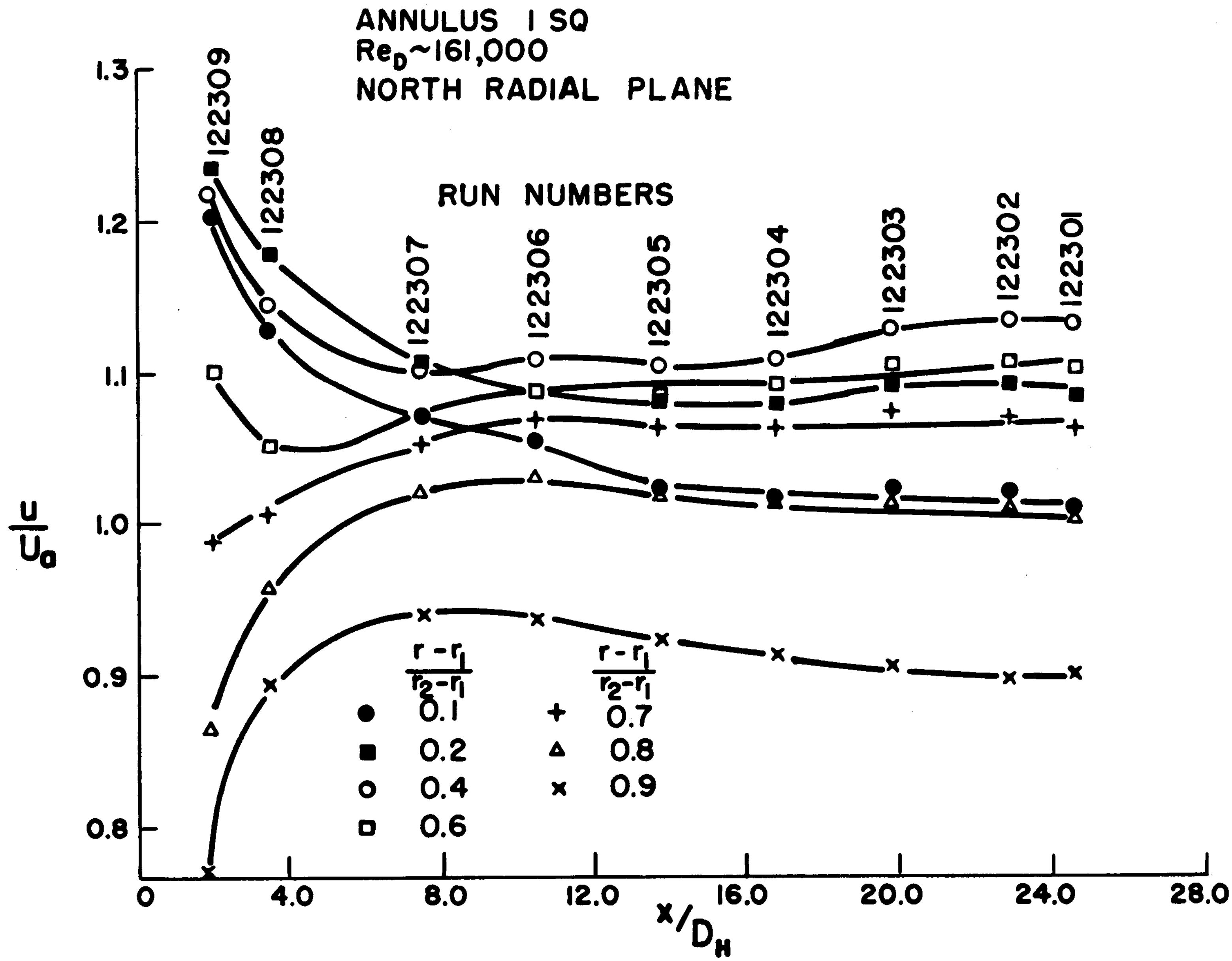

Figure 16. Variation of velocity ratio with x/D_H for high flow rate and radial plane N of annulus 1 SQ.

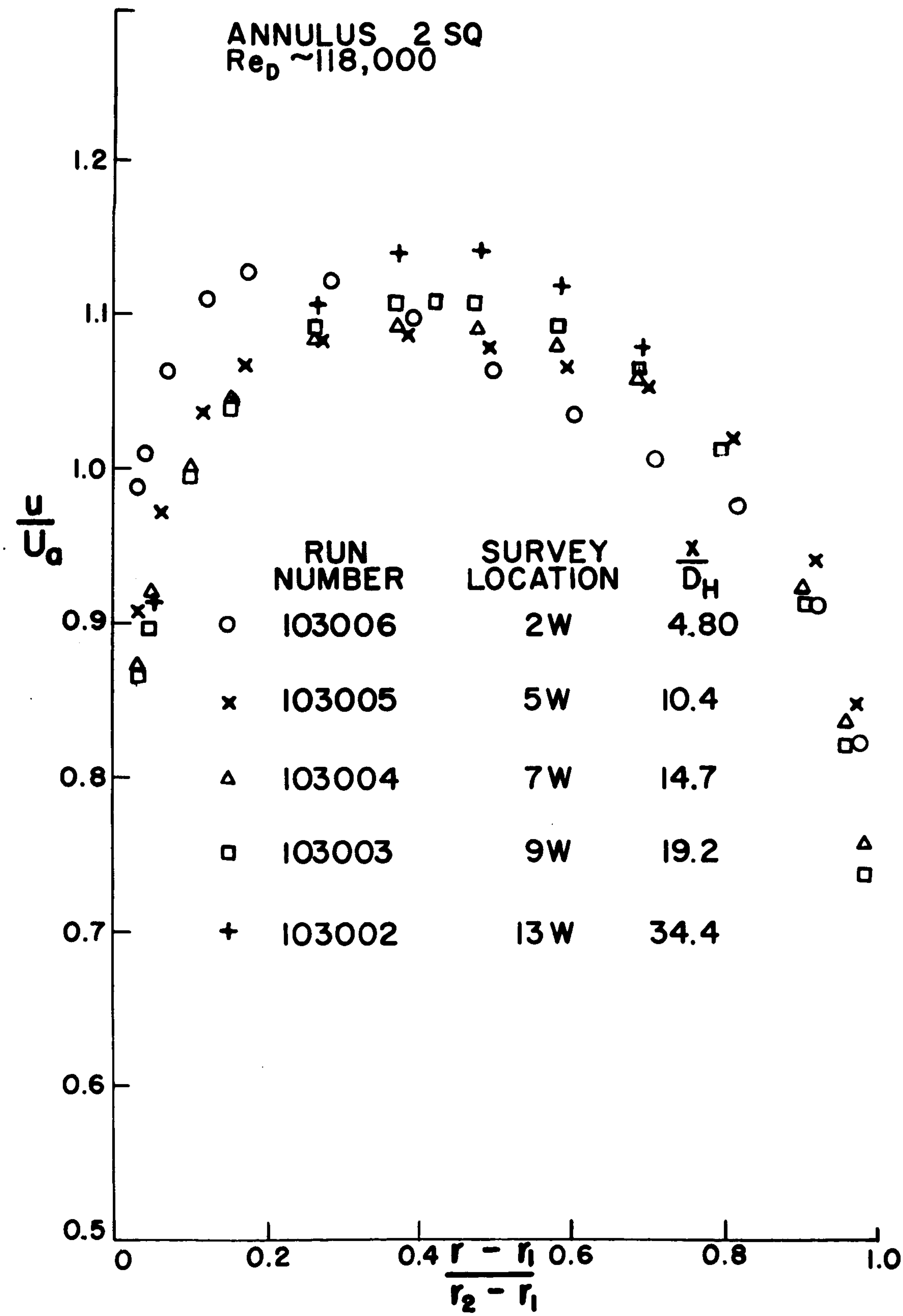

Figure 17. Axial-sequence velocity profiles for medium flow rate and radial plane W of annulus 2 SQ.

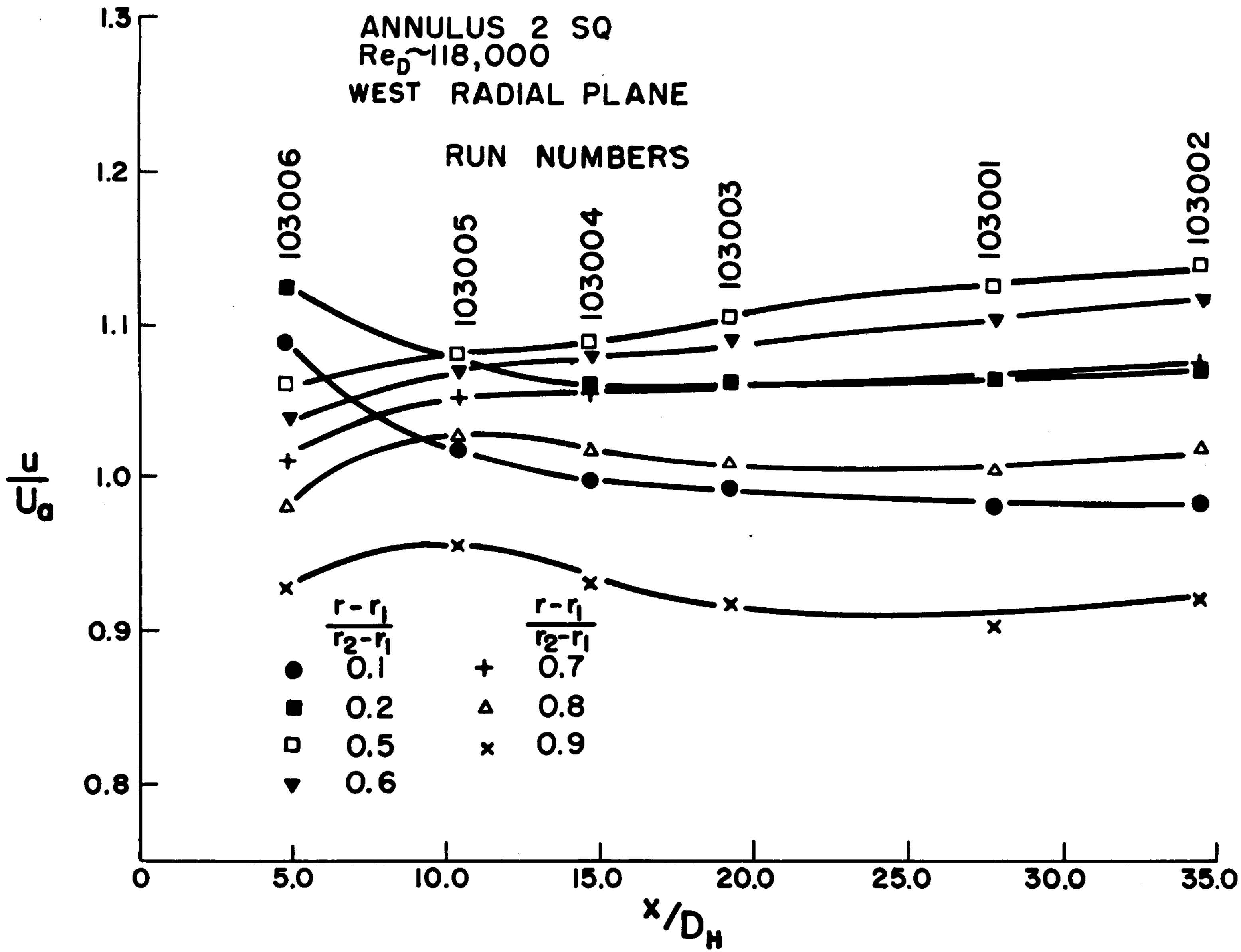

Figure 18. Variation of velocity ratio with x/D_H for high flow rate and radial plane W of annulus 2 SQ.

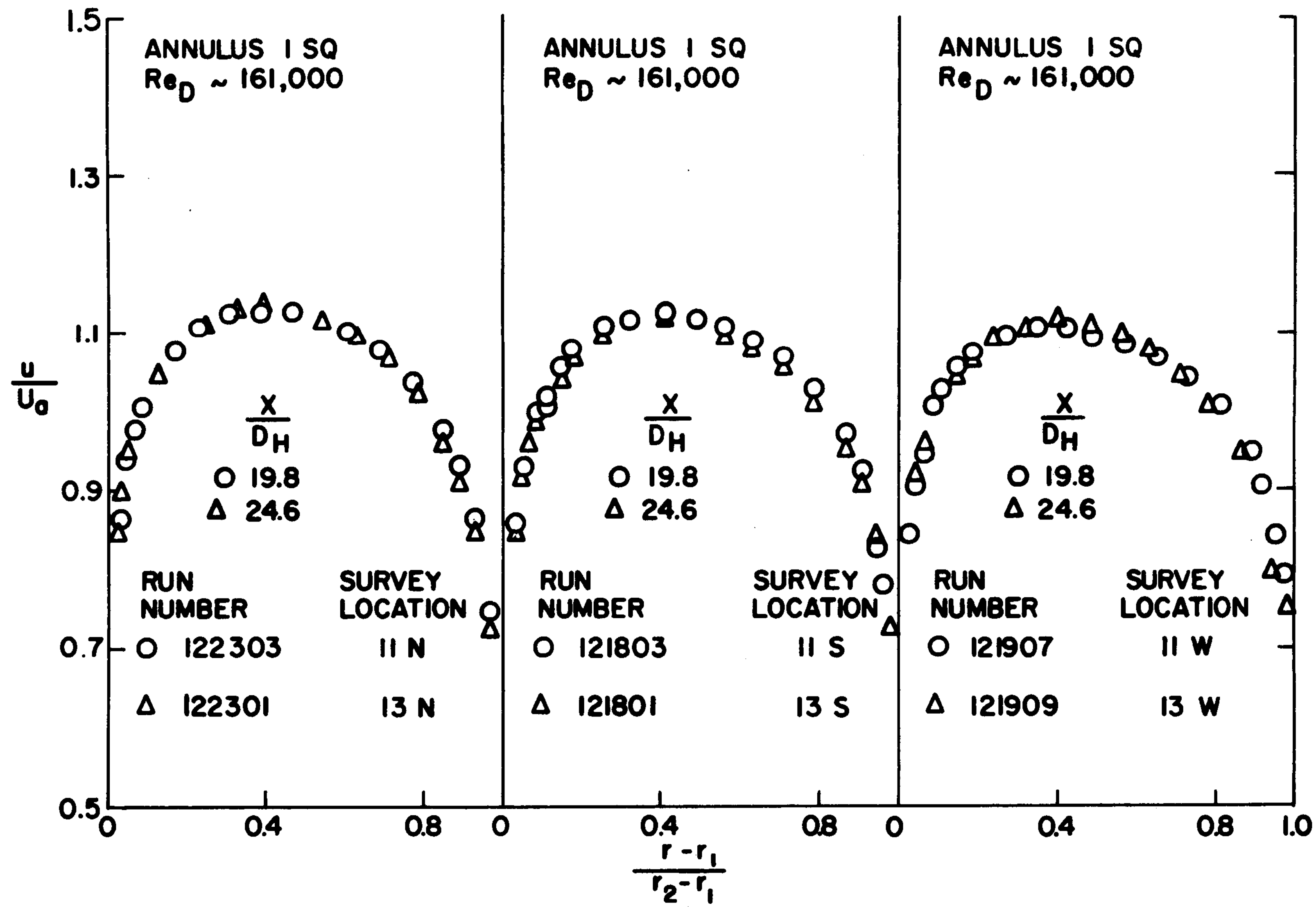

Figure 19. Axial-sequence velocity profiles for high flow rate and axial locations 11 and 13 of annulus 1 SQ.

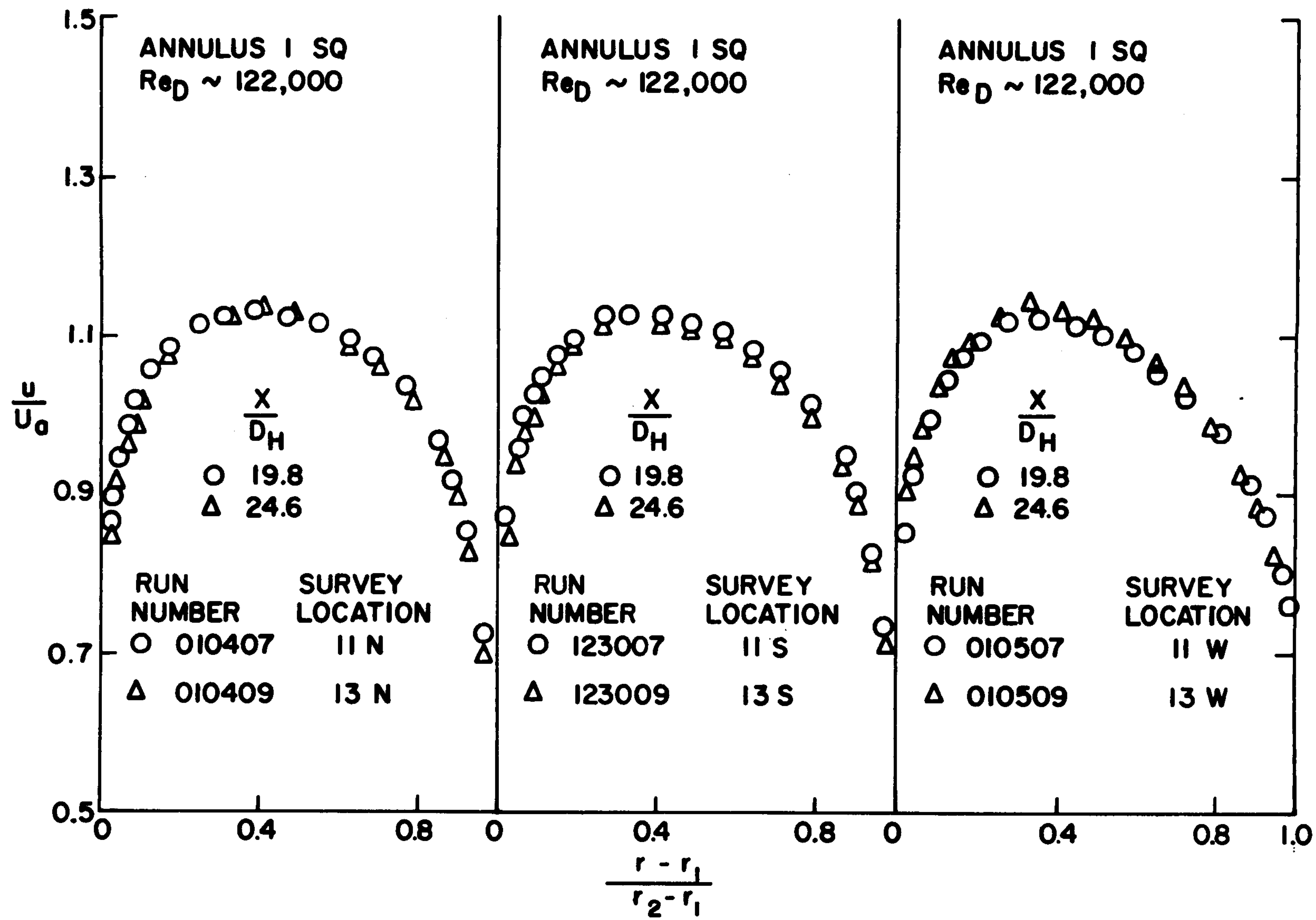

Figure 20. Axial-sequence velocity profiles for medium flow rate and axial locations 11 and 13 of annulus 1 SQ.

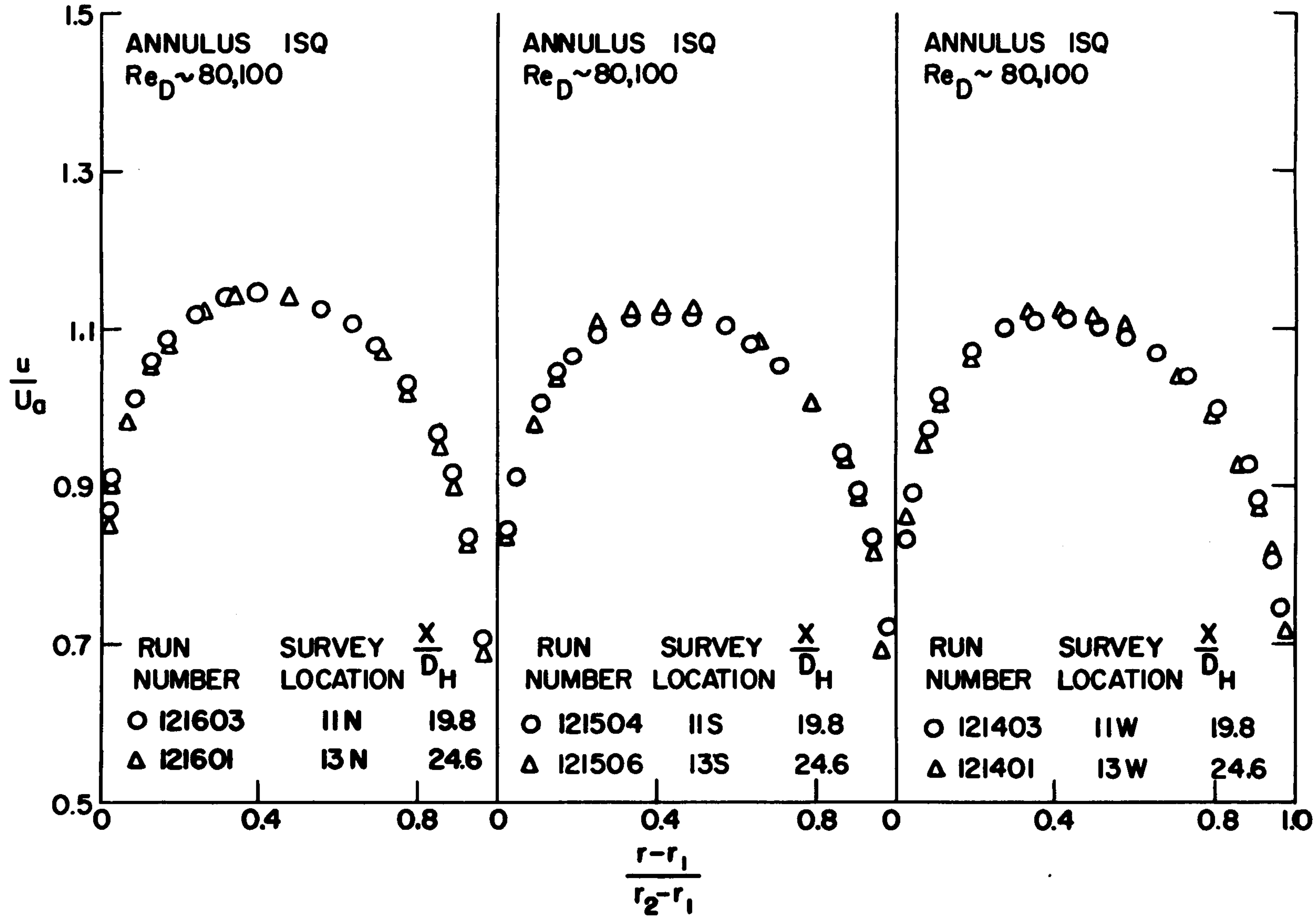

Figure 21. Axial-sequence velocity profiles for low flow rate and axial locations 11 and 13 of annulus 1 SQ.

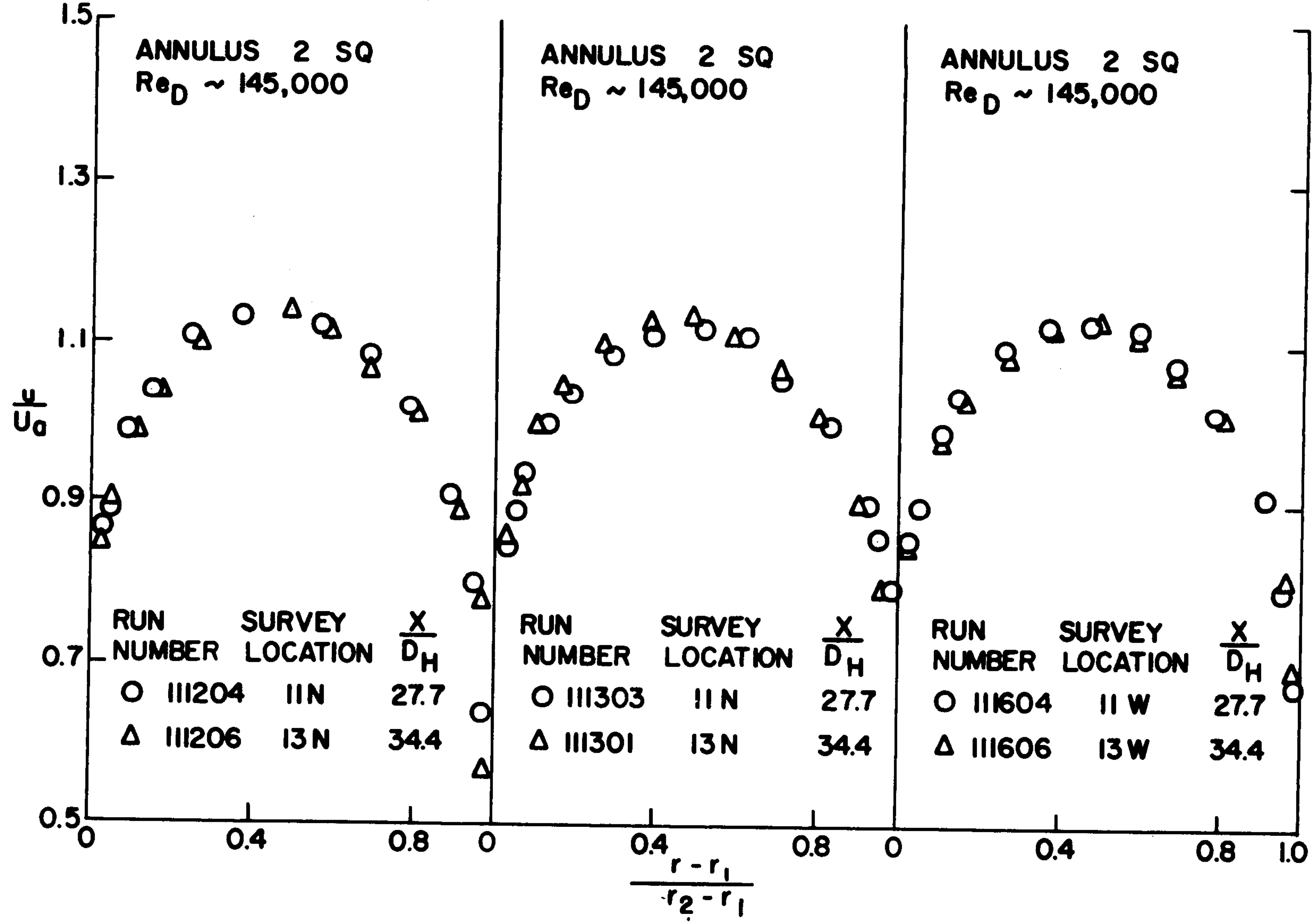

Figure 22. Axial-sequence velocity profiles for high flow rate and axial locations 11 and 13 of annulus 2 SQ.

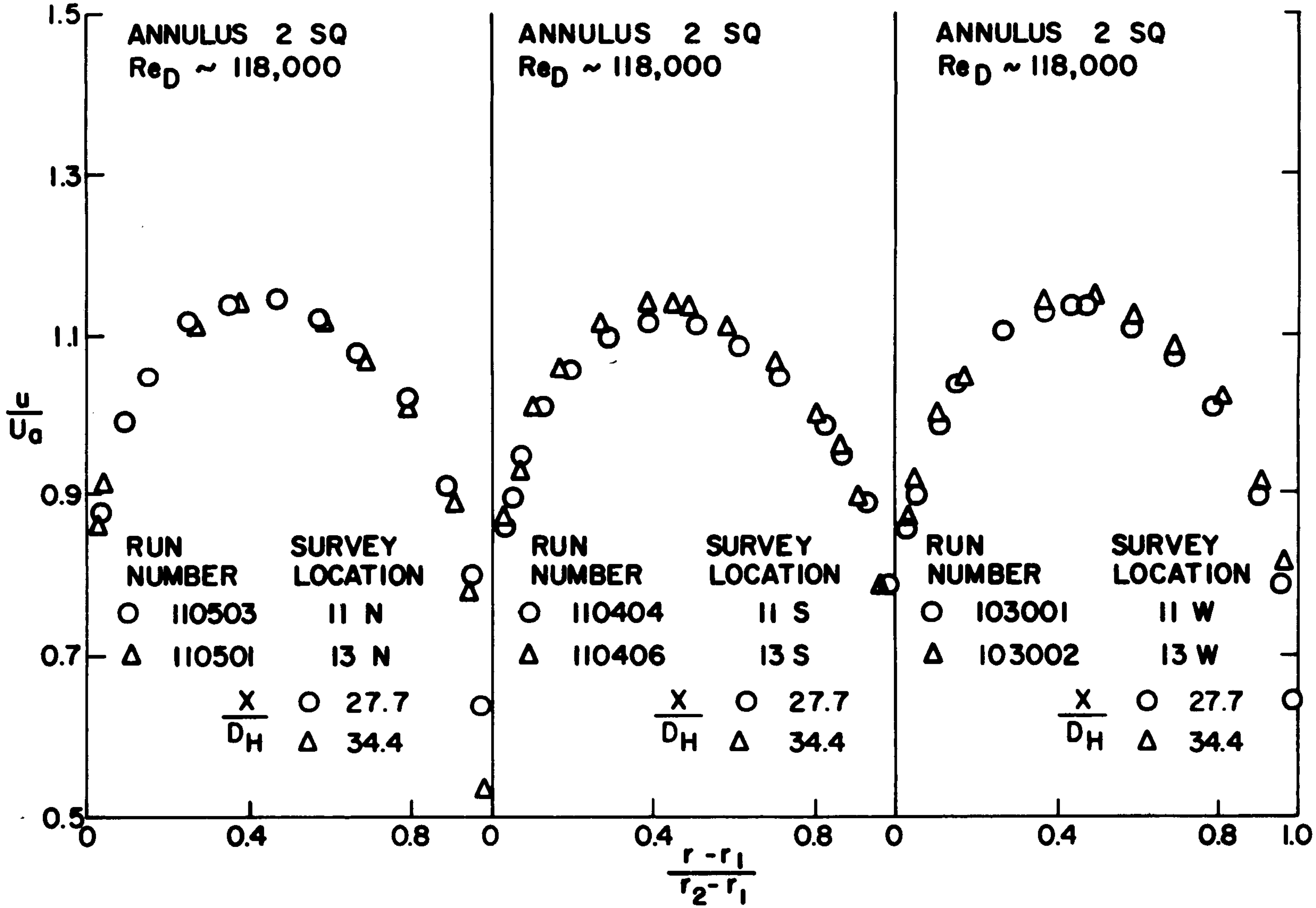

Figure 23. Axial-sequence velocity profiles for medium flow rate and axial locations 11 and 13 of annulus 2 SQ.

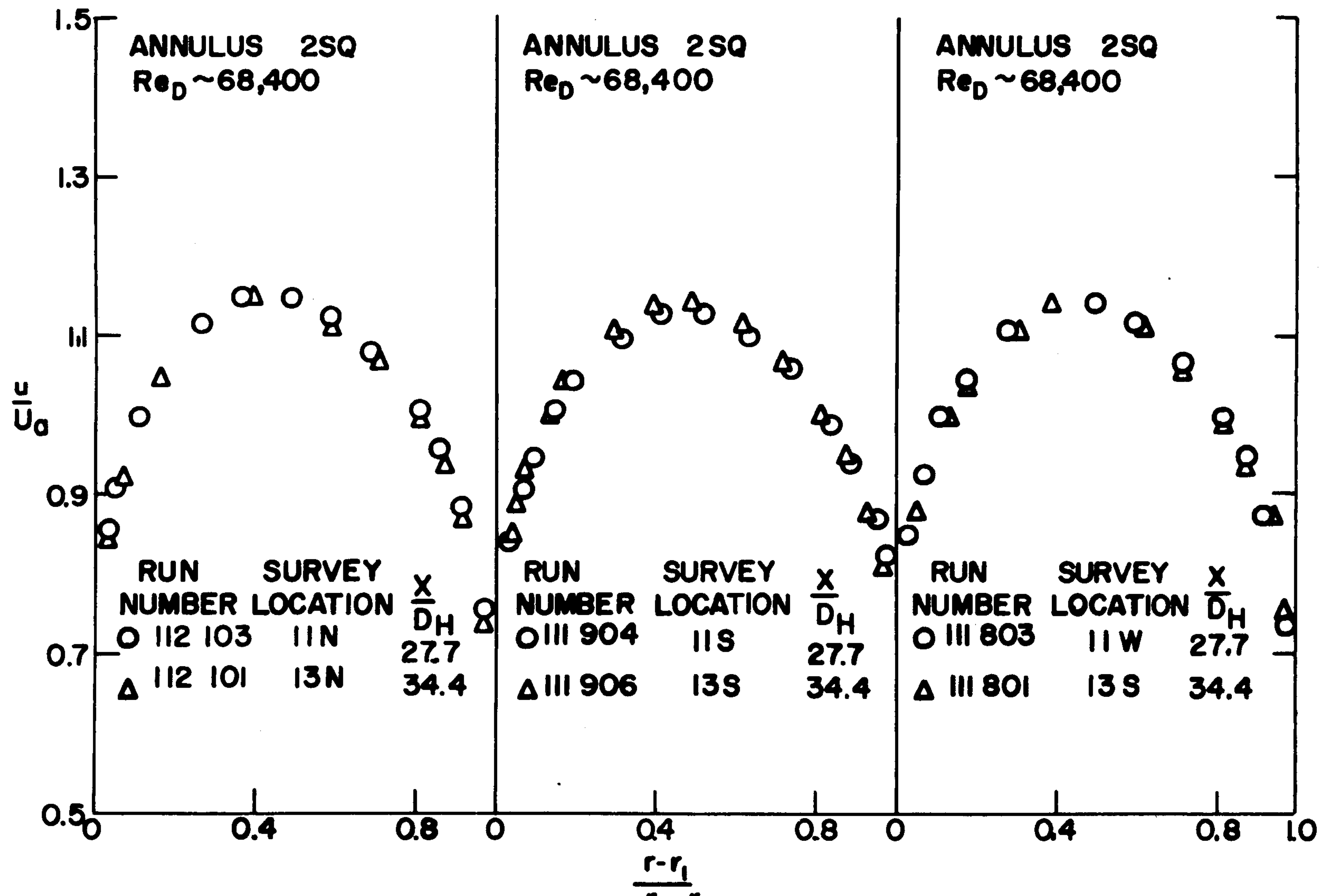

Figure 24. Axial-sequence velocity profiles for low flow rate and axial locations 11 and 13 of annulus 2 SQ.

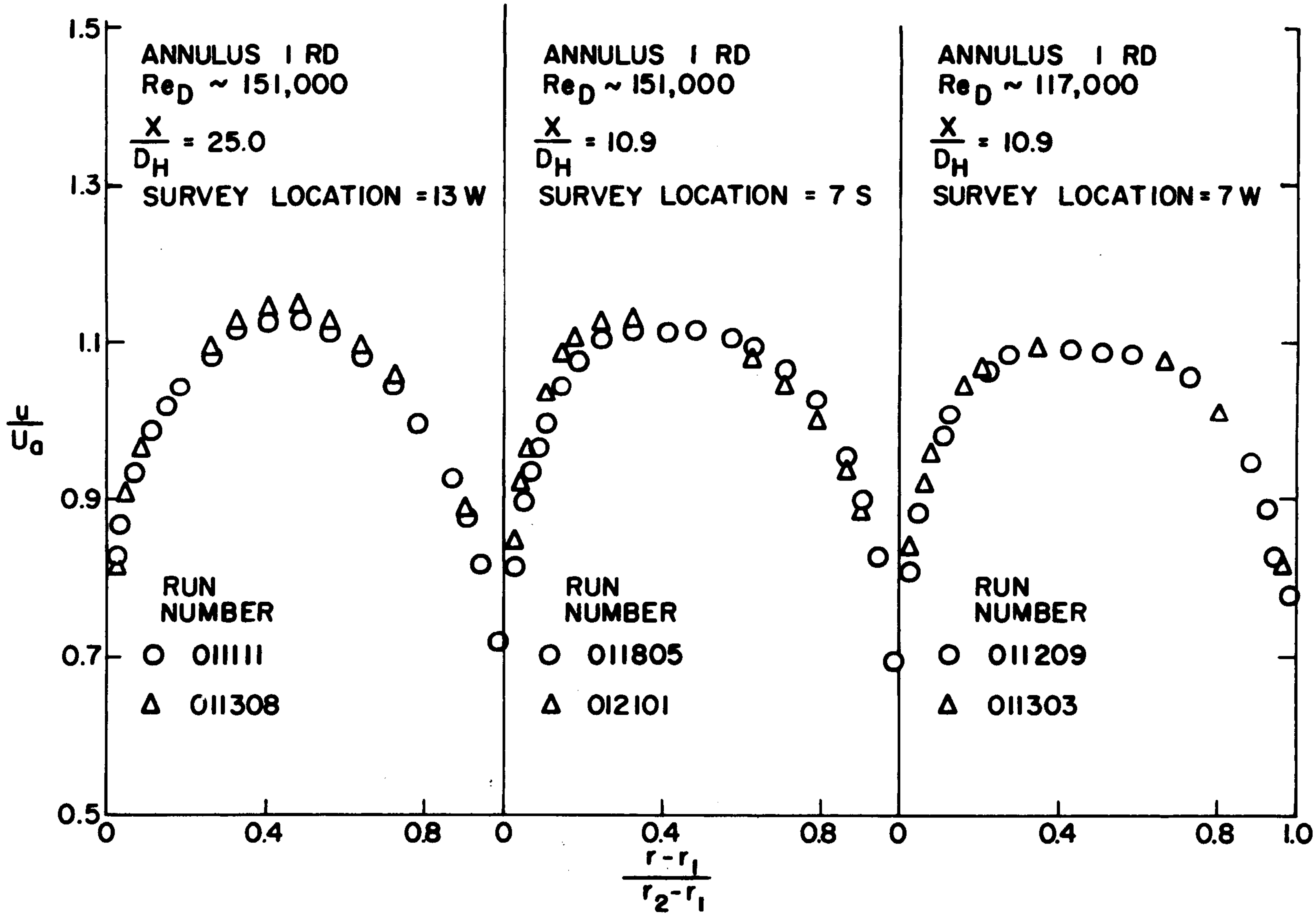

Figure 25. Typical time-sequence velocity profiles for annulus 1 RD.

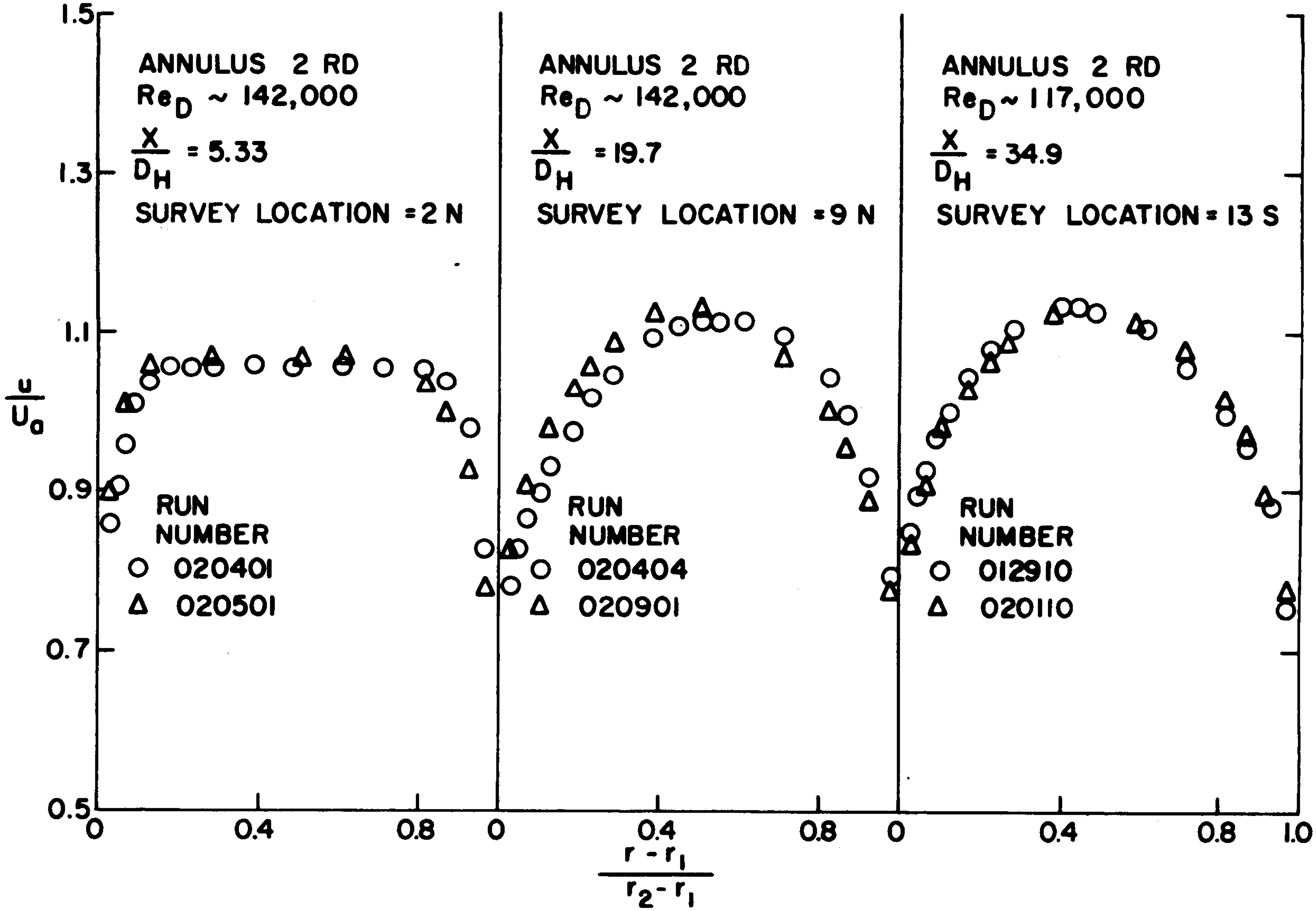

Figure 26. Typical time-sequence velocity profiles for annulus 2 RD.

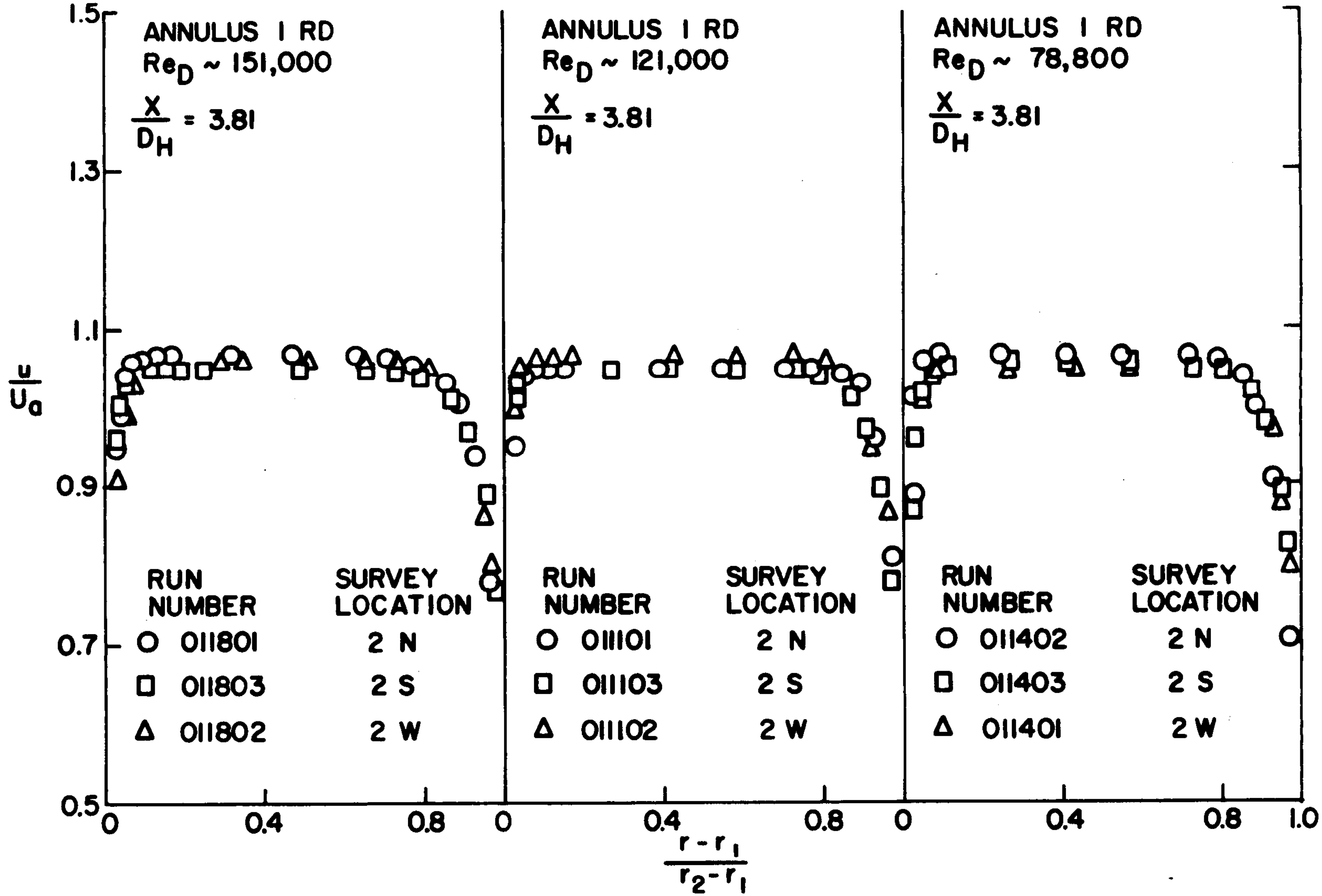

Figure 27. Circumferential-sequence velocity profiles for axial location 2 of annulus 1 RD.

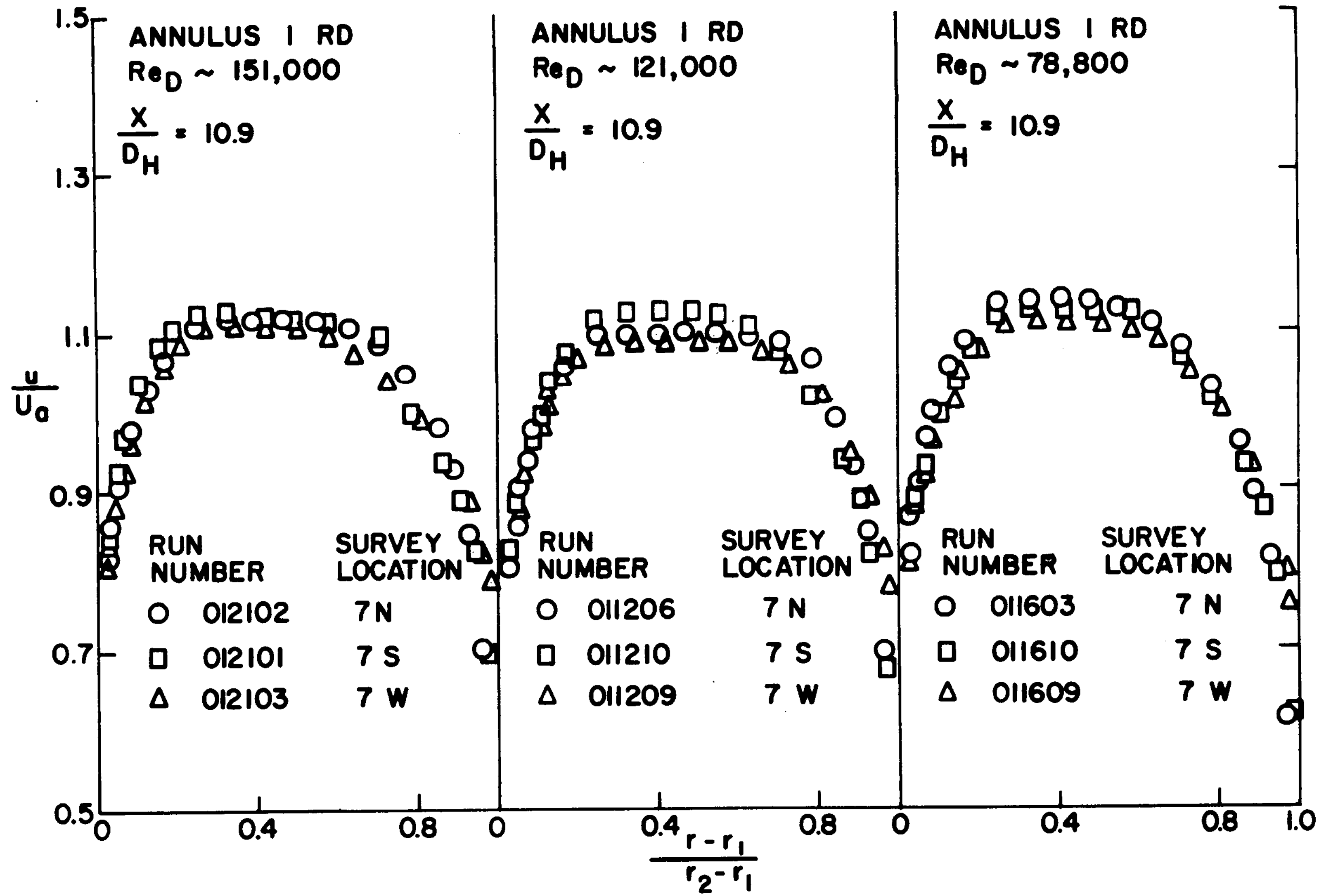

Figure 28. Circumferential-sequence velocity profiles for axial location 7 of annulus 1 RD.

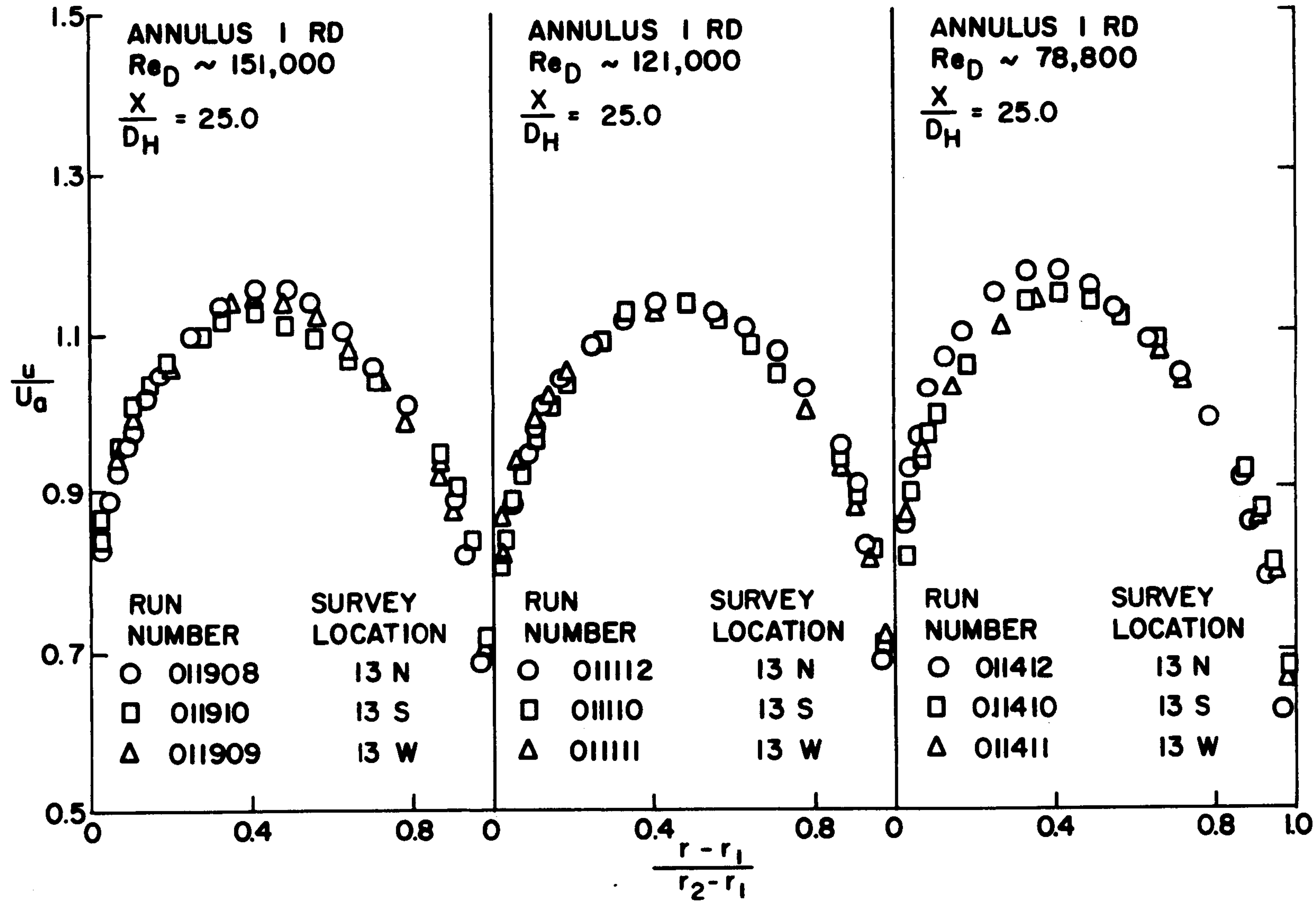

Figure 29. Circumferential-sequence velocity profiles for axial location 13 of annulus 1 RD.

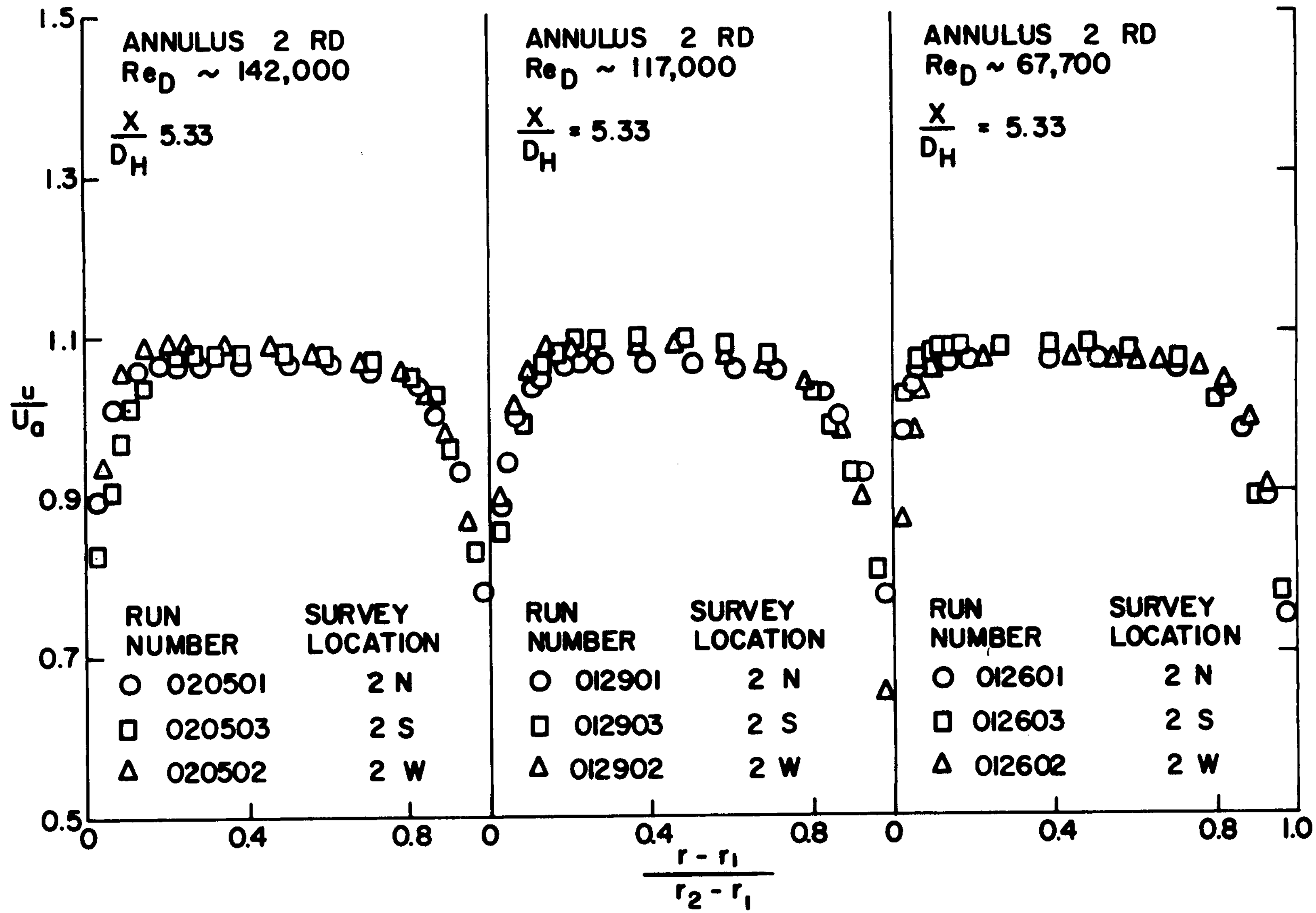

Figure 30. Circumferential-sequence velocity profiles for axial location 2 of annulus 2 RD.

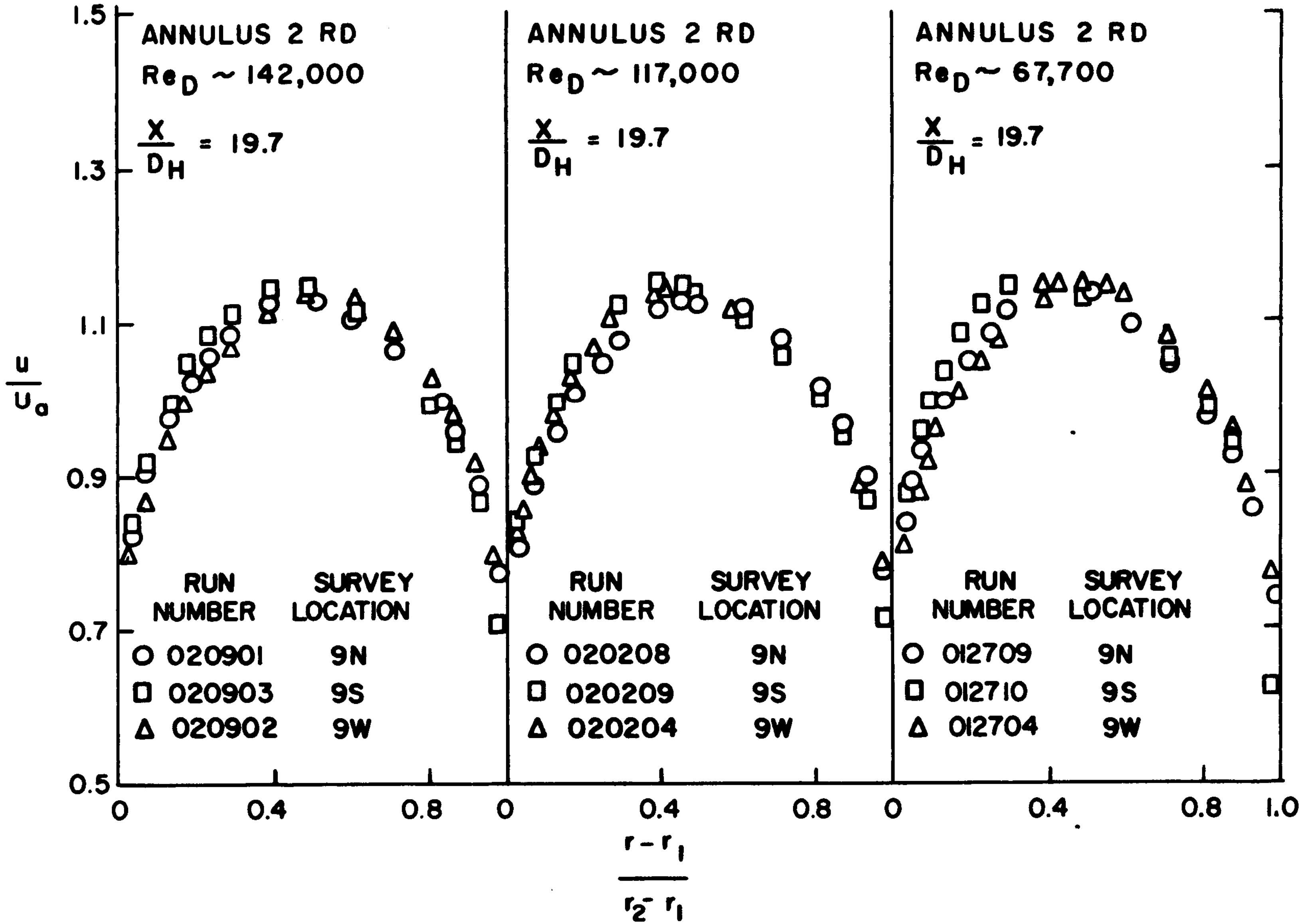

Figure 31. Circumferential-sequence velocity profiles for axial location 9 of annulus 2 RD.

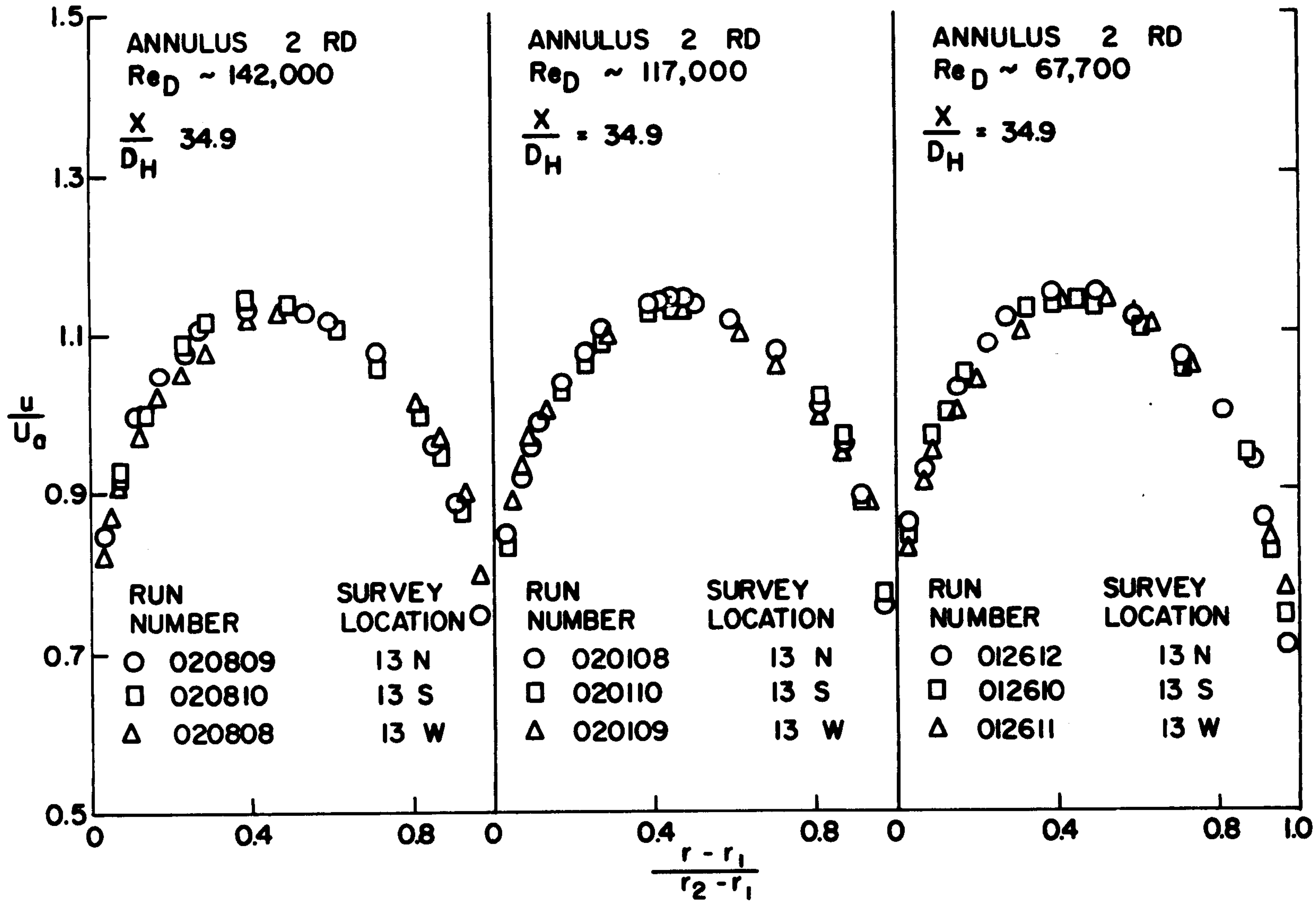

Figure 32. Circumferential-sequence velocity profiles for axial location 13 of annulus 2 RD.

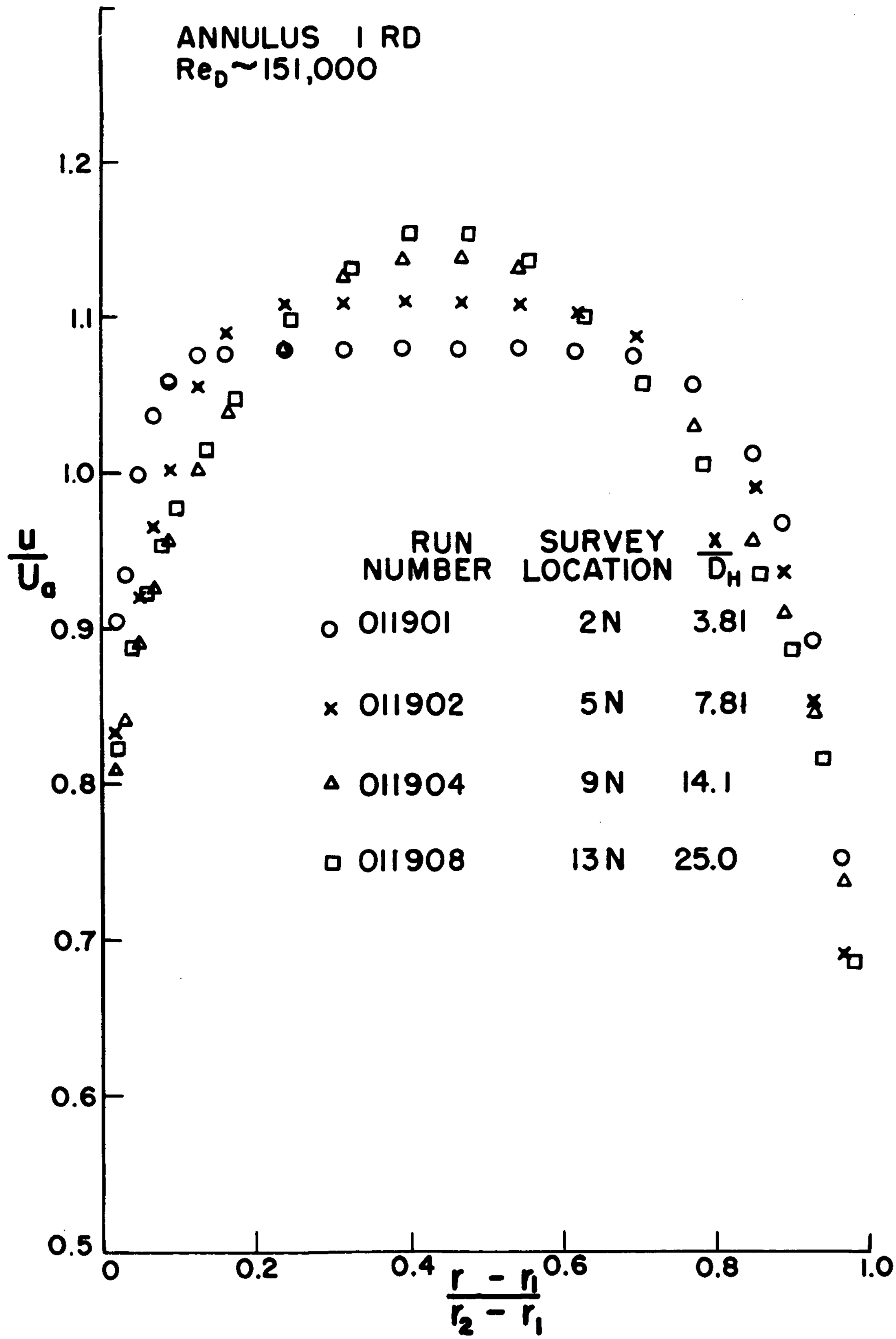

Figure 33. Axial-sequence velocity profiles for high flow rate and radial plane N of annulus 1 RD.

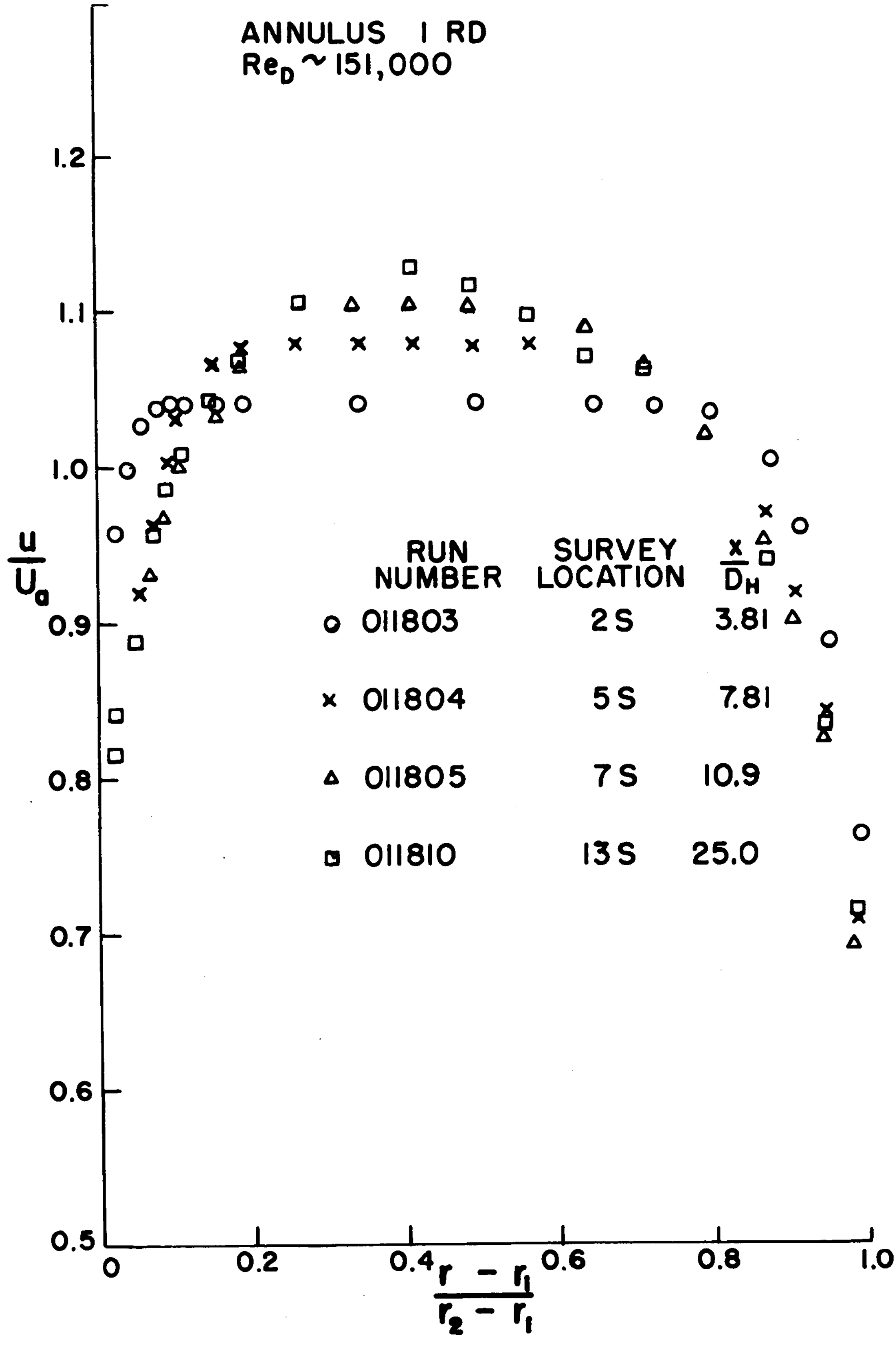

Figure 34. Axial-sequence velocity profiles for high flow rate and radial plane S of annulus 1 RD.

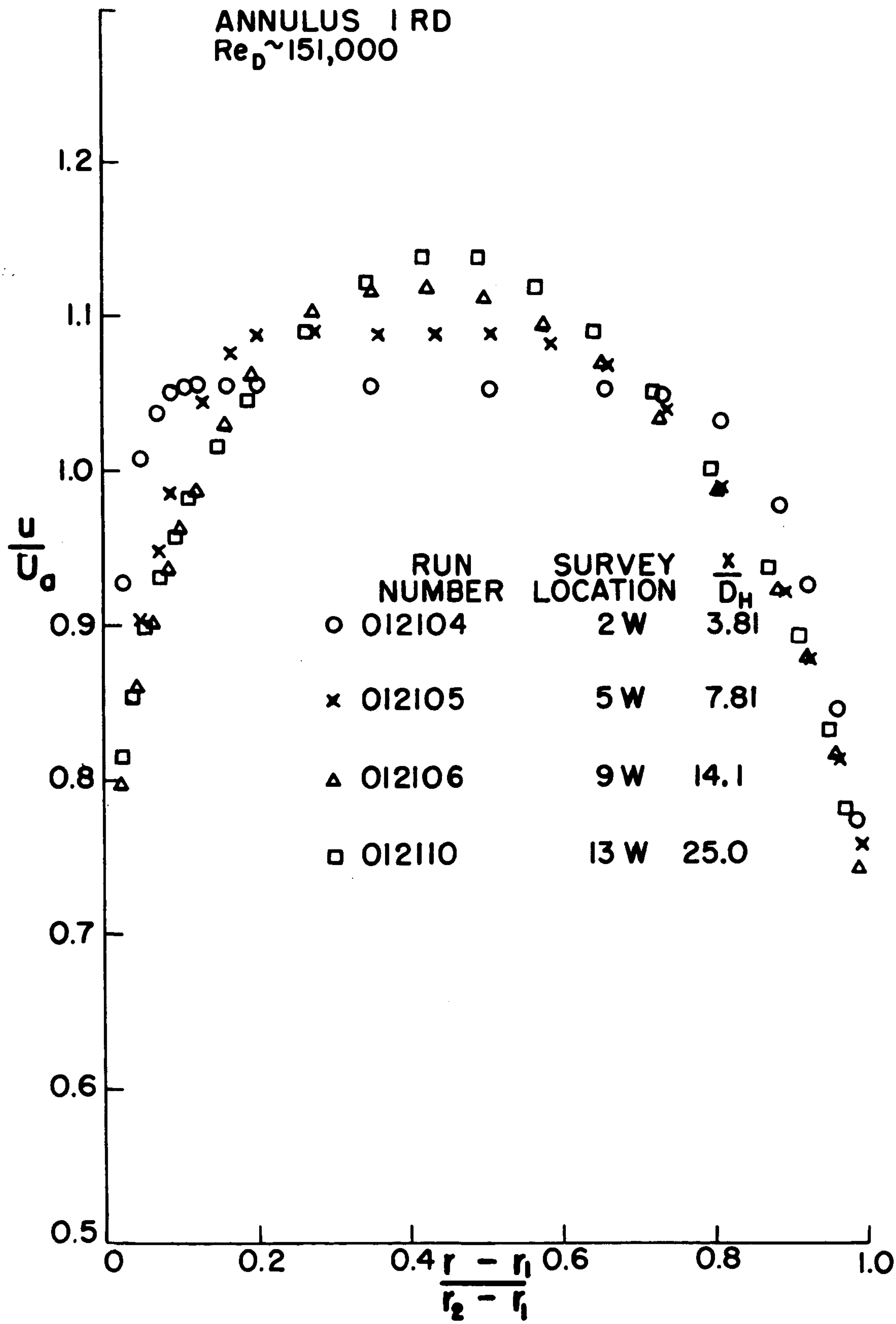

Figure 35. Axial-sequence velocity profiles for high flow rate and radial plane W of annulus 1 RD.

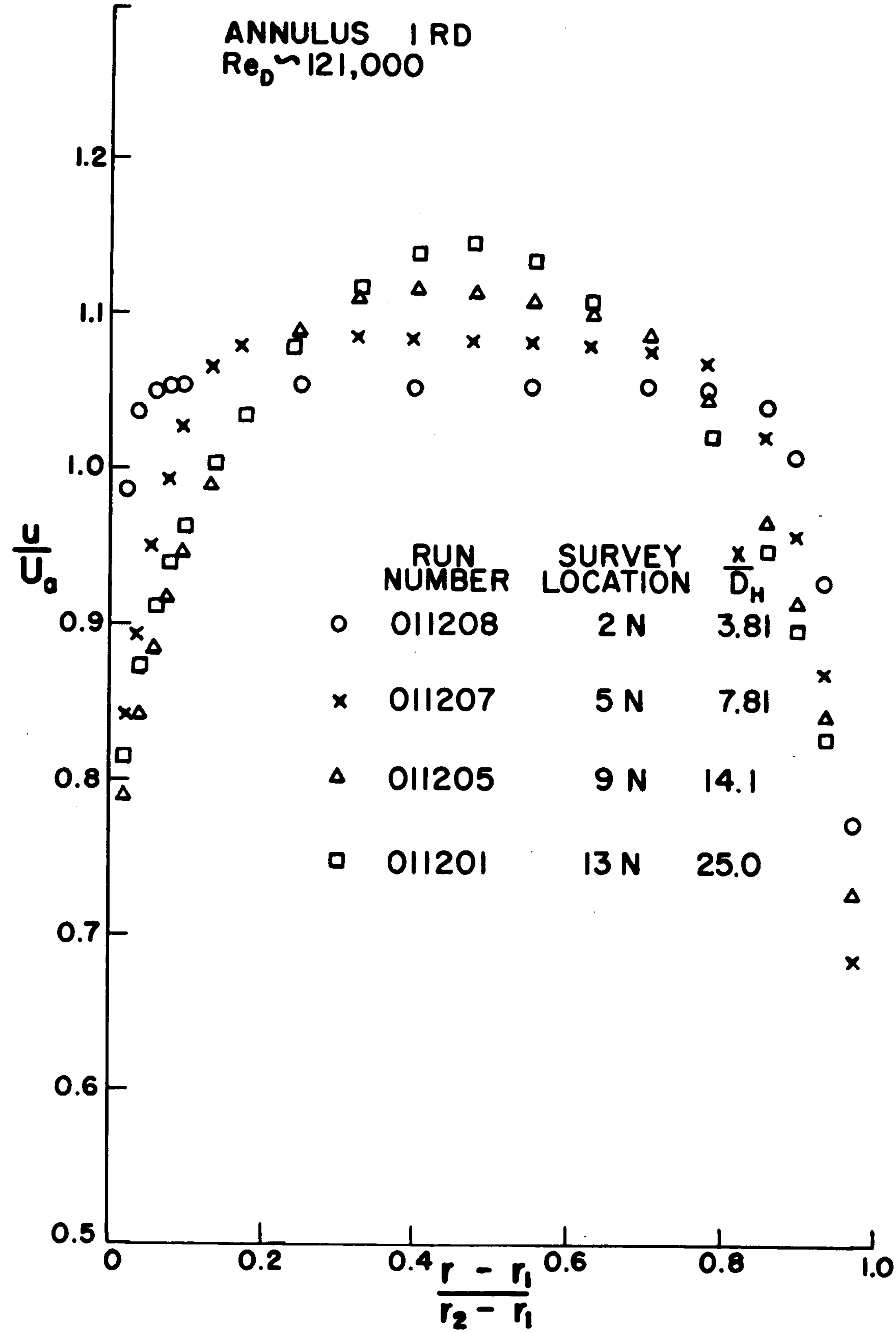

Figure 36. Axial-sequence velocity profiles for medium flow rate and radial plane N of annulus 1 RD.

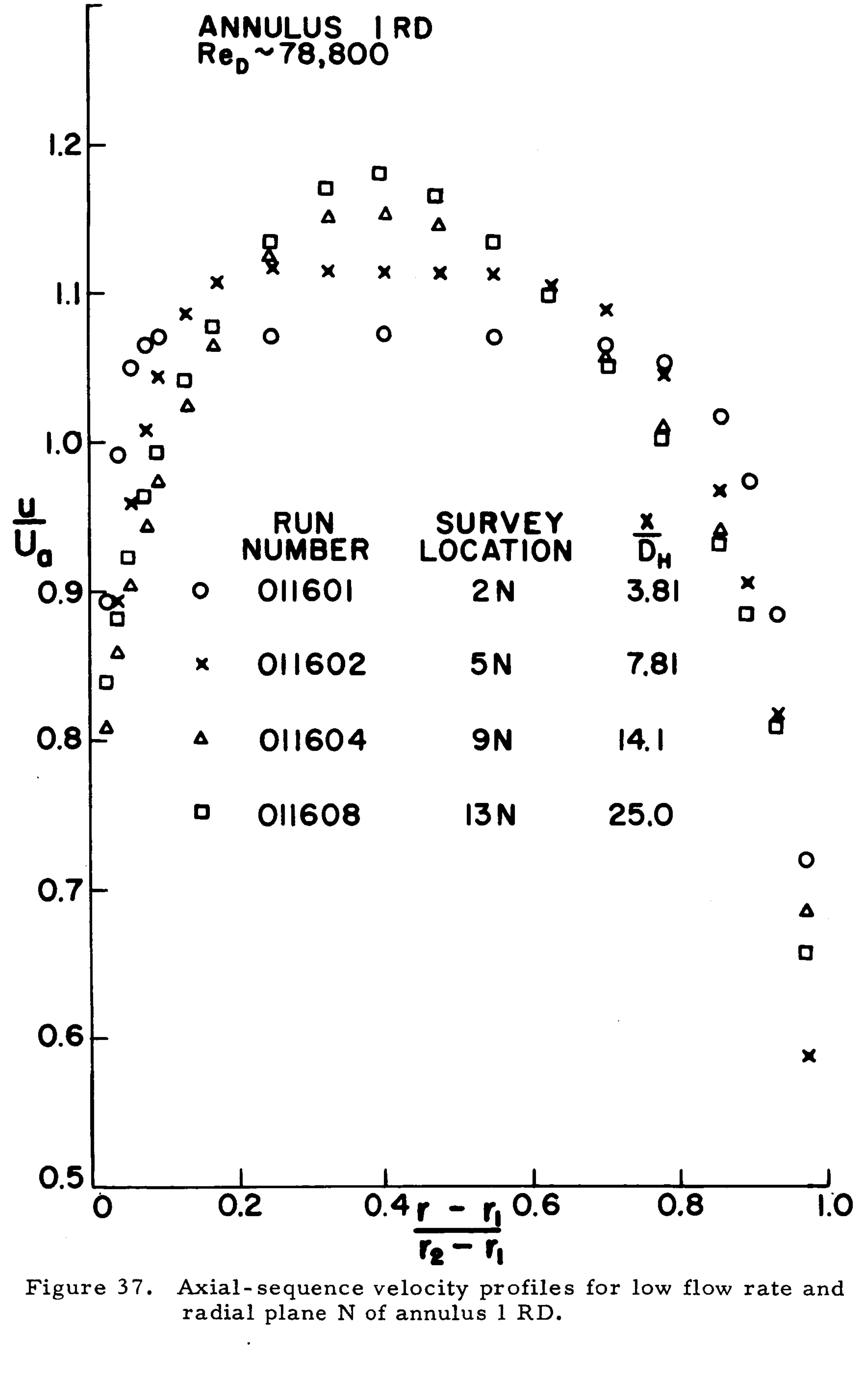

Figure 37. Axial-sequence velocity profiles for low flow rate and radial plane N of annulus 1 RD.

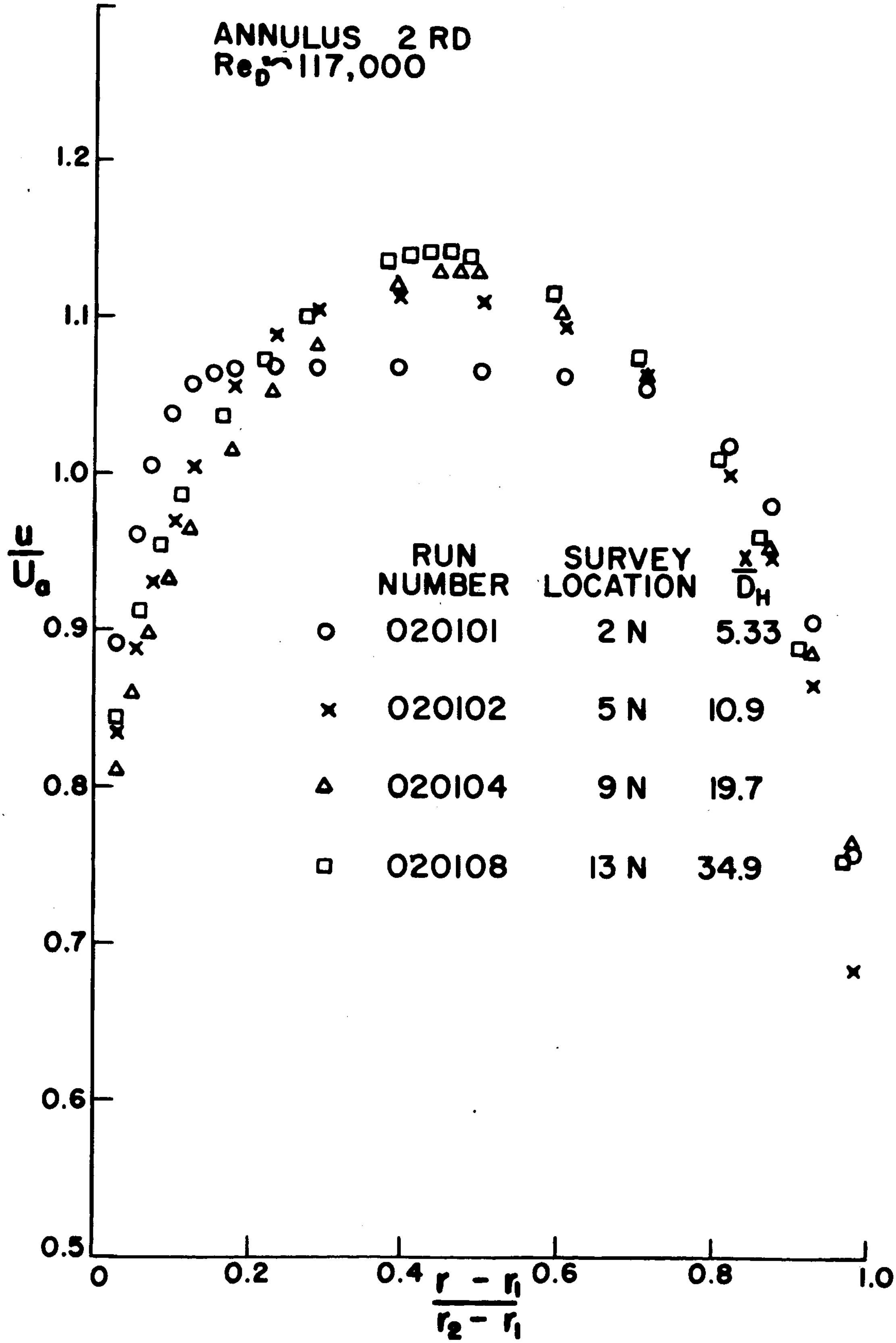

Figure 38. Axial-sequence velocity profiles for medium flow rate and radial plane N of annulus 2 RD.

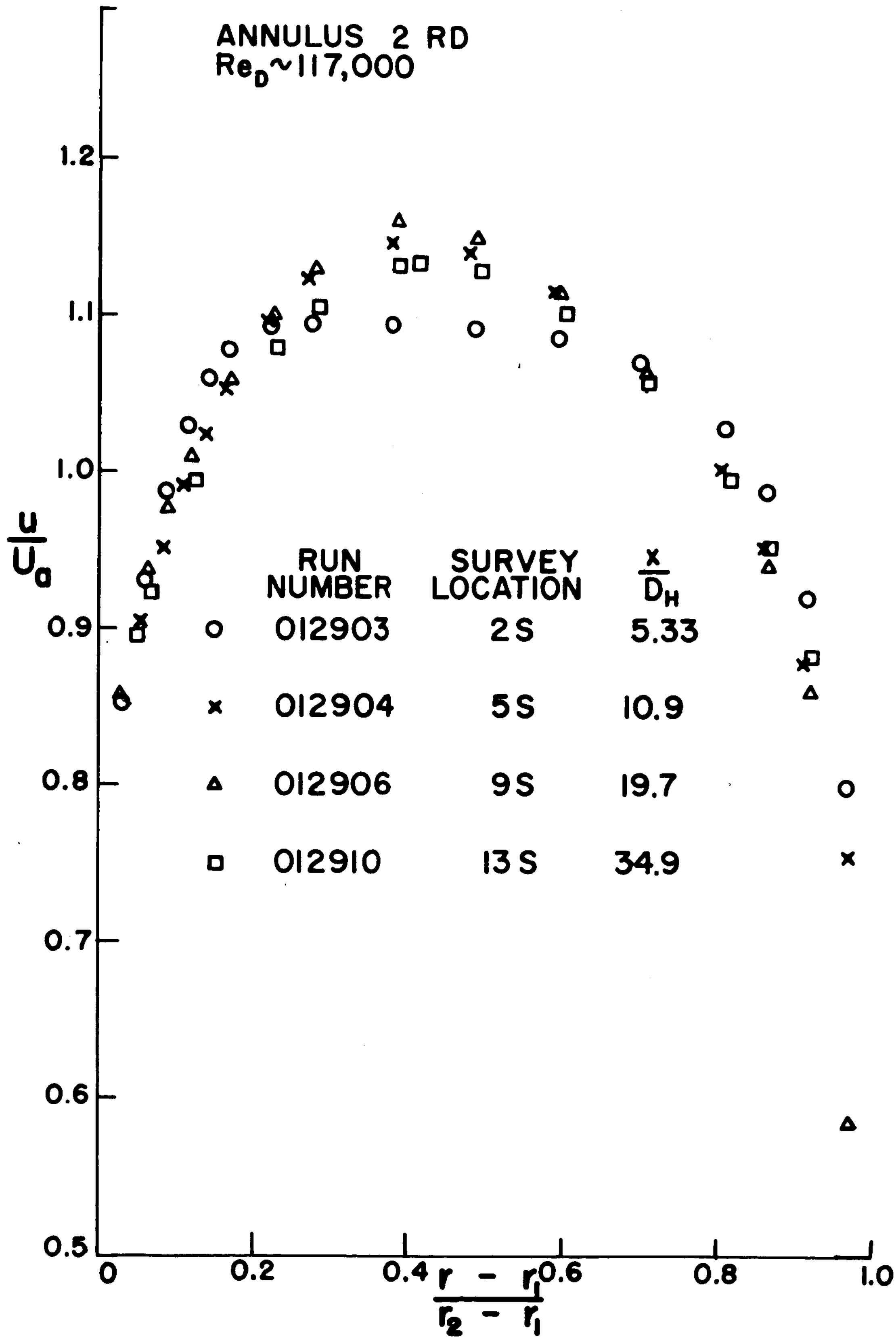

Figure 39. Axial-sequence velocity profiles for medium flow rate and radial plane S of annulus 2 RD.

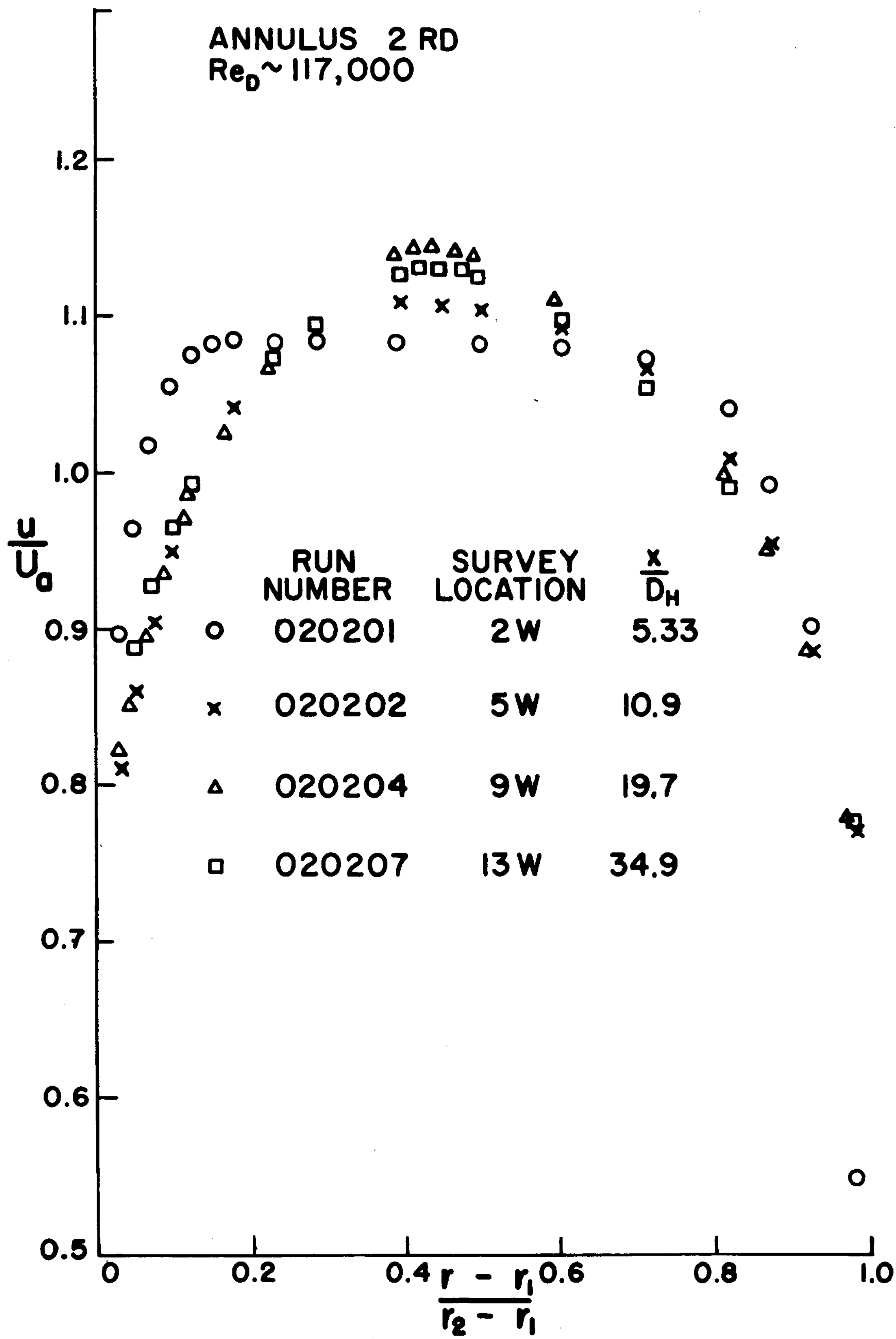

Figure 40. Axial-sequence velocity profiles for medium flow rate and radial plane W of annulus 2 RD.

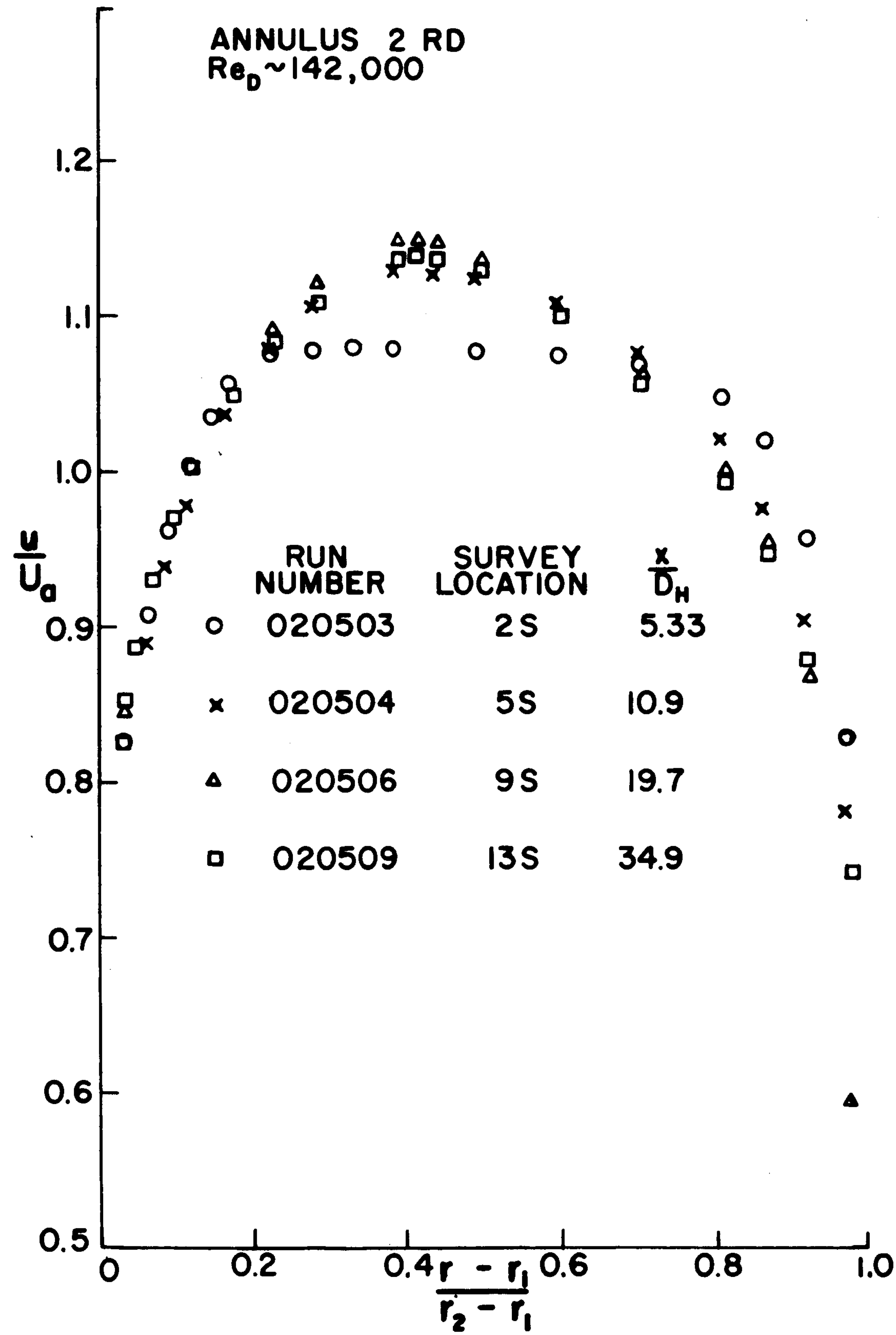

Figure 41. Axial-sequence velocity profiles for high flow rate and radial plane S of annulus 2 RD.

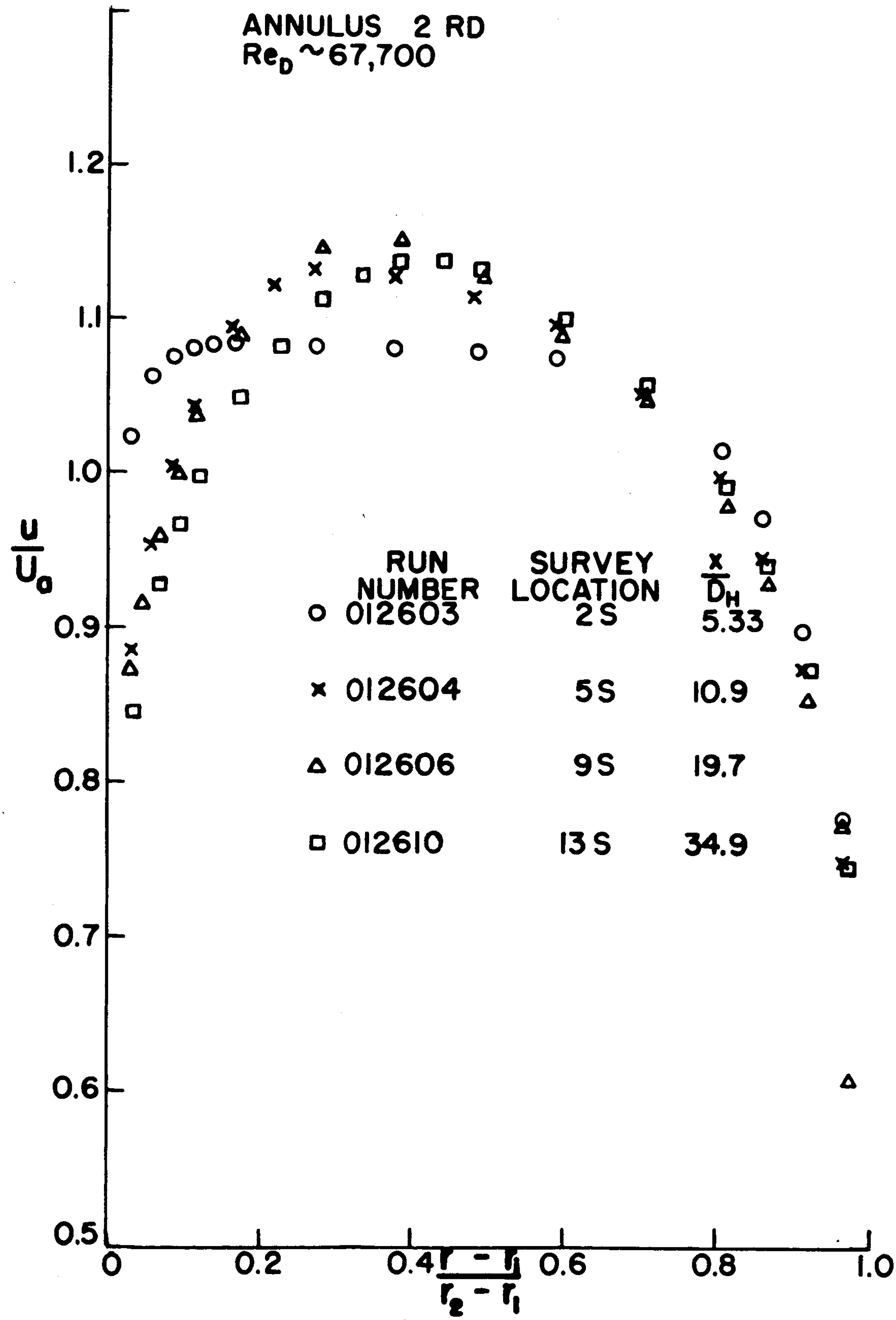

Figure 42. Axial-sequence velocity profiles for low flow rate and radial plane S of annulus 2 RD.

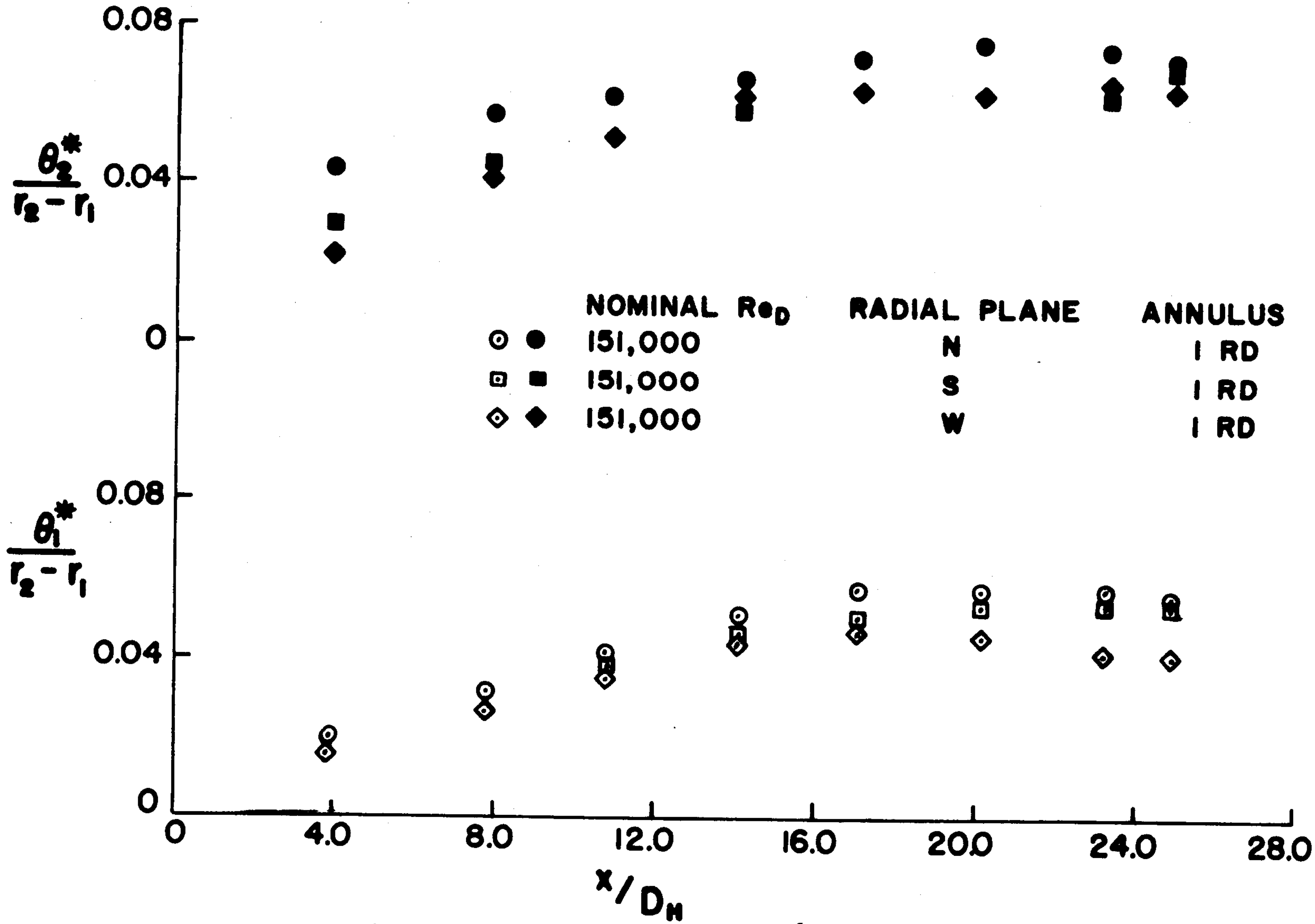

Figure 43. Variation of exact inner-and outer-wall boundary-layer-displacement-thickness parameters with x/D_H in annulus 1 RD for high flow rate.

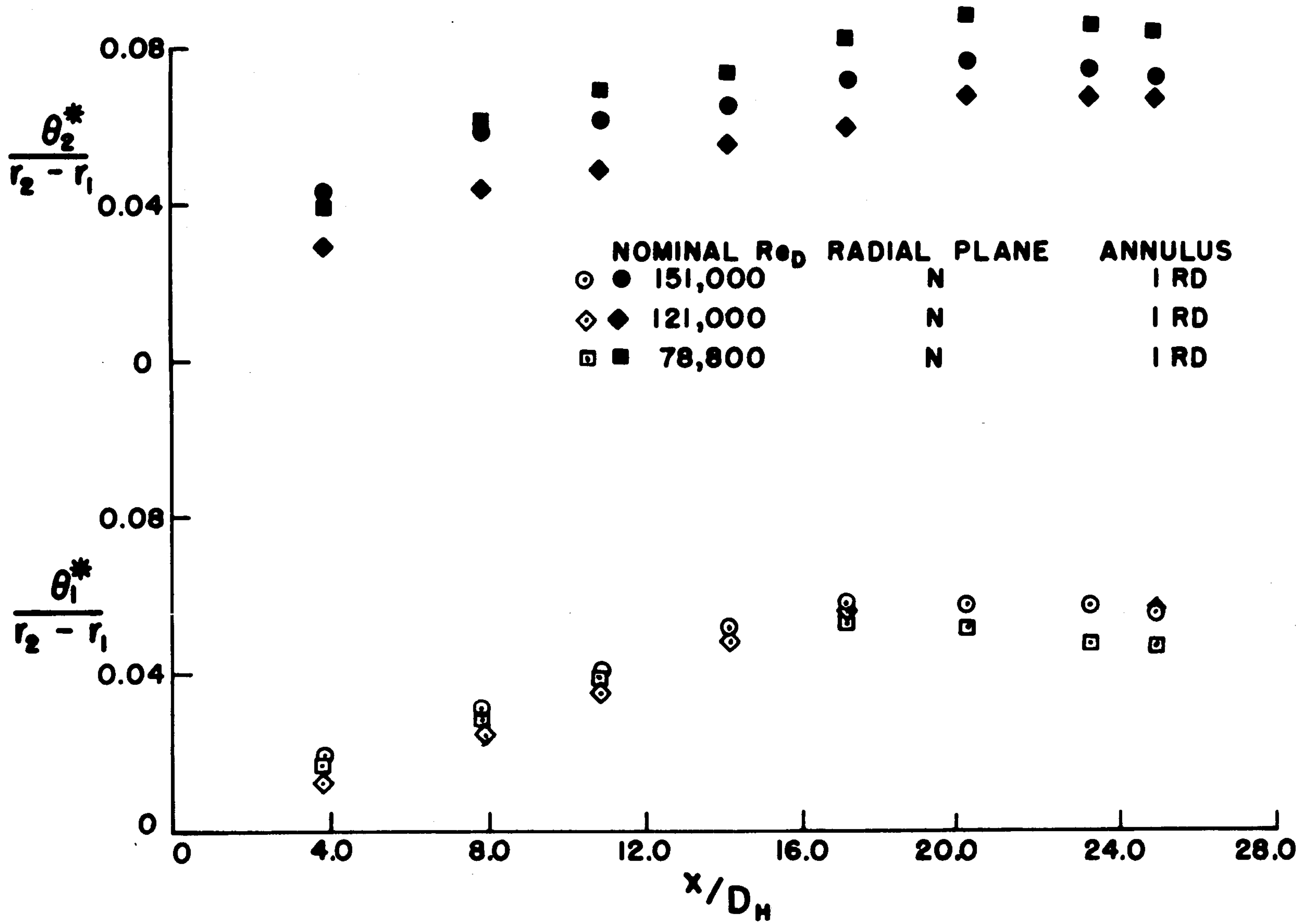

Figure 44. Variation of exact inner-and outer-wall boundary-layer-displacement-thickness parameters with x/D_H for radial plane N of annulus 1 RD.

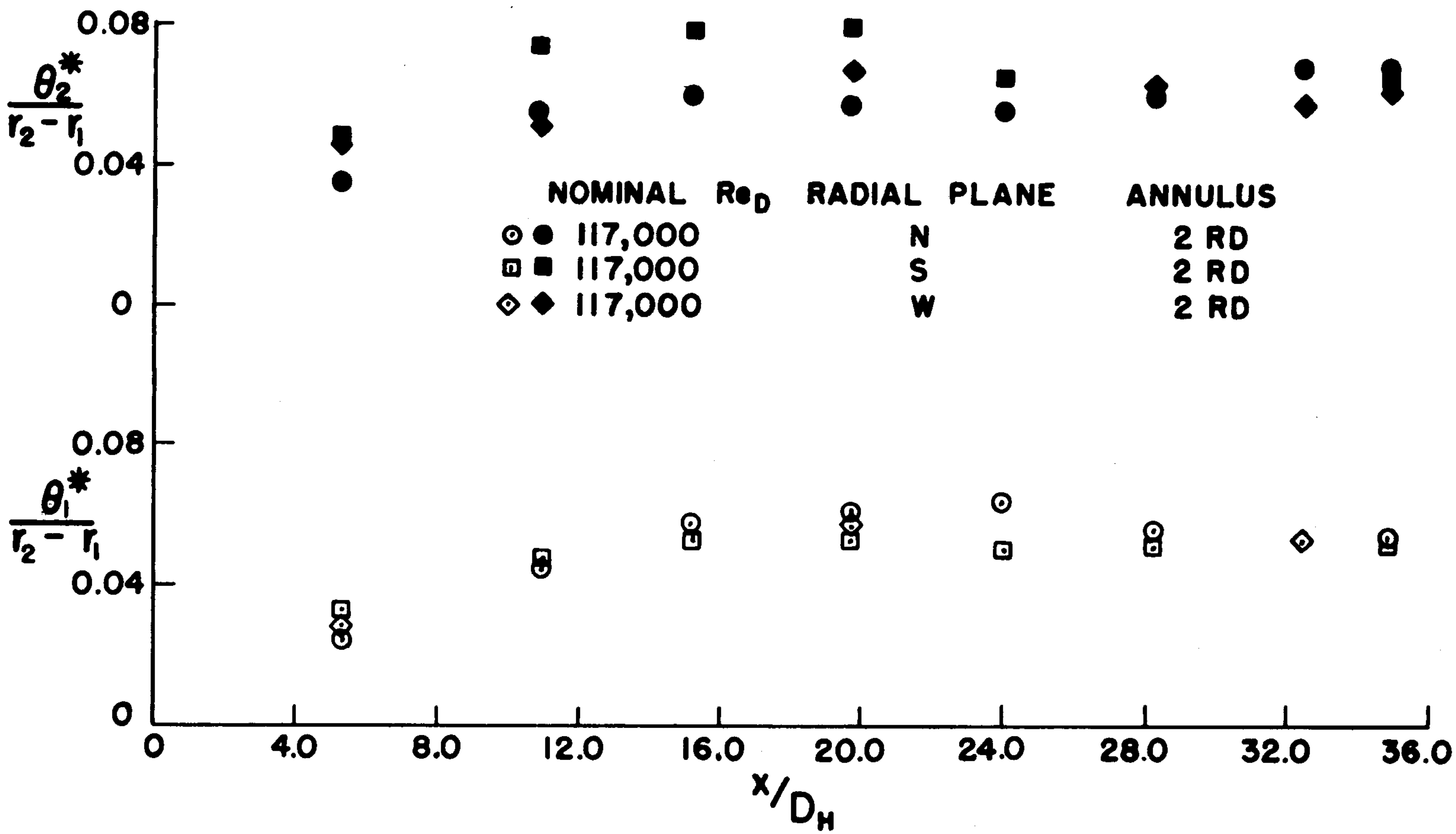

Figure 45. Variation of exact inner-and outer-wall boundary-layer-displacement-thickness parameters with x/D_H in annulus 2 RD for medium flow rate.

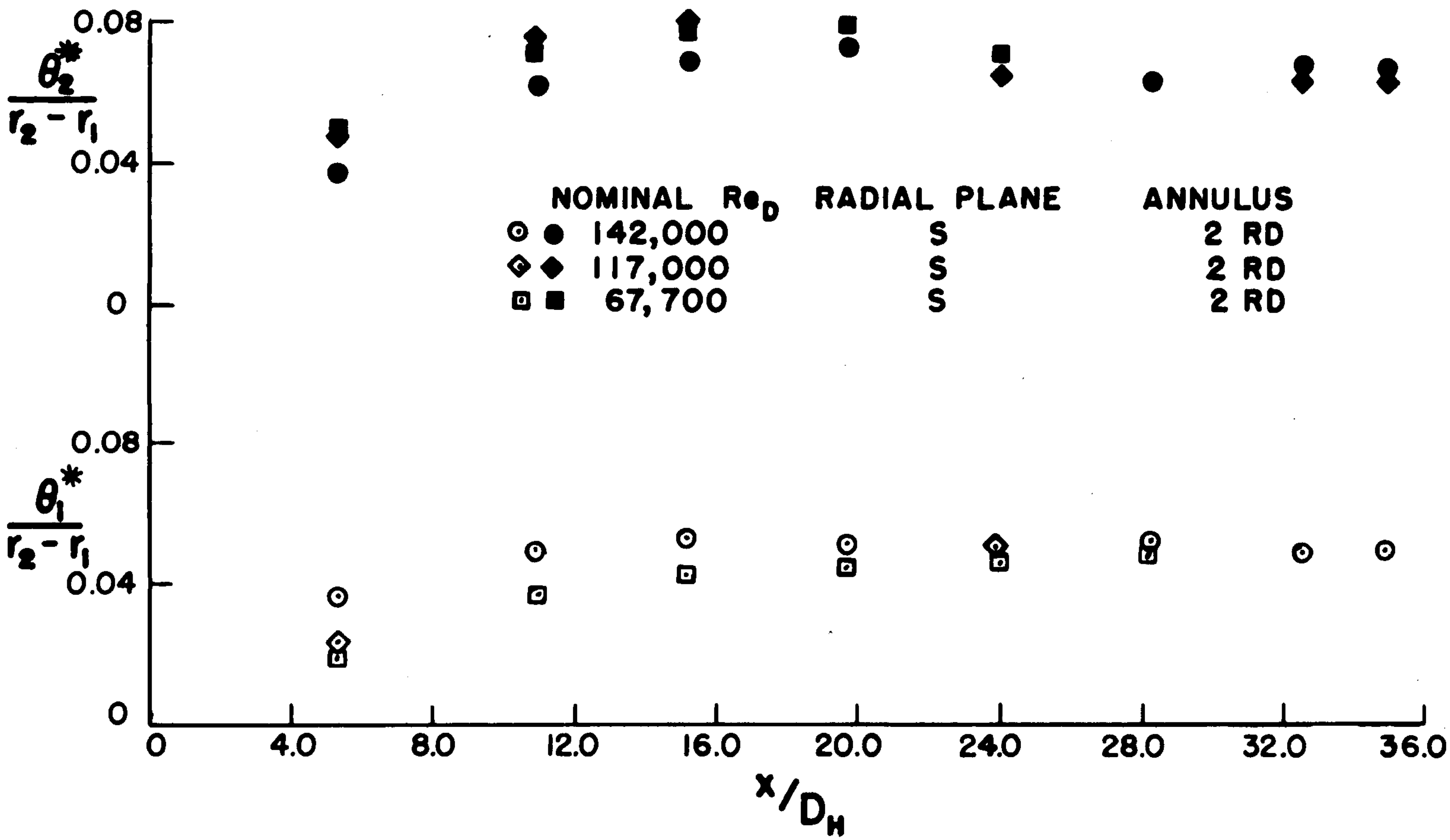

Figure 46. Variation of exact inner- and outer-wall boundary-layer-displacement-thickness parameters with x/D_H for radial plane S of annulus 2 RD.

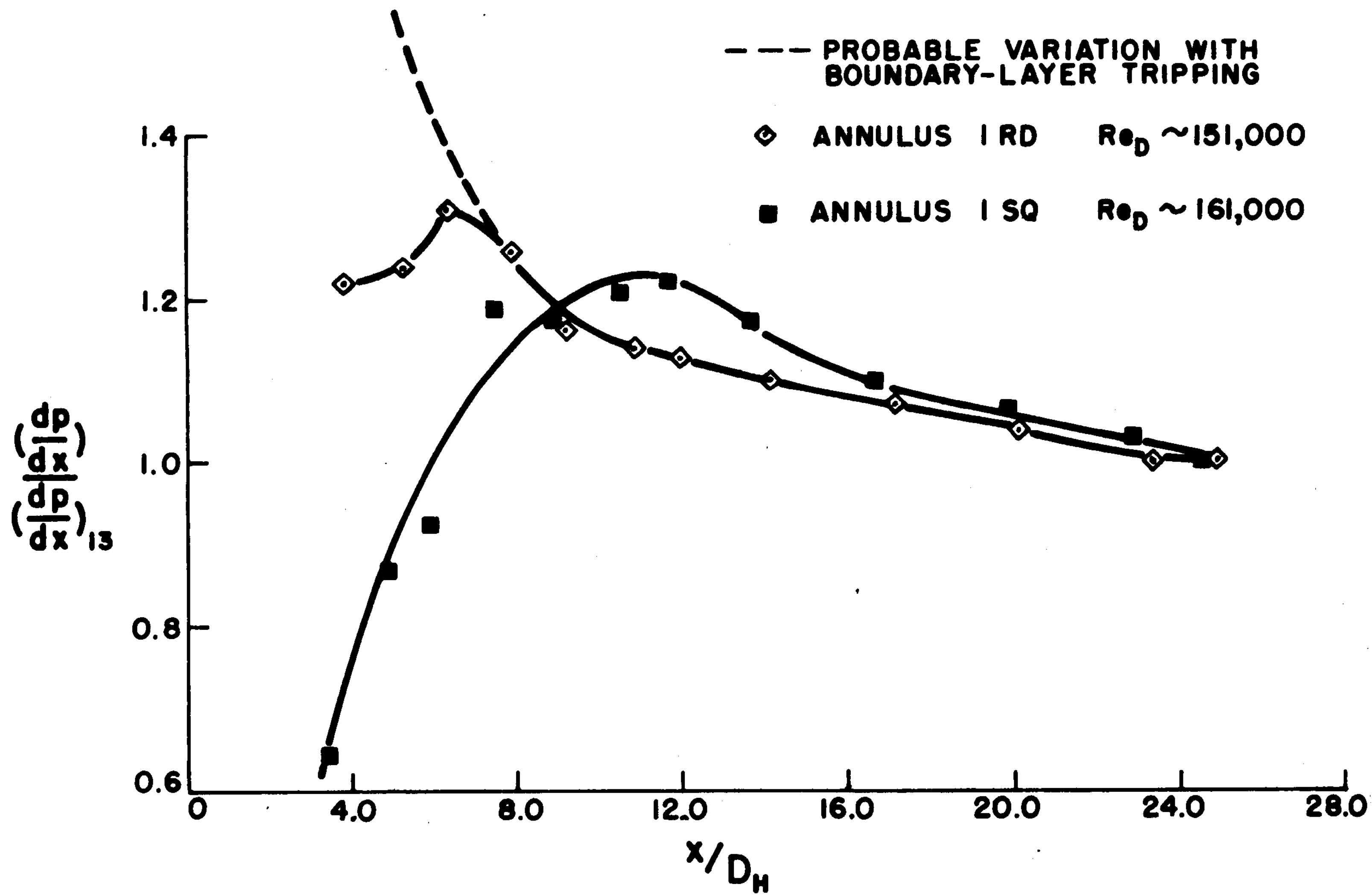

Figure 47. Variation of static-pressure-gradient parameter with x/D_H for high flow rates and annuli 1 RD and 1 SQ.

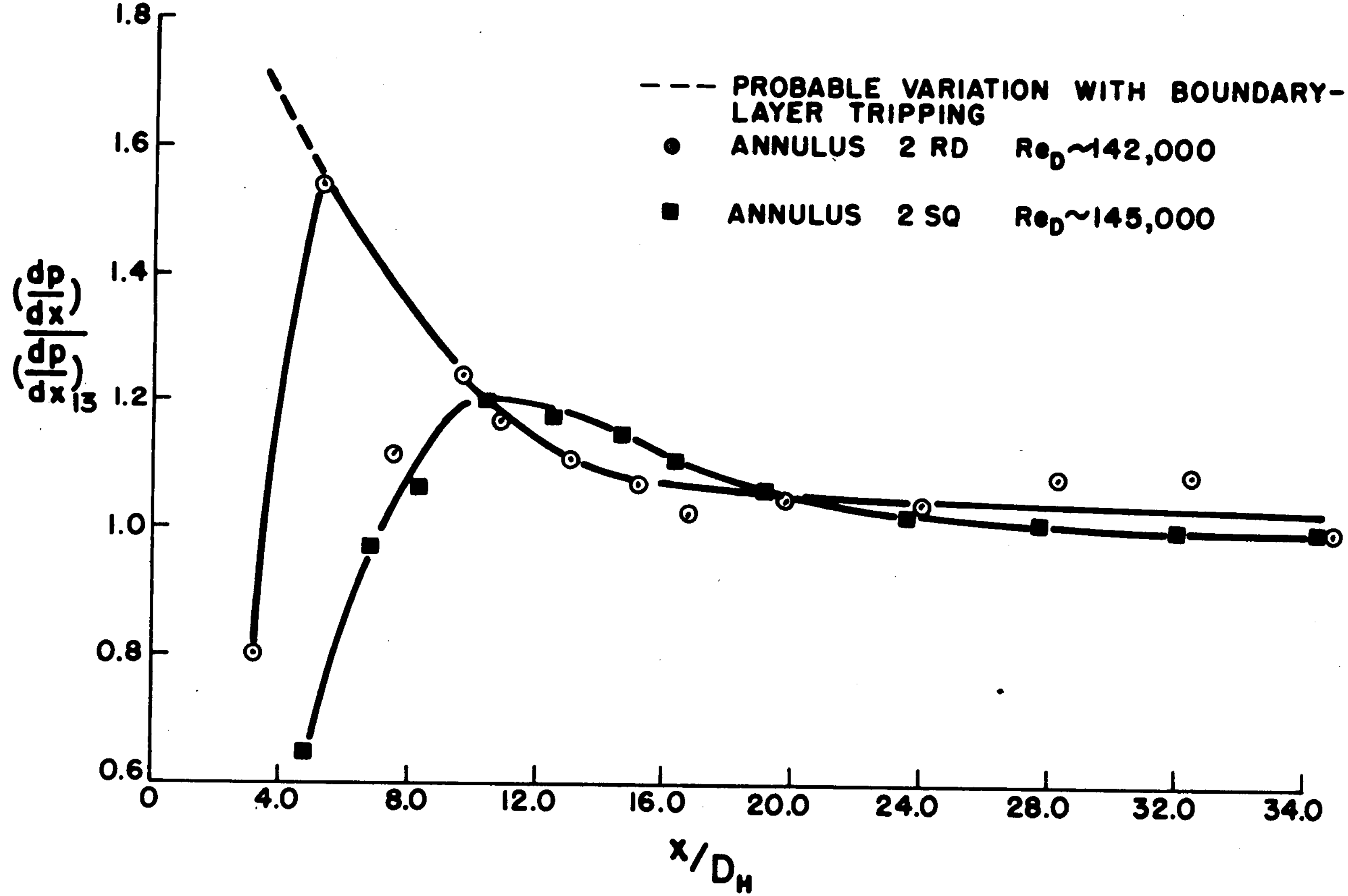

Figure 48. Variation of static-pressure-gradient parameter with x/D_H for high flow rates and annuli 2 RD and 2 SQ.

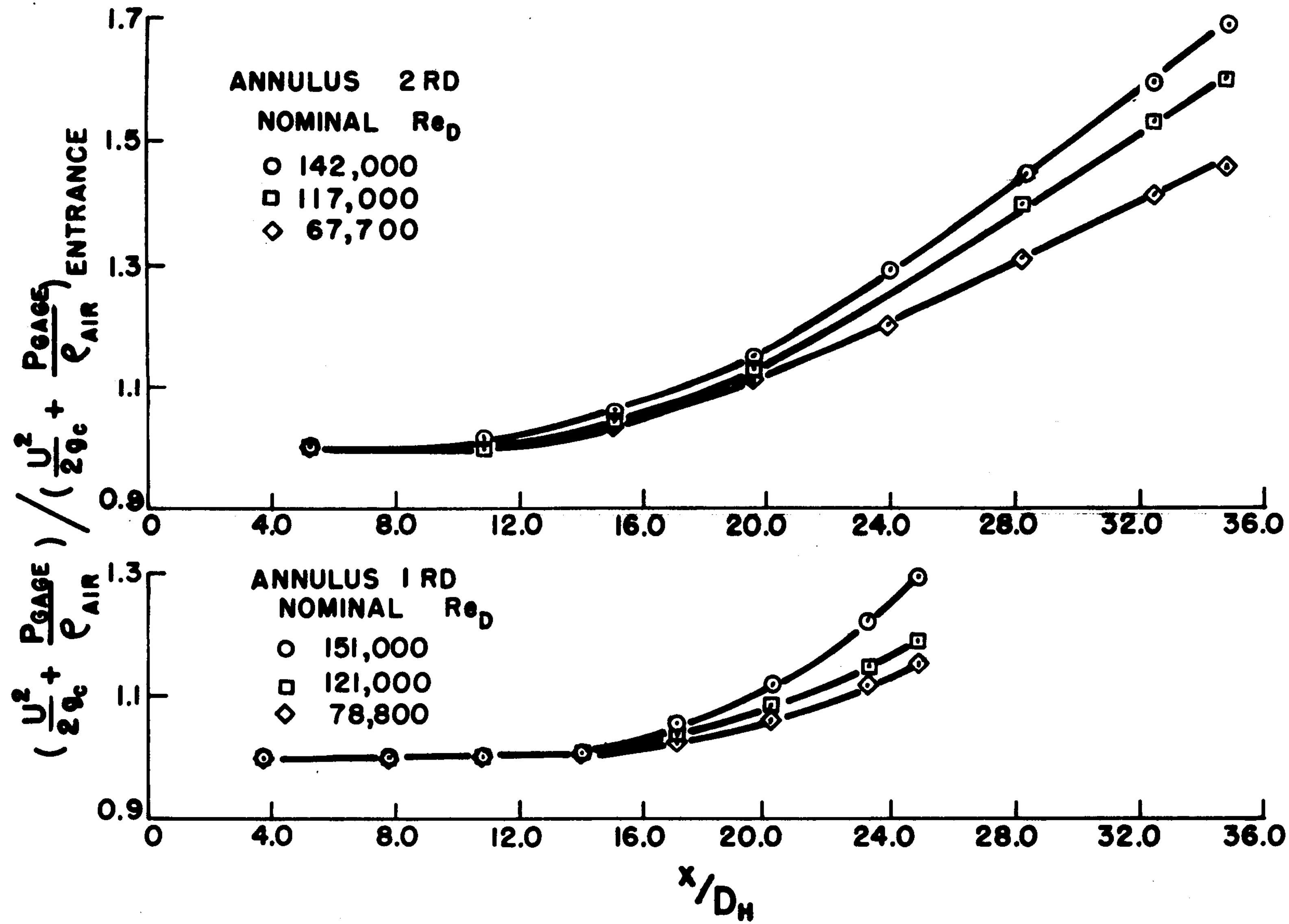

Figure 49. Typical variation of gage-pressure-Bernoulli-constant parameters with x/D_H for annuli 1 RD and 2 RD.

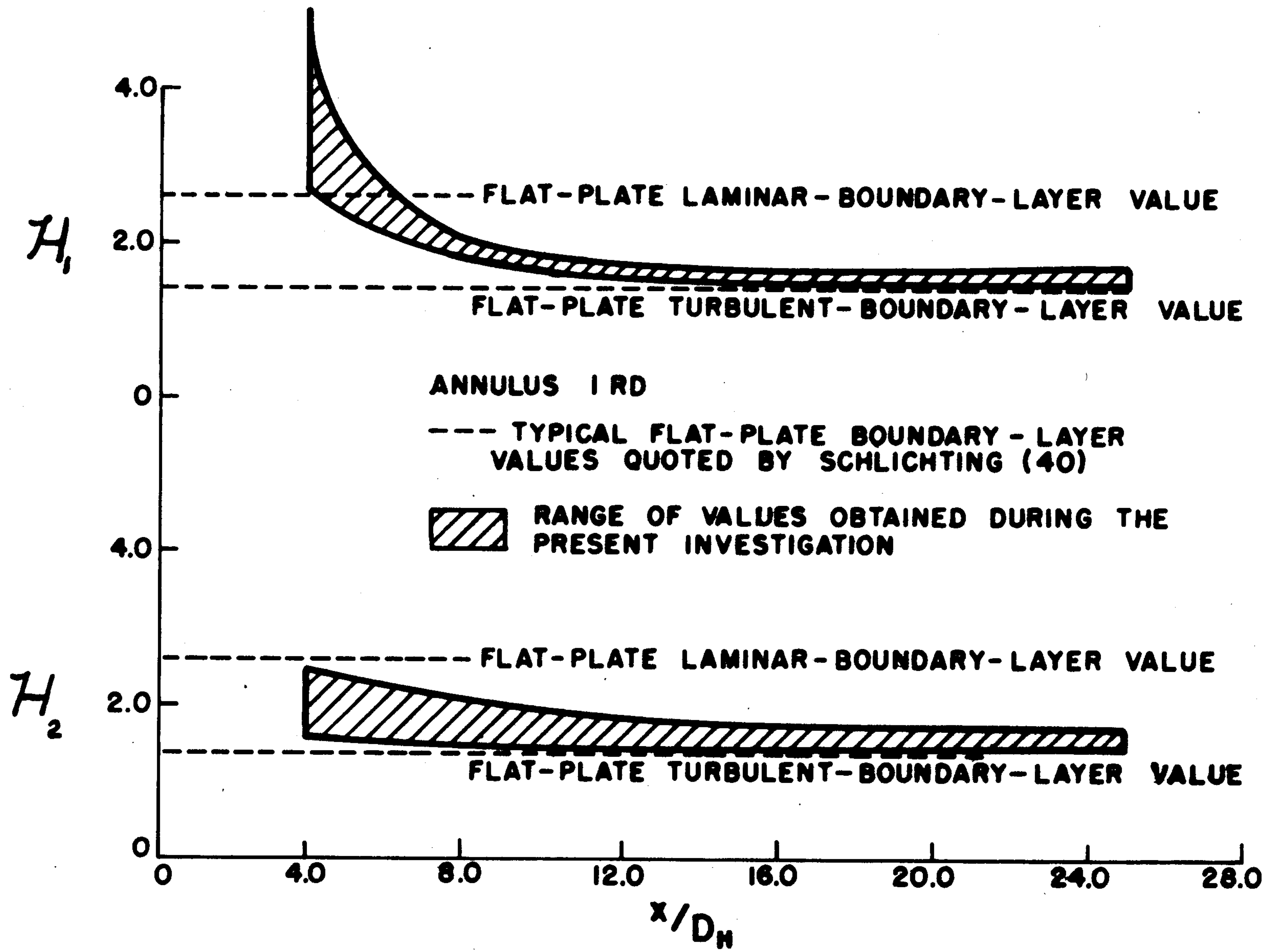

Figure 50. Variation of exact inner-and outer-wall boundary-layer-shape factors with x/D_H for annulus 1 RD.

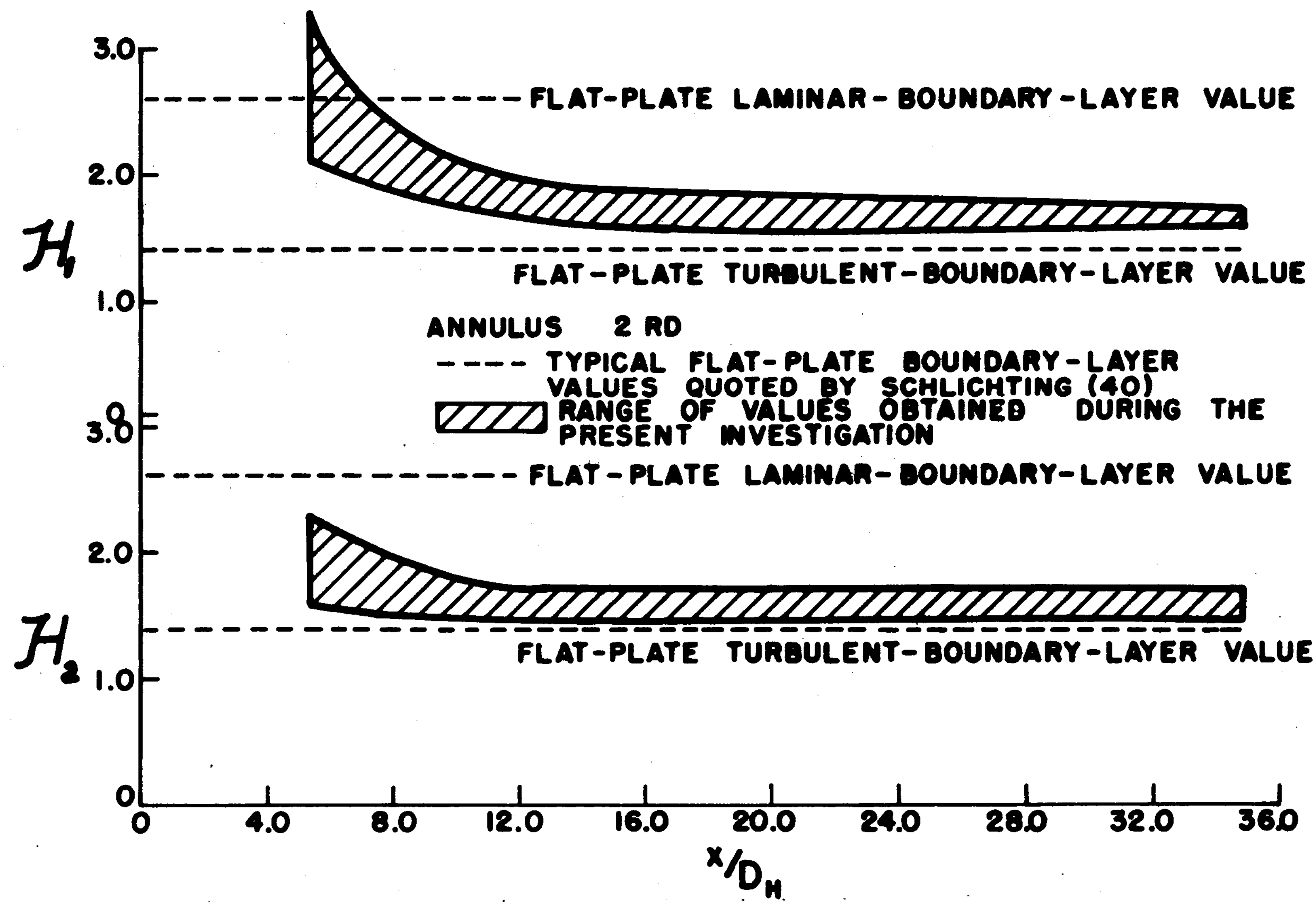

Figure 51. Variation of exact inner-and outer-wall boundary-layer shape factors with x/D_H for annulus 2 RD.

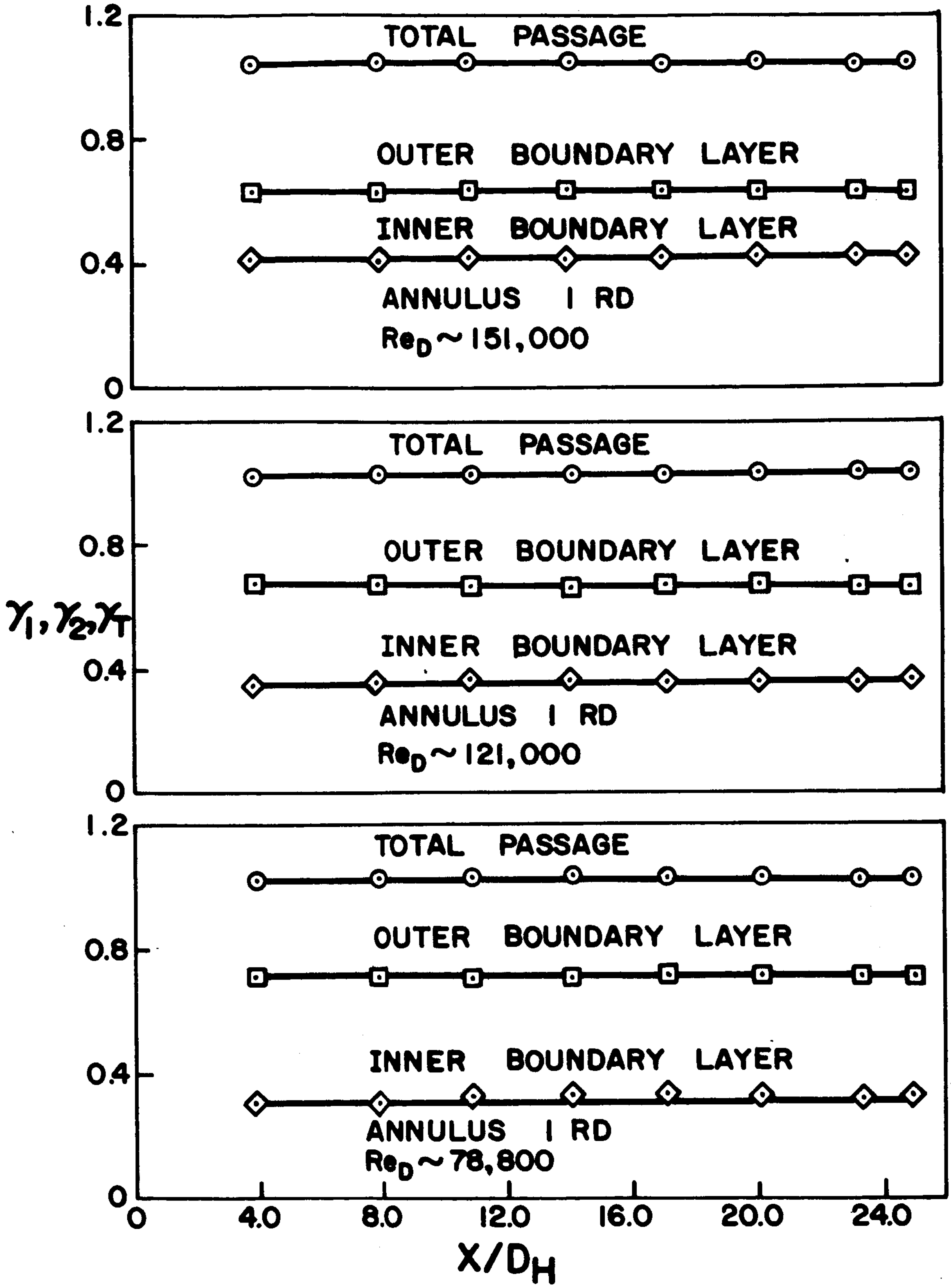

Figure 52. Typical variation of momentum-flux parameters with x/D_H for annulus 1 RD.

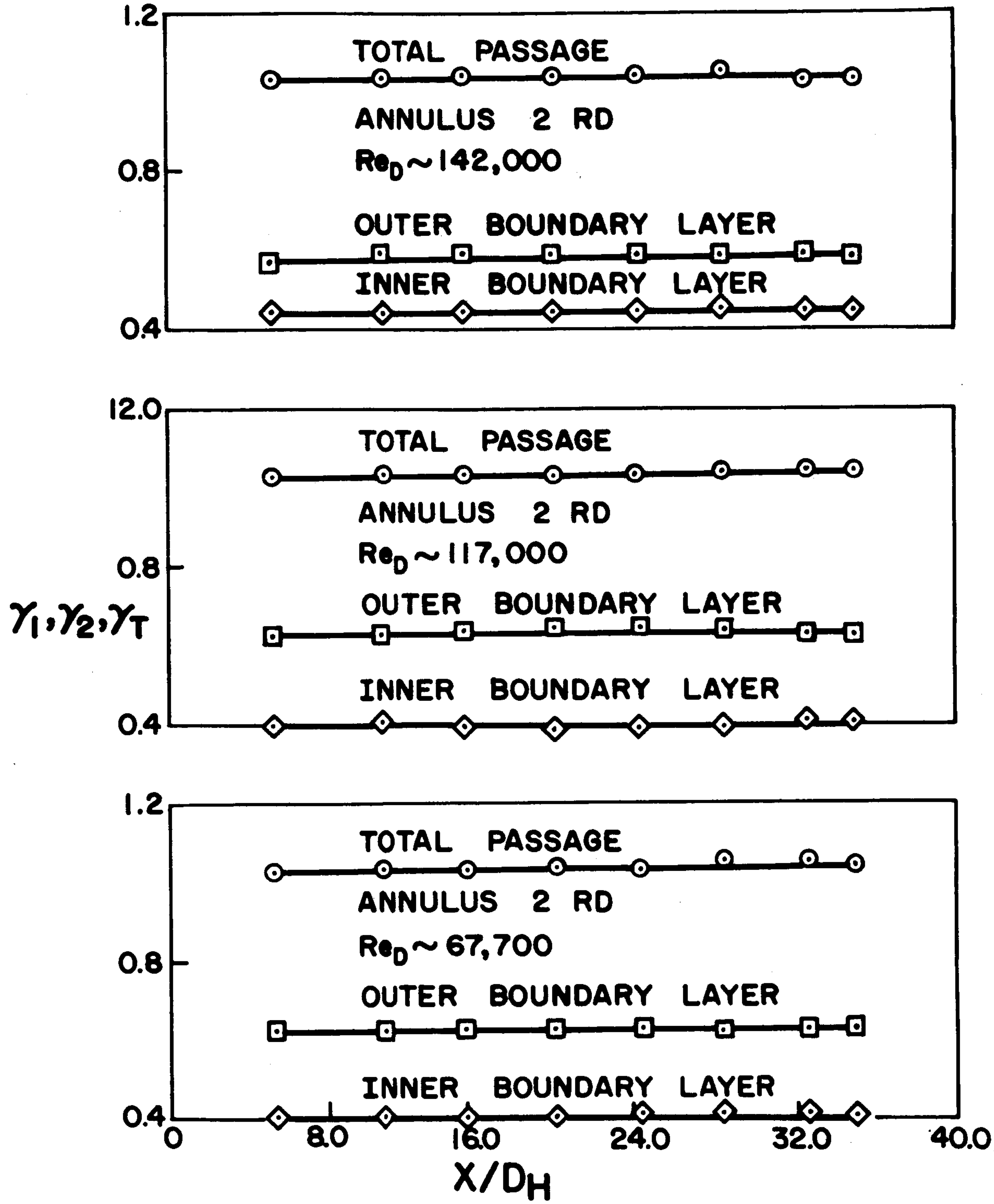

Figure 53. Typical variation of momentum-flux parameters with x/D_H for annulus 2 RD.

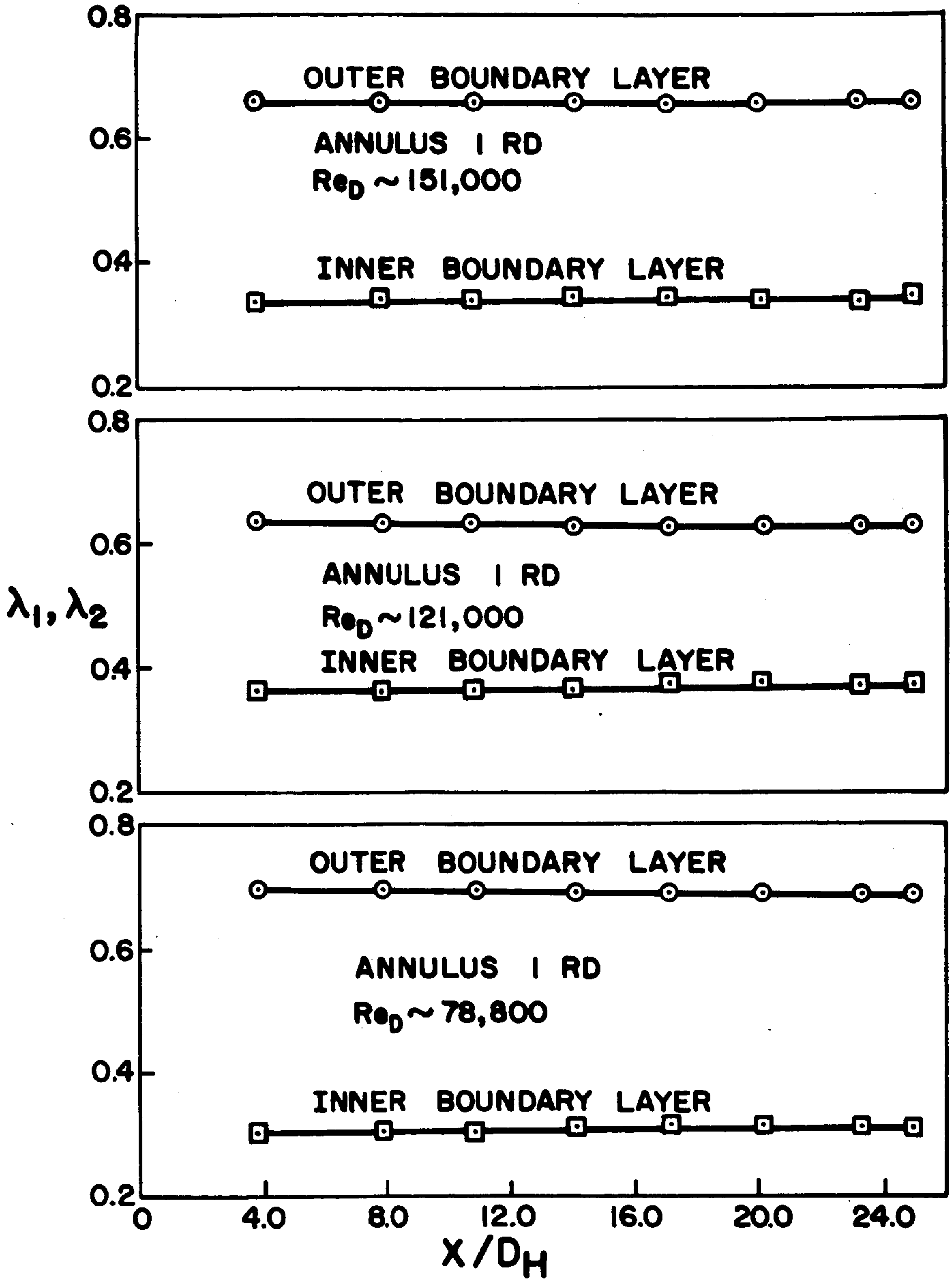

Figure 54. Typical variation of inner-and outer-wall boundary-layer partial-flow-rate parameters with x/D_H for annulus 1 RD.

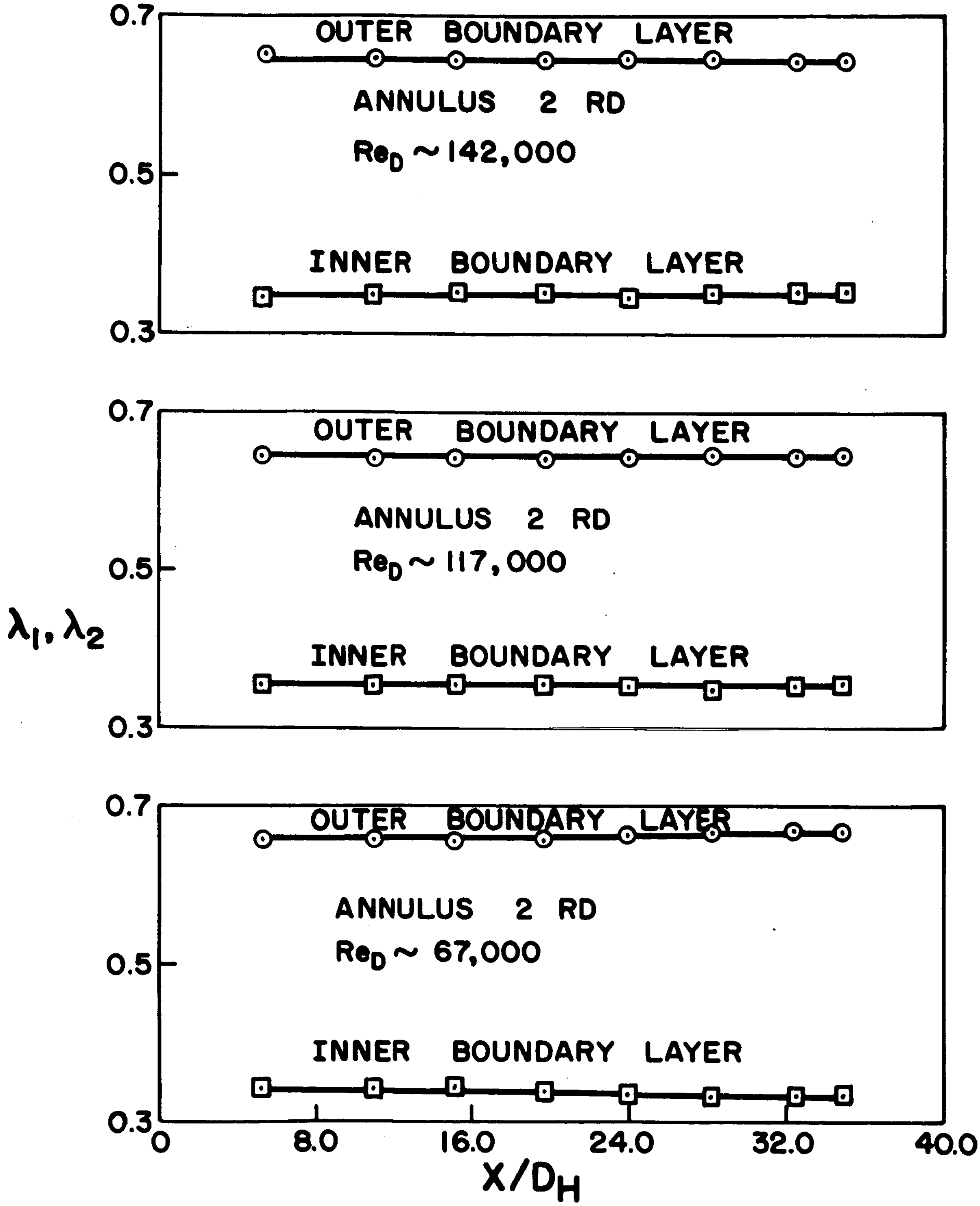

Figure 55. Typical variation of inner- and outer-wall boundary-layer partial-flow-rate parameters with x/D_H for annulus 2 RD.

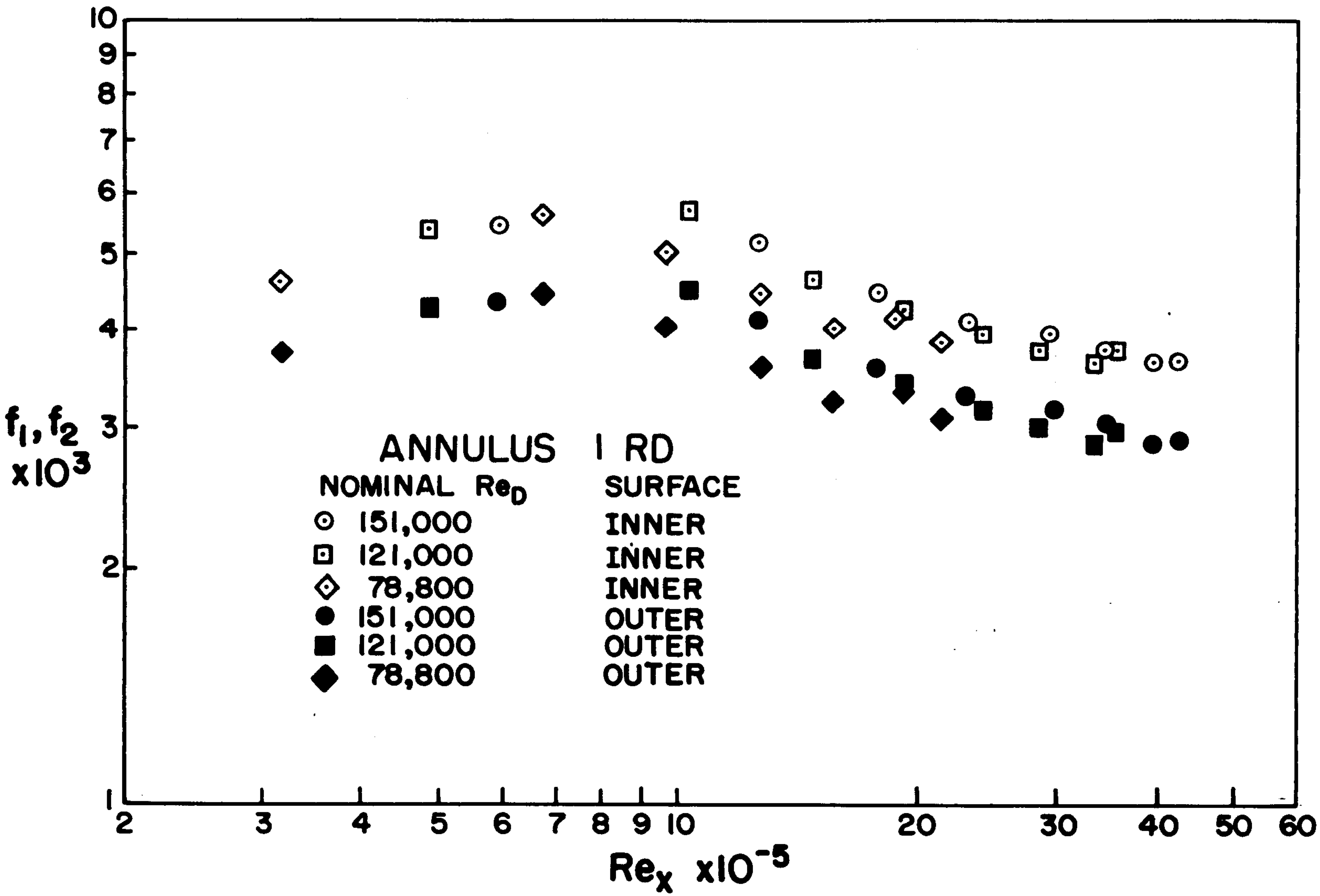

Figure 56. Variation of inner- and outer-wall local friction factors with Re_x for annulus 1 RD.

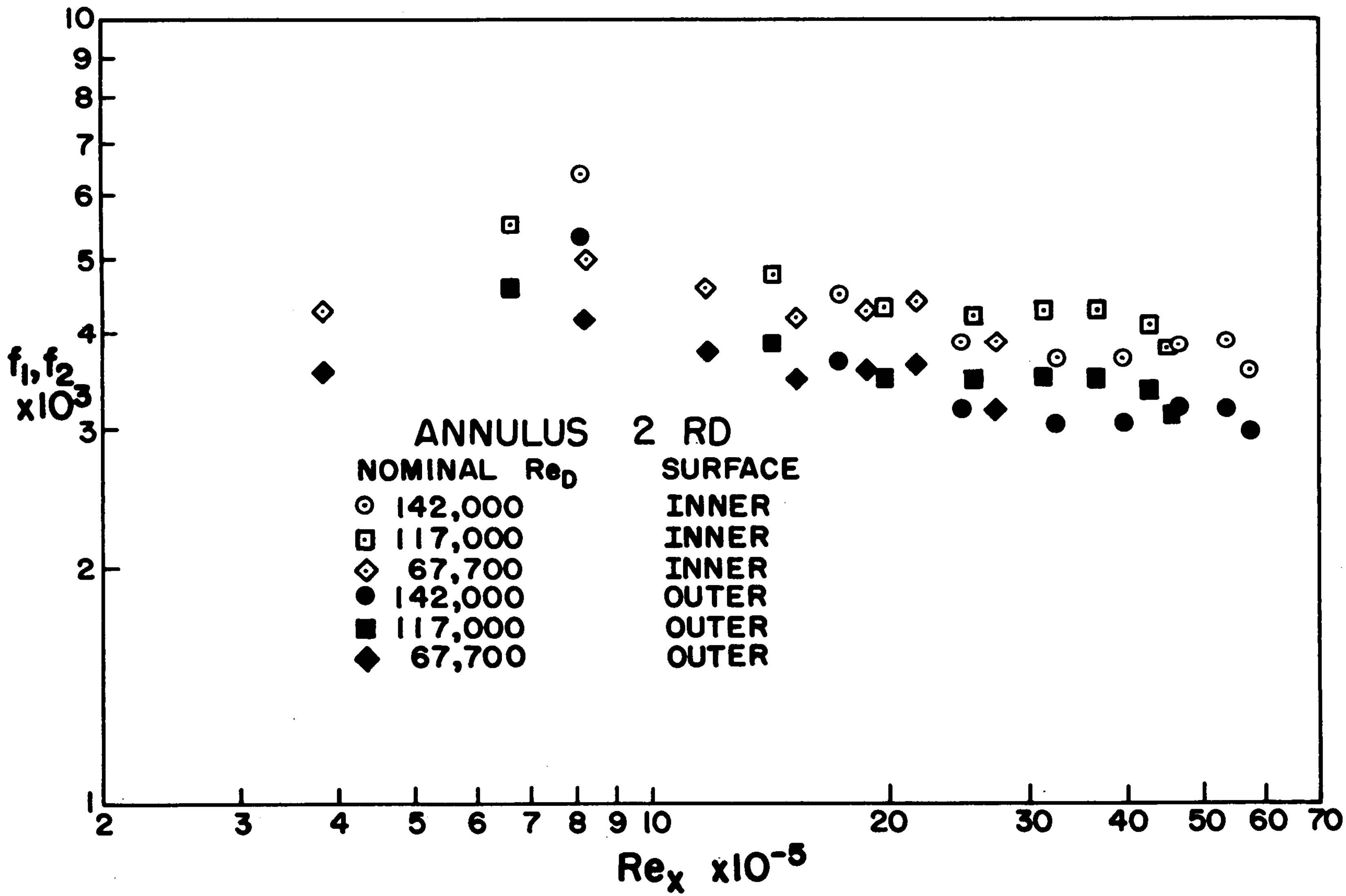

Figure 57. Variation of inner- and outer-wall local friction factors with Re_x for annulus 2 RD.

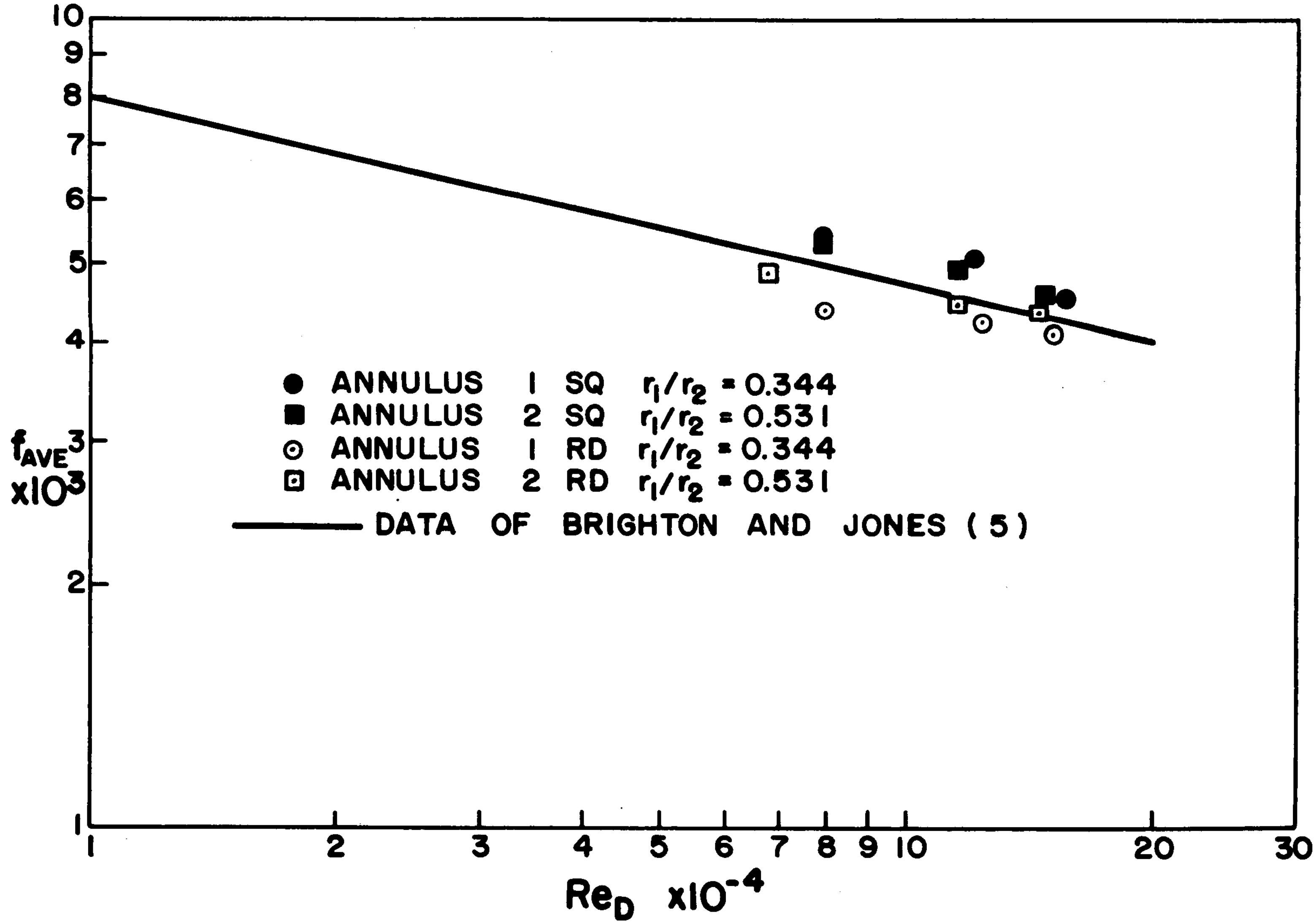

Figure 58. Variation of average friction factors with Re_D for axial location 12 of annuli 1 RD, 2 RD, 1 SQ, and 2 SQ.

CONCLUSIONS

Flow development through the annuli with square-edged entrances was apparently more repeatable than the flow development through the annuli with rounded entrances. This seems reasonable since the flow development in the inlet sections with square-edged entrances did not include the transition from laminar to turbulent flow present in the inlet sections with rounded entrances. The development patterns for the two types of entrances were quite different as demonstrated by the velocity-profile and pressure-gradient data. The separation caused by the abrupt change in area of the square-edged entrance resulted in skewed velocity profiles near the inlet. The rounded entrance produced a flat velocity profile at the throat. Fully developed mean-velocity profiles were apparently obtained in the annuli with square-edged entrances within the test lengths. The same lengths, however, were not sufficient for obtaining fully developed mean-velocity profiles in the annuli with rounded entrances. Mean-velocity data obtained in longer annuli with rounded entrances would certainly serve as a welcome supplement to the present information. At larger x values than were available during the present investigation, the effects of transition are probably non-existent.

It seems reasonable to assume that in typical annular flows, the flow development is not exactly axisymmetric. Even after special care was taken in assembling the present apparatus, noticeable differences in flow development along the three radial planes were present. Asymmetric flow development is probably inconsequential in most industrial applications; but in cases where axisymmetric patterns are of prime importance, careful assembly will be required. The control of transition by boundary-layer tripping would probably result in stable axisymmetric flow development in rounded-entrance annuli.

More shape-factor and friction-factor data will be required before even an approximate solution of the developing-boundary-layer problem for flow in an annulus with a rounded inlet can be obtained. Evidently, the occurrence of transition in the boundary layers is an important facet of the flow development in annuli with rounded entrances. The pressure-gradient, shape-factor, and skin-friction-factor data of annuli 1RD and 2RD were noticeably affected by transition. The asymmetric development and irregularity of flow trends were attributed to the intermittent and seemingly unpredictable nature of transition. Thus, a concentrated study of the basic nature of the transition process in an annulus with a rounded entrance appears to be in order. A flow-visualization study would probably be most practical.

The author realizes the questionable nature of the assumption that the static pressure remains constant over the cross section of the annular passage. Static-pressure gradients probably exist in the transverse direction in the initial portions of the annuli. However, until a means is devised for accurately measuring static pressure in internal passages where boundary effects are considerable, the assumption will necessarily be made as an approximation. The Reynolds equation containing the radial-pressure-gradient term might be used as a tool in solving this problem. Brighton and Jones (5) used this approach for the case of fully developed annular flow but were unable to obtain satisfactory static-pressure measurements to confirm their results.

REFERENCES

1. American Society of Mechanical Engineers. Research Committee on Fluid Meters. Fluid meters their theory and application. 5th ed. New York, N. Y., Author. 1959.

2. Barbin, A. R. Development of turbulence in the inlet of a smooth pipe. [Microfilm copy No. 61-6507. Unpublished Ph.D. thesis, Library, Purdue University, Lafayette, Indiana.] Ann Arbor, Michigan, University Microfilms. 1961.

3. Barbin, A. R. and Jones, J. B. Turbulent flow in the inlet region of a smooth pipe. American Society of Mechanical Engineers Transactions Series D: Journal of Basic Engineering 85:29-34. 1963.

4. Bodoia, J. R. and Osterle, J. F. Finite difference analysis of plane pouseuille and couette flow developments. Applied Scientific Research Series A, 10:265-276. 1961.

5. Brighton, J. A. and Jones, J. B. Fully developed turbulent flow in annuli. American Society of Mechanical Engineers Transactions Series D: Journal of Basic Engineering 86:835-844. 1964.

6. Campbell, W. D. and Slattery, J. C. Flow in the entrance of a tube. American Society of Mechanical Engineers Transactions Series D: Journal of Basic Engineering 85:41-45. 1963.

7. Chang, C. C. and Atabek, H. B. Flow between two co-axial tubes near the entry. Zeitschrift fur Angewandte Mathematik und Mechanik 42:425-430. 1962.

8. Collins, M. and Schowalter, W. R. Laminar flow in the inlet region of a straight channel. Physics of Fluids 5:1122-1124. 1962.

9. Croop, E. J. Velocity distribution in transitional flow through annuli. Unpublished Ph.D. thesis. Pittsburgh, Pennsylvania, Library, Carnegie Institute of Tech-

nology. 1958.

10. Croop, E. J. and Rothfus, R. R. Skin friction patterns for transitional flow in annuli. American Institute of Chemical Engineers Journal 8:26-30. 1962.

11. Davies, P. O. A. L. The behavior of a pitot tube in transverse shear. Journal of Fluid Mechanics 3:441-456. 1957.

12. Dean, R. C., Jr. Aerodynamic measurements. Cambridge, Massachusetts, Gas Turbine Laboratory, Massachusetts Institute of Technology. 1953.

13. Deissler, R. G. Analysis of turbulent heat transfer and flow in the entrance regions of smooth passages. U.S. National Advisory Committee for Aeronautics Technical Note 3016. 1953.

14. Filippov, G. V. On turbulent flow in the entrance length of a straight tube of circular cross section. Soviet Physics Technical Physics 3:1681-1686. 1958.

15. Fowler, A. H. and Wilson, C. W. Cubic spline, a curve fitting routine. U.S. Atomic Energy Commission Research and Development Report Y-1400. 1962.

16. Goldstein, S. Modern developments in fluid dynamics. Volume 1. Oxford, England, Clarendon Press. 1938.

17. Han, L. S. Hydrodynamic entrance lengths for incompressible flow in rectangular ducts. American Society of Mechanical Engineers Transactions Series E: Journal of Applied Mechanics 27:403-409. 1960.

18. Hanks, Richard W. Velocity profile development in the entrance region of a right circular cylinder with slip at the walls. The Physics of Fluids 6:1645-1648. 1963.

19. Heaton, H. S., Reynolds, W. C., and Kays, W. M. Heat transfer in annular passages. Simultaneous development of velocity and temperature fields in laminar flow. International Journal of Heat and Mass Transfer 7:763-781. 1964.

20. Holdhusen, J. S. The turbulent boundary layer in the inlet region of smooth pipes. [Microfilm copy No. 3945. Unpublished Ph.D. thesis, Library, University of Minnesota, Minneapolis, Minnesota.] Ann Arbor, Michigan, University Microfilms. 1952.

21. Keenan, J. H. and Kaye, J. Gas tables. New York, N. Y., John Wiley and Sons, Inc. 1948.

22. Keenan, J. H. and Keyes, F. G. Thermodynamic properties of steam. New York, N. Y., John Wiley and Sons, Inc. 1936.

23. Kline, S. J. and McClintock, F. A. Describing uncertainties in single sample experiments. Mechanical Engineering 75:3-8. 1953.

24. Lamb, Horace. Hydrodynamics. 6th ed. New York, N. Y., Dover Publications. 1945.

25. Langhaar, H. L. Steady flow in the transition length of a straight tube. American Society of Mechanical Engineers Transactions Series E: Journal of Applied Mechanics 64:A55-A58. 1942.

26. Latzko, H. Heat transfer in a turbulent liquid or gas stream. U.S. National Advisory Committee for Aeronautics Technical Memorandum 1068. 1944.

27. Lundgren, T. S., Sparrow, E. M., and Starr, J. B. Pressure drop due to the entrance region in ducts of arbitrary cross section. American Society of Mechanical Engineers Paper 63-WA-93. New York, N. Y., The Society. 1963.

28. MacMillan, F. A. Experiments on pitot-tubes in shear flow. Great Britain Aeronautical Research Council Reports and Memorandums 3028. 1957.

29. Obert, E. F. Concepts of thermodynamics. New York, N. Y., McGraw-Hill Book Company, Inc. 1960.

30. Okiishi, T. H. and Serovy, G. K. Experimental velocity profiles for fully developed turbulent flow of air in concentric annuli. American Society of Mechanical

Engineers Paper 64 WA/FE-32. New York, N. Y., The Society. 1964.

31. Olson, R. M. and Sparrow, E. M. Measurements of turbulent flow development in tubes and annuli with square or rounded entrances. American Institute of Chemical Engineers Journal 9:766-770. 1963.

32. Oosthuizen, P. H. An approximate analysis of the incompressible turbulent flow near the entrance to a two dimensional channel and to a pipe. South African Mechanical Engineer 13, No. 6:160-166. January 1964.

33. Prengle, R. S. and Rothfus, R. R. Transition phenomena in pipes and annular cross sections. Industrial and Engineering Chemistry 47:379-386. 1955.

34. Reynolds, W. C., Lundberg, R. E., and McCuen, P. A. Heat transfer in annular passages. General formulation of the problem for arbitrarily prescribed wall temperatures or heat fluxes. International Journal of Heat and Mass Transfer 6:483-493. 1963.

35. Roidt, M. and Cess, R. D. An approximate analysis of laminar magnetohydrodynamic flow in the entrance region of a flat duct. American Society of Mechanical Engineers Transactions Series E: Journal of Applied Mechanics 29: 171-176. 1962.

36. Ross, D. Turbulent flow in the entrance region of a pipe. American Society of Mechanical Engineers Transactions 78:915-923. 1956.

37. Rothfus, R. R. Velocity gradients and friction in concentric annuli. Unpublished Ph.D. thesis. Pittsburgh, Pennsylvania, Library, Carnegie Institute of Technology. 1948.

38. Rothfus, R. R., Monrad, C. C., Sikchi, K. G., and Heideger, W. J. Isothermal skin friction in flow through annular sections. Industrial and Engineering Chemistry 47:913-918. 1955.

39. Rouse, H., ed. Advanced mechanics of fluids. New York, N. Y., John Wiley and Sons, Inc. 1959.

40. Schlichting, Hermann. Boundary layer theory. 4th ed. New York, N. Y., McGraw-Hill Book Co., Inc. 1960.

41. Schubauer, G. B. and Klebanoff, P. S. Contributions on the mechanics of boundary-layer transition. U.S. National Advisory Committee for Aeronautics Technical Note 3489. 1955.

42. Shapiro, A. H. and Smith, R. Douglas. Friction coefficients in the inlet length of smooth round tubes. U.S. National Advisory Committee for Aeronautics Technical Note 1785. 1948.

43. Sparrow, E. M. and Lin, S. H. The developing laminar flow and pressure drop in the entrance region of annular ducts. American Society of Mechanical Engineers Transactions Series D: Journal of Basic Engineering 86:827-834. 1964.

44. Sparrow, E. M., Lin, S. H., and Lundgren, T. S. Flow development in the hydrodynamic entrance region of tubes and ducts. The Physics of Fluids 7:338-347. 1964.

45. Sugino, Eitaro. Velocity distribution and pressure drop in the laminar inlet of a pipe with annular space. Bulletin of the Japan Society of Mechanical Engineers 5: 651-655. 1962.

46. Thwaites, D. Incompressible aerodynamics. Oxford, England, The Clarendon Press. 1960.

47. Walker, J. E. Characteristics of isothermal flow in smooth concentric annuli. Unpublished Ph.D. thesis. Pittsburgh, Pennsylvania, Library, Carnegie Institute of Technology. 1957.

48. Walker, J. E. and Rothfus, R. R. Transitional velocity patterns in a smooth concentric annulus. American Institute of Chemical Engineers Journal 5:51-54. 1959.

ACKNOWLEDGEMENTS

The author appreciates the opportunity he had to work under the members of the faculty who consented to serve as graduate-study committee members. The committee members, Professor Henry M. Black, Professor Stephen J. Chamberlin, Professor Robert C. Fellinger, Dr. Jerold C. Mathews, Dr. George K. Serovy, and Dr. Donald F. Young, willingly offered their encouragement and assistance on many occasions.

Dr. George K. Serovy directed the research leading to this dissertation. His straightforward advice and counsel are especially valued.

The author would certainly be an ingrate if he did not acknowledge the financial assistance he received from the National Aeronautics and Space Administration under Grant NsG-62-60. A majority of the present investigation was carried out with their support.

The author also received financial aid from the I. S. U. Department of Mechanical Engineering, the I. S. U. Engineering Experiment Station, the I. S. U. Research Foundation, and the National Science Foundation. He is appreciative of the trust placed in him by these organizations.

The cooperation that the author received from the members of the Engineering Experiment Station Shop and Mr. Clifford Osam during the equipment fabrication phase of the present investigation was inspiring. The work of Mr. John Smith and Mr. Carmi Spicer was invaluable.

Obviously, the author is grateful for his wife who provided a motivating atmosphere at home.

APPENDIX A. SAMPLE CALCULATIONS

The calculations presented in this section are representative of those used to obtain the experimental results. All of the calculations were performed on an IBM 7074 computer system. The data of run 20807 (Annulus 2RD) were used for calculations 1 through 17. The data of run 012109 (Annulus 1RD) were used for calculation 18. The values of $_{32}s_{Hg}$ and R_{AIR} were as quoted by Obert (29). The values of s_{MAN} and μ_{AIR} were obtained from the tables of Keenan and Keyes (22), and Keenan and Kaye (21) respectively.

1. Atmospheric pressure, p_{ATM}:

$$p_{ATM} = (h_{hg} - h_{corr})(_{32}s_{Hg})$$

$$p_{ATM} = (29.25)(0.4912)$$

$$p_{ATM} = \underline{\underline{14.37}} \text{ psia}$$

2. Density of the flowing air, ρ_{AIR}:

$$\rho_{AIR} = \frac{(144)(p_{ATM} + p_{GAGE})}{(R_{AIR})(T_{AIR})}$$

$$\rho_{AIR} = \frac{(144)[14.37 + (-0.424)]}{(53.36)(529.98)}$$

$$\rho_{AIR} = \underline{\underline{0.071}} \text{ lb}_m/\text{ft}^3$$

3. Temporal-mean axial point velocity, u:

$$u = \sqrt{2g_c\left(\frac{\Delta h_v}{12}\right)\left(\frac{s_{MAN}-s_{AIR}}{\rho_{AIR}}\right)}$$

$$u = \sqrt{2(32.174)(3.635)\left(\frac{62.3-0.071}{(0.071)}\right)}$$

$$u = \underline{\underline{130.7}}\ \text{ft/sec}$$

4. Mass flow rate of air, $\dot{m}$:[1]

$$\dot{m} = \frac{(3600)(2)}{(144)}\ \pi\ \rho_{AIR} \int_{r_1}^{r_2} urdr$$

$$\dot{m} = \frac{(3600)(2)(3.14)(0.071)(231)}{144}$$

$$\dot{m} = \underline{\underline{2574}}\ lb_m/hr$$

[1]The integral $\int_{r_1}^{r_2} urdr$ and all other integrals were evaluated by employing a modification of the trapezoidal rule. The incremental areas enclosed by the trapezoids formed when straight lines were passed through the data were added together to obtain the total area.

5. Reynolds number based on hydraulic diameter, Re_D:

$$Re_D = \frac{(\dot{m})(4)(12)}{\pi(D_2+D_1)(\mu_{AIR})(3600)}$$

$$Re_D = \frac{(2574)(4)(12)}{(3.14)(4.000+2.125)(122.8X10^{-7})(3600)}$$

$$Re_D = \underline{\underline{145,000}}$$

6. Average air velocity, U_a:

$$U_a = \frac{\dot{m}(144)(4)}{(3600)(\rho_{AIR})\pi(D_2^2-D_1^2)}$$

$$U_a = \frac{(2574)(144)(4)}{(3600)(0.071)(3.14)[(4.000)^2-(2.125)^2]}$$

$$U_a = \underline{\underline{160.9}} \text{ ft/sec}$$

7. Exact annulus inner-wall displacement-thickness parameter, $\frac{\theta_1^*}{r_2-r_1}$:

$$\frac{\theta_1^*}{r_2-r_1} \cong \frac{\sqrt{2\int_{r_1}^{r_m}(1-\frac{u}{U})rdr + r_1^2} - r_1}{r_2-r_1}$$

$$\frac{\theta_1^*}{r_2-r_1} \cong \frac{\sqrt{2(0.0625) + (1.0625)^2} - 1.0625}{2.000 - 1.0625}$$

$$\frac{\theta_1^*}{r_2-r_1} = \underline{\underline{0.0614}}$$

8. Approximate annulus inner-wall displacement-thickness parameter, $\frac{\delta_1^*}{r_2-r_1}$:

$$\frac{\delta_1^*}{r_2-r_1} = \frac{\int_{r_1}^{r_m} r(1-\frac{u}{U})dr}{r_1(r_2-r_1)}$$

$$\frac{\delta_1^*}{r_2-r_1} = \frac{0.0625}{(1.0625)(2.000-1.0625)}$$

$$\frac{\delta_1^*}{r_2-r_1} = \underline{\underline{0.0627}}$$

9. Exact annulus inner-wall momentum-thickness parameter, $\frac{\theta_1^{**}}{r_2-r_1}$:

$$\frac{\theta_1^{**}}{r_2-r_1} = \frac{\sqrt{2\int_{r_1}^{r_m} r\,\frac{u}{U}\left(1-\frac{u}{U}\right)dr + r_1^2} - r_1}{r_2-r_1}$$

$$\frac{\theta_1^{**}}{r_2-r_1} = \frac{\sqrt{2(0.0394) + (1.0625)^2} - 1.0625}{2.000 - 1.0625}$$

$$\frac{\theta_1^{**}}{r_2-r_1} = \underline{\underline{0.039}}$$

10. Approximate annulus inner-wall momentum-thickness parameter, $\frac{\delta_1^{**}}{r_2-r_1}$:

$$\frac{\delta_1^{**}}{r_2-r_1} = \frac{\int_{r_1}^{r_m} r\,\frac{u}{U}\left(1-\frac{u}{U}\right)dr}{r_1(r_2-r_1)}$$

$$\frac{\delta_1^{**}}{r_2-r_1} = \frac{0.0394}{(1.0625)(0.9375)}$$

$$\frac{\delta_1^{**}}{r_2-r_1} = \underline{\underline{0.0395}}$$

11. Gage-pressure Bernoulli constant, B:

$$B = \frac{U^2}{2g_c} + \frac{(p_{GAGE})(144)}{\rho_{AIR}}$$

$$B = \frac{(180.49)^2}{(2)(32.174)} + \frac{(-0.4237)(144)}{0.071}$$

$$B = \underline{\underline{-362}} \text{ ft } lb_f/lb_m$$

12. Annulus inner-wall momentum-flux parameter, γ_1:

$$\gamma_1 = \frac{2\int_{r_1}^{r_m} \left(\frac{u}{U_a}\right)^2 r\,dr}{r_2^2 - r_1^2}$$

$$\gamma_1 = \frac{2(0.584)}{(2.000)^2-(1.0625)^2}$$

$$\gamma_1 = \underline{\underline{0.406}}$$

13. Partial mass-flow-rate parameter for the inner portion of flow, λ_1:

$$\lambda_1 = \frac{\int_{r_1}^{r_m} urdr}{\int_{r_1}^{r_2} urdr}$$

$$\lambda_1 = \frac{98.5}{231}$$

$$\lambda_1 = \underline{\underline{0.426}}$$

14. Static-pressure gradient, $\frac{dp}{dx}$:[1]

$$\frac{dp}{dx} = \frac{s_{MAN}}{1728} \frac{dh_s}{dx}$$

$$\frac{dp}{dx} = \frac{(62.3)(-0.05094)}{1728}$$

$$\frac{dp}{dx} = \underline{\underline{-0.00183}} \ lb_f/in.^2 in.$$

[1] The gradient $\frac{dh_s}{dx}$ was obtained with the cubic-spline computer program of Fowler and Wilson (15).

15. Annulus inner-wall friction factor, f_1:

$$f_1 = -2\left(\frac{r_m^2 - r_1^2}{2r_1}\right)\frac{g_c}{\rho_{AIR}U^2}\,\frac{dp(144)}{dx}$$

$$f_1 = -2\left[\frac{(1.503)^2 - (1.0625)^2}{2(1.0625)}\right]\frac{(32.174)(-0.00183)(144)}{(0.071)(180.49)^2}$$

$$f_1 = \underline{\underline{0.0039}}$$

16. Reynolds number based on x, Re_x:

$$Re_x = \frac{\rho_{AIR}Ux}{\mu_{AIR}12}$$

$$Re_x = \frac{(0.071)(180.49)(60)}{(122.8X10^{-7})(12)}$$

$$Re_x = \underline{\underline{5,250,000}}$$

17. Air-density error, ϵ_ρ:

$$\epsilon_\rho = \sqrt{\left(\frac{\partial\rho}{\partial p}\right)^2 \epsilon_p^2 + \left(\frac{\partial\rho}{\partial T}\right)^2 \epsilon_T^2}$$

$$\epsilon_\rho = \sqrt{\left(\frac{144}{RT}\right)^2 \epsilon_p^2 + \left[\frac{p(144)}{RT^2}\right]^2 \epsilon_T^2}$$

$$\epsilon_\rho = \sqrt{\left[\frac{144}{(53.36)(529.98)}\right]^2 (0.01)^2 + \left[\frac{(13.946)(144)}{(53.36)(529.98)^2}\right]^2 (0.5)^2}$$

$$\epsilon_\rho = \underline{\underline{0.000085}}\ \mathrm{lb_m/ft^3}$$

18. Average local friction factor, f_{AVE}:

$$f_{AVE} = -\frac{(D_2-D_1)(144)\ g_c}{2\rho_{AIR}U_a^2}\frac{dp}{dx}$$

$$f_{AVE} = -\frac{(4.000-1.375)(144)(32.174)(-0.00068)}{2(0.07)(120.4)^2}$$

$$f_{AVE} = \underline{\underline{0.00406}}$$

APPENDIX B. SYMBOLS

a_i Observed variable

B Gage-pressure Bernoulli constant

$$= \frac{U^2}{2g_c} + \frac{(p_{GAGE})(144)}{\rho_{AIR}}, \text{ ft } lb_f/lb_m$$

D Diameter, in. or ft

D_1 Outside diameter of the inner core of the annulus, in. or ft

D_2 Inside diameter of the outer pipe of the annulus, in. or ft

D_H Hydraulic diameter, in. or ft

F General function

f Local friction factor

$$= \frac{2\tau_o g_c}{\rho U^2}$$

f_1 Local friction factor for the inner wall of the annulus

$$= \frac{2\tau_{01} g_c}{\rho_{AIR} U^2}$$

f_2 Local friction factor for the outer wall of the annulus

$$= \frac{2\tau_{02} g_c}{\rho_{AIR} U^2}$$

f_{AVE} Average local friction factor

$$= \frac{(D_2 - D_1)(144) g_c}{2\rho_{AIR} U_a^2} \left(-\frac{dp}{dx}\right)$$

g_c Gravitational constant, $\frac{lb_m\ ft}{lb_f\ sec^2}$

h_{CORR} Temperature correction for the barometer reading, in. Hg or ft Hg

h_{Hg} Barometer reading, in. Hg

h_s Static gage-pressure head, in. H_2O

H Shape factor or ratio of displacement and momentum thicknesses

H_1 Approximate shape factor for the inner-wall boundary layer in the annulus

$$= \frac{\delta_1^*}{\delta_1^{**}}$$

H_2 Approximate shape factor for the outer-wall boundary layer in the annulus

$$= \frac{\delta_2^*}{\delta_2^{**}}$$

$\mathcal{H}_1$ Exact shape factor for the inner-wall boundary layer in the annulus

$$= \frac{\theta_1^*}{\theta_1^{**}}$$

$\mathcal{H}_2$ Exact shape factor for the outer-wall boundary layer in the annulus

$$= \frac{\theta_2^*}{\theta_2^{**}}$$

Δh_v Temporal-mean point-axial-velocity head, in. H_2O or ft H_2O

$\dot{m}$ Mass flow rate

$$= \frac{(3600)(2)\pi}{(144)} \rho_{AIR} \int_{r_1}^{r_2} urdr, \ \frac{lb_m}{hr}$$

p Temporal-mean fluid static pressure, psia or psfa

p_{ATM} Atmospheric pressure, psia or psfa

p_{GAGE} Static gage pressure, psig or psfg

$(\frac{dp}{dx})_{13}$ Static pressure gradient for axial station 13,

$$\frac{lb_f}{in^2 \ in}$$

r Radial coordinate, in. or ft

$r_{\delta 1}$ Radial distance from the annulus axis to the edge of the inner-wall boundary layer, in. or ft

$r_{\delta 2}$	Radial distance from the annulus axis to the edge of the outer-wall boundary layer, in. or ft
r_1	Radius of the inner wall of the annulus, in. or ft
r_2	Radius of the outer wall of the annulus, in. or ft
r_m	Radius of maximum velocity, in. or ft
R_{AIR}	Gas constant for air, $\frac{lb_f\ ft}{lb_m\ {}^oR}$
Re_D	Reynolds number based on hydraulic diameter $= \frac{(\dot{m})(4)(12)}{\pi(D_2+D_1)(\mu_{AIR})(3600)}$
Re_x	Reynolds number based on x $= \frac{\rho_{AIR} Ux}{\mu_{AIR}(12)}$
$_{32}S_{Hg}$	Specific weight of mercury at 32^{o}F, $\frac{lb_f}{in^3}$
S_{AIR}	Specific weight of flowing air, $\frac{lb_f}{ft^3}$
S_{MAN}	Specific weight of manometer fluid, $\frac{lb_f}{ft^3}$
t	Time, sec
t_{ROOM}	Room air temperature, ^{o}F
T_{AIR}	Absolute temperature of the flowing air, ^{o}R

u — Temporal-mean point velocity in the axial direction

$$= \sqrt{2g_c \frac{(\Delta h_v)}{(12)} \left(\frac{S_{MAN} - S_{AIR}}{\rho_{AIR}}\right)}\ , \ \frac{ft}{sec}$$

u' — Fluctuating velocity component in the axial direction, $\frac{ft}{sec}$

U — Temporal-mean maximum or freestream axial point velocity, $\frac{ft}{sec}$

U_a — Average axial velocity

$$\frac{(\dot{m})(144)(4)}{(3600)(\rho_{AIR})\pi(D_2^2 - D_1^2)}\ , \ \frac{ft}{sec}$$

v — Temporal-mean point velocity in the radial direction, $\frac{ft}{sec}$

v' — Fluctuating velocity component in the radial direction, $\frac{ft}{sec}$

w — Temporal-mean point-velocity in the tangential direction, $\frac{ft}{sec}$

w' — Fluctuating velocity component in the tangential direction, $\frac{ft}{sec}$

x — Axial-direction coordinate with origin at beginning of constant-area section, in. or ft

y	Coordinate perpendicular to the solid flow boundary, in.
β	Flat-plate boundary-layer thickness, in.
β^{*}	Flat-plate boundary-layer displacement thickness $= \int_0^{\beta} (1 - \frac{u}{U})dy$, in.
β^{**}	Flat-plate boundary-layer momentum thickness $= \int_0^{\beta} \frac{u}{U}(1 - \frac{u}{U})dy$, in.
Y_1	Annulus inner-wall boundary-layer-momentum-flux parameter $= \dfrac{2\int_{r_1}^{r_m} (\frac{u}{U_a})^2 rdr}{r_2^2 - r_1^2}$
Y_2	Annulus outer-wall boundary-layer-momentum-flux parameter $= \dfrac{2\int_{r_m}^{r_2} (\frac{u}{U_a})^2 rdr}{r_2^2 - r_1^2}$.
Y_T	Annulus total-passage-momentum-flux parameter $= \dfrac{2\int_{r_1}^{r_2} (\frac{u}{U_a})^2 rdr}{r_2^2 - r_1^2}$

δ_1 Annulus inner-wall boundary-layer thickness, in.

δ_2 Annulus outer-wall boundary-layer thickness, in.

δ_1^* Approximate annulus inner-wall boundary-layer displacement thickness

$$= \frac{1}{r_1} \int_{r_1}^{r_{\delta 1}} r\left(1 - \frac{u}{U}\right)dr, \text{ in.}$$

δ_1^{**} Approximate annulus inner-wall boundary-layer momentum thickness

$$= \frac{1}{r_1} \int_{r_1}^{r_{\delta 1}} r \frac{u}{U}\left(1 - \frac{u}{U}\right)dr, \text{ in.}$$

δ_2^* Approximate annulus outer-wall boundary-layer displacement thickness

$$= \frac{1}{r_2} \int_{r_{\delta 2}}^{r_2} r\left(1 - \frac{u}{U}\right)dr, \text{ in.}$$

δ_2^{**} Approximate annulus outer-wall boundary-layer momentum thickness

$$= \frac{1}{r_2} \int_{r_{\delta 2}}^{r_2} r \frac{u}{U}\left(1 - \frac{u}{U}\right)dr, \text{ in.}$$

η Odds

ϵ_i One-half the uncertainty interval associated with variable i, units of i

θ_1^* Exact annulus inner-wall boundary-layer displacement thickness

$$= \sqrt{\int_{r_1}^{r_{\delta 1}} 2\left(1 - \frac{u}{U}\right)rdr + r_1^2} - r_1 \text{, in.}$$

θ_1^{**} Exact annulus inner-wall boundary-layer momentum thickness

$$= \sqrt{\int_{r_1}^{r_{\delta 1}} 2r \frac{u}{U}\left(1 - \frac{u}{U}\right)dr + r_1^2} - r_1, \text{ in.}$$

θ_2^{*} Exact annulus outer-wall boundary-layer displacement thickness

$$= r_2 - \sqrt{r_2^2 - \int_{r_{\delta 2}}^{r_2} 2\left(1 - \frac{u}{U}\right)rdr} \quad , \text{ in.}$$

θ_2^{**} Exact annulus outer-wall boundary-layer momentum thickness

$$= r_2 - \sqrt{r_2^2 - \int_{r_{\delta 2}}^{r_2} 2r \frac{u}{U}\left(1 - \frac{u}{U}\right)dr} \quad , \text{ in.}$$

λ_1 Annulus inner-wall boundary-layer partial-flow-rate parameter

$$= \frac{\int_{r_1}^{r_m} urdr}{\int_{r_1}^{r_2} urdr}$$

λ_2 Annulus outer-wall boundary-layer partial-flow-rate parameter

$$= \frac{\int_{r_m}^{r_2} urdr}{\int_{r_1}^{r_2} urdr}$$

μ Absolute viscosity of the flowing fluid, $\frac{lb_m}{ft\ sec}$

μ_{AIR} Absolute viscosity of the flowing air, $\frac{lb_m}{ft\ sec}$

Flowing-fluid kinematic viscosity, $\frac{ft^2}{sec}$

ρ_{AIR} Density of the flowing air

$$= \frac{(p_{ATM} + p_{GAGE})144}{R_{AIR}\ T_{AIR}}, \quad \frac{lb_m}{ft^3}$$

τ_0 Surface shear stress, $\frac{lb_f}{ft^2}$

τ_{01} Annulus inner-wall shear stress, $\frac{lb_f}{ft^2}$

τ_{02} Annulus outer-wall shear stress, $\frac{lb_f}{ft^2}$

ϕ Tangential-direction coordinate, radians

Ω Force-field potential, $\frac{ft\ lb_f}{lb_m}$